Summer 8-15-2022

Focused Ultrasound-Enabled Blood-Based Liquid Biopsy (Sonobiopsy) for Brain Disease Diagnosis

Christopher Pham Pacia
Washington University in St. Louis

WASHINGTON UNIVERSITY IN ST. LOUIS

McKelvey School of Engineering
Department of Biomedical Engineering

Dissertation Examination Committee:
Hong Chen, Chair
Aadel A. Chaudhuri
H. Michael Gach
Eric C. Leuthardt
James D. Quirk

Focused Ultrasound-Enabled Blood-Based Liquid Biopsy (Sonobiopsy) for Brain Disease Diagnosis

by
Christopher Pham Pacia

A dissertation presented to
the McKelvey School of Engineering
of Washington University in
partial fulfillment of the
requirements for the degree
of Doctor of Philosophy

August 2022
St. Louis, Missouri

Table of Contents

List of Figures

List of Tables

Acknowledgments

I would like to thank all the lab members who have helped perform the studies: Yimei Yue, for help with mouse surgeries and histological staining; Dr. Jinyun Yuan, for help with tumor implantations and plasma analysis; Dr. Lifei Zhu, for mentorship during the pig study; Yaoheng Yang, for help conduct the mouse experiments; Dr. Arash Nazeri, for help planning and analyzing the Alzheimer's study; Lu Xu, for help in the neuronavigation-guided study. I also want to acknowledge the co-authors who have provided valuable input: Dr. H. Michael Gach, Dr. Michael R. Talcott, Dr. Eric C. Leuthardt, Dr. Rupen Desai, Dr. Xiaowei Wang, Dr. Aadel A. Chaudhuri, and Dr. Gavin P. Dunn. I would like to thank Erik Dumont from Image Guided Therapy for assistance with developing the MRI-guided FUS system. We thank the Division of Comparative Medicine at Washington University in St. Louis, including Michael Talcott, Todd Pavek, Angie Lewis, Charles Mitchell, Alicia Sexauer, Susan Spiess, Matthew Bledsoe, and Chris Sanders for help with the pig study. We thank Linda Hood for assistance with operating the 3T Siemens PRISMA Fit clinical scanner and Dr. James D. Quirk for the assistance in setting up the 4.7T Agilent Varian small animal scanner. I would also like to thank the staff of the Washington University Instrument Machine Shop: John Witte, Kevin Poenicke, Francis Sindelar, for fabricating the MRI-compatible equipment. I was supported by my advisor, Dr. Hong Chen, and by the Cognitive, Computational and Systems Neuroscience Pathway (CCSN) at Washington University in St. Louis under the one-year traineeship and the NIH T32NS115672.

Christopher Pham Pacia

Washington University in St. Louis

August 2022

Dedicated to my loving wife and my supportive family
for their constant encouragement and motivation.

ABSTRACT OF THE DISSERTATION

Focused Ultrasound-Enabled Blood-Based Liquid Biopsy (Sonobiopsy)

for Brain Disease Diagnosis

by

Christopher Pham Pacia

Doctor of Philosophy in Biomedical Engineering

Washington University in St. Louis, 2022

Professor Hong Chen, Chair

Brain cancer severely threatens human health due to its disruption of neurological function, poor prognosis, and substantial reduction in quality of life. Glioblastoma (GBM) is the most devastating brain cancer; not only is it the most common malignant primary tumor in adults, but also it has a median survival of 14 months with a 5-year survival rate of less than 5%. Despite advances in multidisciplinary treatment that includes surgical resection, radiation therapy, and chemotherapy, almost all patients experience tumor progression and nearly universal mortality within 2 years. However, advances in patient care have suggested that the accurate diagnosis of molecular subtypes is critical for individualized targeted treatment and improving survival outcome for brain cancer patients.

Conventional diagnostic evaluation begins with neuroimaging and continues with surgical tissue biopsy to confirm the diagnosis and acquire the molecular profile of the tumor. Though tissue biopsy is the gold standard for molecular characterization, there are significant risks for patients because the procedure is invasive. Liquid biopsy is a minimally invasive approach that enables genetic profiling by detecting circulating tumor-derived biomarkers that

were shed by tumors into the blood circulation. However, blood-based liquid biopsy is inherently limited by the blood-brain barrier (BBB) that hinders the release of molecular biomarkers, leading to a low detection sensitivity for GBM.

The combination of focused ultrasound (FUS) with microbubbles is an established technique to disrupt the BBB noninvasively and transiently with high precision (on the order of millimeter). Though this has conventionally been used to deliver drugs from the bloodstream to the brain tissue of interest, it is hypothesized that this FUS-induced BBB disruption enables molecules to be released from the tissue into the blood circulation. Under this "two-way trafficking" hypothesis, FUS-enabled blood-based liquid biopsy (sonobiopsy) can release brain tumor-derived biomarkers into the blood circulation to improve the sensitivity for noninvasive molecular characterization of GBM. In this work, we evaluated the feasibility, safety, and efficacy of sonobiopsy in small and large animal models to provide a minimally invasive, spatiotemporally-controlled, and sensitive molecular characterization of brain diseases.

First, we evaluated the impact of different sonobiopsy parameters on the extent of biomarker release and tissue damage in a mouse GBM model. The blood collection time after FUS sonication was an important factor to minimize the effect of clearance and maximize the level of biomarkers detected in the plasma. Importantly, careful optimization of key sonobiopsy parameters, e.g., FUS pressure, microbubble dose, and sonication volume, was necessary to increase the release of circulating biomarkers while minimizing the potential for tissue damage. With the optimized parameters, sonobiopsy significantly increased the plasma level of GBM-derived biomarkers and improved the detection sensitivity for two clinically relevant mutations.

Second, sonobiopsy was performed in a non-tumor pig model to demonstrate the potential for clinical translation. A customized sonobiopsy device was developed to target a

specific brain area and release brain-specific biomarkers into the blood circulation. Importantly, sonobiopsy significantly increased the plasma level of these biomarkers without causing detectable tissue damage. This large animal study demonstrated that sonobiopsy has the potential to be safely translated to humans.

To further underscore the potential for clinical translation of sonobiopsy, a pig GBM model was developed to assess the feasibility of sonobiopsy to release GBM-derived biomarkers and improve the detection sensitivity for two clinically relevant mutations. We achieved localized BBB disruption and the plasma level of GBM biomarkers significantly increased shortly after FUS sonication in the large animal tumor model. Importantly, sonobiopsy improved the detection sensitivity for two mutations without causing off-target damage. This addressed the fundamental limitation—obtaining specimens with a sufficient abundance of circulating tumor biomarkers—for the minimally invasive, sensitive molecular characterization of GBM.

Lastly, we evaluated the impact of sonobiopsy as a platform technology to aid in the diagnosis of other brain diseases. After performing sonobiopsy in a transgenic mouse model of tauopathy, there was a significant increase in the plasma levels of pathologic proteins and a key marker for neurodegeneration. This demonstrated the potential to use sonobiopsy for the noninvasive diagnosis of neurodegenerative disorders.

In summary, this work provided evidence that supports the clinical translation of sonobiopsy as a minimally invasive, spatiotemporally-controlled, and sensitive molecular characterization of brain diseases. This enhanced capability could have an important impact throughout the continuum of patient care from brain disease diagnosis and treatment monitoring to recurrence detection. In addition, sonobiopsy could support the investigation of disease-specific molecular mechanisms and accelerate the development of targeted therapy.

Chapter 1: Introduction and background

1.1 Genomic characterization is crucial for diagnosis and treatment of glioblastoma

Glioblastoma (GBM) is a devastating disease because it is the most common malignant primary adult brain tumor[1] and it has the worst prognosis with a median survival time of 14 months from the time of diagnosis[2,3]. Despite recent advances in understanding GBM, there has not been any significant improvement in treatment options or survival outcome. One of the contributing factors is because GBM is a highly heterogeneous tumor and patients with similar histopathological features have very different responses to the same treatment[4]. However, a recent shift towards genomic characterization is transforming clinical medicine away from the previous model of population risk assessment and empirical treatment towards one focused on individualized care based on molecular classification and targeted therapy.

1.2 Conventional diagnostic workup is limited

The two pillars of diagnostic management of malignant brain tumors are neuroimaging and surgically acquired tissue for pathology and genetic profiling. Current diagnostic evaluation typically relies on magnetic resonance imaging (MRI) and computed tomography to identify suspicious tumor lesions, followed by surgical resection or stereotactic biopsy for histological confirmation and genetic characterization.

1.2.1 Magnetic resonance imaging lacks molecular information

Basic MRI modalities, such as contrast-enhanced T_1-weighted and T_2-weighted scans, provide critical information about the tumor environment for initial diagnosis, surgical planning, and post-treatment management[5]. Advanced MRI modalities, such as diffusion tensor imaging and functional MRI, can identify critical brain areas to guide neurosurgery and minimize postsurgical

neuro-deficits. These imaging features can be very important prognostic indicators, but they lack the genomic information needed to subtype the tumor[6]. Radiomics is an emerging field of medical imaging that converts images to high-dimensional data that may reflect underlying molecular drivers[7]. Though machine learning has been utilized to identify distinctive imaging phenotypes that are unique to different GBM subtypes, the images inherently do not carry molecular information about the genomic profile of the tumor[8,9]. Chemical exchange saturation transfer (CEST) and MR spectroscopy (MRS) are specialized imaging techniques that can assist in the histopathological characterization of brain lesions[10,11]. Thus, radiomics can be a complementary approach to improve accuracy of molecular subtyping and survival prediction, but cannot replace histopathological examination[12,13].

1.2.2 Tissue biopsy poses significant risks and cannot fully capture tumor heterogeneity

Surgical tissue biopsies are the gold standard for molecular characterization. However, these procedures carry significant clinical risk[14], so they cannot be performed for tumors at inoperable locations, or patients who are too ill to tolerate invasive procedures[15]. Given the dynamic nature of these aggressive tumors, a routine interrogation to assess treatment response and cancer recurrence is critically needed. Yet, repeated tissue biopsies are often not feasible given the increased risk for complications and morbidity. In addition, tissue biopsies cannot capture the spatial heterogeneity because the genetic analysis is typically performed for a single tumor region[16].

1.3 Circulating biomarkers provide valuable genetic information

Liquid biopsy (LBx) is a rapid, inexpensive, and minimally invasive approach to obtain clinically relevant information about the tumor[17]. It is a promising approach for the diagnosis,

molecular characterization, and monitoring of extracranial cancer by detecting circulating tumor-derived biomarkers, e.g., DNA, RNA, extracellular vesicles, and proteins shed by tumors into the blood circulation[18–22]. Of particular interest are proteins, messenger RNA (mRNA), cell-free DNA (cfDNA), and circulating tumor DNA (ctDNA).

Proteins have historically been the gold standard for biomarkers because they are relatively abundant compared to circulating nucleic acids[23,24] and are associated with tumor progression[20]. Though protein assays typically have low sensitivity and specificity, multi-protein panels have been developed to reduce false positives and false negatives and improve diagnostic accuracy[25,26].

One of the promising circulating biomarkers is mRNA, which has been used to monitor therapy response and aids in the identification of genetic mutations for GBM[25]. However, it is limited by a relatively low abundance and high instability in the circulatory system[27].

Another potential circulating biomarker is cfDNA, which contains information about molecular/genetic alterations[28,29]. The fragmentation profile of cfDNA may be a valuable readout to screen for early detection because it may be indicative of malignancy[30,31]. In addition, the strong correlation between absolute levels of cfDNA, tumor burden, and therapeutic response suggests that cfDNA has the potential to be a beneficial prognostic biomarker[22].

Tumor-derived cfDNA, i.e., ctDNA, carries information about the dynamics of cancer-specific genetic and epigenetic alternations, is currently the most well-studied and validated biomarker for LBx. There are two potential mechanisms for ctDNA to shed into the blood circulation: passive release through cell death, i.e., apoptosis and necrosis, and active secretion from extracellular vesicles[23,32,33]. Under normal conditions, ctDNA and other

debris are cleared by phagocytes. However, in the presence of a tumor mass or inflammation, this clearance is not performed efficiently[34]. As a result, there is an accumulation of these molecular biomarkers. Then, it follows that disease progression, i.e., tumor burden and tumor cell proliferation, is associated with ctDNA levels[35]. As a result, ctDNA has the potential to be a prognostic biomarker[36]. However, the routine analysis of ctDNA is difficult because of its low abundance: ctDNA makes up less than 0.01% of cfDNA [37,38]. With advanced biomarker detection techniques, the detection rate of ctDNA in GBM patients has improved from <10% to as high as 62% sensitivity[21,29,36,39–41].

1.4 Liquid biopsy for brain tumor diagnosis is limited

Although LBx-guided personalized therapy has already entered clinical practice for the management of several extracranial cancers[42,43], brain tumor-derived molecular biomarkers are generally detected at low abundance and in a limited number of patients, which makes analysis difficult in routine clinical practice[20,36,44,45]. There are two sources of genetic information typically used for detecting brain tumor-derived biomarkers.

1.4.1 Cerebrospinal fluid acquisition may hinder patient diagnosis

Cerebrospinal fluid (CSF) is one source for circulating brain tumor-derived biomarkers. Typically, the CSF has a sufficiently high concentration of circulating biomarkers, such as ctDNA, which can provide an accurate diagnosis[46–48]. However, the total volume of CSF available for LBx is limited, which could hinder the repeatability of CSF-based liquid biopsies[35,49]. Additionally, repeat lumbar punctures to longitudinally characterize the tumor are risky for healthy patients, but can be significantly worse for children, aged, or infirm patients[19]. The invasiveness of the procedure raises safety concerns and the potential risk for developing serious adverse effects in some patients with brain tumors, such as increased

intracerebral pressure[50]. Moreover, CSF-based LBx may not be feasible for tumors with limited DNA shedding to the CSF (e.g., brain tumors that do not contact a CSF compartment or ventricular space)[51].

1.4.2 Blood-based liquid biopsy is limited by low abundance of biomarkers

Though not as sensitive as CSF-based liquid biopsies, blood-based liquid biopsies are less invasive, so the genetic profile is more accessible[35,47,48]. However, the primary challenge facing LBx—low abundance of circulating biomarkers—is underscored in the blood. Though the blood volume is greater than the CSF volume, there is a higher level of background host biomarkers in the blood, which ultimately leads to lower detection rates for the biomarkers of interest[35]. For intracranial tumors, this low sensitivity is exacerbated by the blood-brain barrier (BBB). Current strategies all focus on developing advanced, highly sensitive biomarker detection techniques for analyzing the collected specimens, such as droplet digital PCR (ddPCR)[52], optimized next-generation sequencing (NGS)[53], and advanced spectroscopy[54]. While these techniques are critical in improving sensitivity to the presence of these sparse circulating biomarkers, there is a critical need of techniques that overcome the biophysical barrier that is responsible for this sparsity.

1.5 The blood-brain barrier hinders biomarker release

The BBB is a unique vascular structure in the brain that prevents molecules from non-selectively crossing between the circulating blood and the extracellular fluid of the central nervous system (Figure 1). The BBB protects neural tissues from being exposed to toxins in the blood circulation, but it also hinders the release of brain tumor-derived molecular biomarkers into the bloodstream, resulting in extremely low concentrations of circulating biomarkers[36,55]. Though the vasculature of gliomas is generally leaky, the tumor-associated BBB permeability can be

highly heterogeneous because high-grade gliomas inherently have compromised BBB[56,57], but new vessels may maintain healthy BBB properties and tumor cells may infiltrate the healthy parenchyma where the BBB remains intact[58]. In addition, the clearance of molecular biomarkers, such as ctDNA, is inefficient within a tumor mass, leading to an accumulation of these biomarkers behind the BBB[34]. Thus, there is a need to increase the BBB permeability to ensure sufficient biomarker release for blood-based LBx diagnosis.

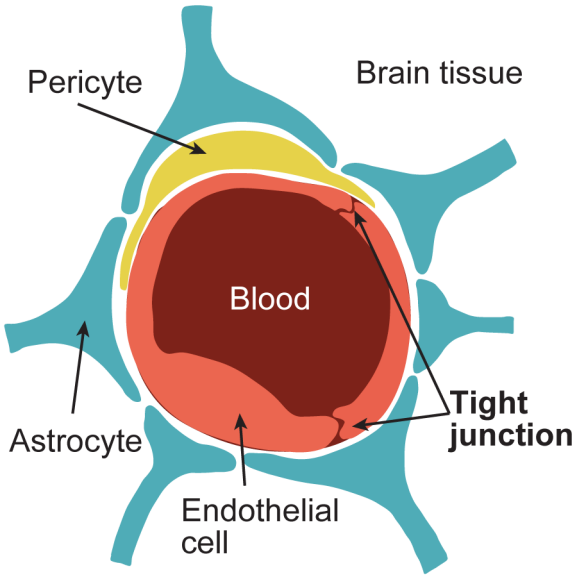

Figure 1. Diagram of blood-brain barrier. The blood vessel is surrounded by endothelial cells, pericytes, and astrocyte feet. The specialized tight junctions between the endothelial cells regulate the diffusion of molecules between the blood vessel and the brain.

1.6 Focused ultrasound is a robust approach to open the BBB

Focused ultrasound (FUS) in combination with microbubbles has been established as a noninvasive technique to disrupt the BBB for drug delivery[59]. Microbubbles, which are ultrasound contrast agents used in the clinic for ultrasound imaging, are intravenously injected into the blood circulation. FUS generated by an extracorporeal ultrasound transducer can penetrate through the skull and focus the ultrasound energy at a targeted brain location. FUS has the potential to target any area in the whole brain with high precision (on the order of millimeter)

in animal models and humans. When microbubbles pass through the FUS target brain region, the ultrasound waves induce microbubble cavitation (i.e., the expansion, contraction, and collapse of microbubbles in an acoustic field). The stable cavitation (SC) of microbubbles localizes and amplifies the FUS acoustic energy to induce mechanical effects on the blood vessel wall[60]. Under high pressures, the microbubbles can experience inertial cavitation (IC), i.e., rapid expansion and violent collapse, which is an indication of tissue damage[61]. Using optimized treatment parameters, FUS can transiently disrupt the BBB and increase its permeability without causing vascular damage. FUS combined with microbubbles is known to improve brain drug delivery in preclinical tumor models[62–64] and non-tumor studies[65–71]. As well as in different species ranging from small animal models to sheep[72], pigs[73–75], nonhuman primates[76–78], and GBM clinical trials[79–85].

1.6.1 High-intensity FUS can release biomarkers from extracranial tumors

Although the use of ultrasound to amplify biomarker signals in the blood was proposed in 2009[86], most previous studies used high-intensity focused ultrasound (HIFU) to induce permanent mechanical or thermal disruption of tumors outside the brain to liberate biomarkers from tumor cells[87–89]. Following the initial introduction of the ultrasound-mediated biomarker amplification concept by D'Souza et al. in 2009, several in vitro studies were reported over the next few years[90–93]. These studies showed that ultrasound combined with microbubble-induced sonoporation could liberate various cellular contents into the extracellular space, such as enhanced green fluorescence protein[90], mammaglobin mRNA[90], micro-RNA 21[91], cancer antigens 125 and 19-9[92], and small molecule calcein[93].

It was only after 2016 that in vivo studies on ultrasound-mediated tumor biomarker release started to be reported[87–89]. Chevillet et al. used pulsed HIFU to induce histotripsy

(i.e., a technique for mechanical tissue fractionation) in a rat model of prostate cancer, and enhanced the release of cell-free tumor microRNA into the blood circulation[87]. Paproski et al. performed the experiment using a chicken embryo tumor model and demonstrated the feasibility of amplifying the release of extracellular vesicles using the mechanical damaging effect induced by HIFU in combination with phase-changing nanodroplets[88]. Souza et al. found significant increases in two protein biomarkers in the plasma of patients treated by HIFU thermal ablation of uterine fibroids[89]. All these previous studies used HIFU to induce permanent mechanical or thermal disruption of the tumor to enhance the release of tumor biomarkers from the tumor cells. The tissue-damaging effect limits the application of these techniques as diagnostic tools in a sensitive organ, such as the brain, and none of these techniques could resolve the BBB challenge inherent to brain tumors.

1.6.2 Sonobiopsy can release biomarkers from brain tumors

Sonobiopsy was developed to advance the diagnosis of brain cancer and is different from all previously reported strategies. Sonobiopsy combines low-intensity pulsed FUS with microbubbles to overcome the unique challenge that the BBB poses on the efficient passage of tumor biomarkers from the brain into the peripheral circulation (Figure 2). We hypothesized that FUS-induced BBB disruption enabled “two-way trafficking” between the brain and bloodstream by demonstrating the feasibility of sonobiopsy with a mouse GBM model[94]. In that study, sonobiopsy was performed after intracerebral implantation of glioma cells expressing the enhanced green fluorescent protein (eGFP). While circulating agents were allowed to enter the brain using FUS-mediated BBB disruption, brain tumor-derived biomarkers – eGFP mRNA – were also released into the blood circulation to improve the sensitivity of blood-based LBx.

1.7 Sonobiopsy enables noninvasive, sensitive, molecular diagnosis

Due to the limitations and risks associated with conventional diagnostic evaluation, genetic heterogeneity of GBM, and the low abundance of circulating biomarkers, there is a clinical need for a minimally invasive, spatiotemporally-controlled approach to improve the sensitive molecular characterization of brain cancer. Sonobiopsy has the potential to fulfill these unmet needs.

Sonobiopsy is minimally invasive and only requires intravascular access to inject FDA-approved microbubbles and collect blood, both of which are standard procedures in patient care. Leveraging these established, minimally invasive techniques to disrupt the BBB, sonobiopsy can enhance the sensitivity in the detection of tumor mutations by increasing biomarker release. By retrospectively analyzing blood samples collected from FUS-mediated drug delivery clinical trials, Meng et al. provided preliminary clinical evidence that FUS-induced BBB disruption increased the concentrations of circulating biomarkers (cell-free DNA, neuron-derived extracellular vesicles, and brain-specific protein)[84]. Although promising, there is a lack of compelling evidence that demonstrates the capability of sonobiopsy in improving the diagnostic sensitivity of brain tumor-specific genetic mutations compared with conventional blood-based LBx. Meng et al. detected IDH1-R132H mutation in one patient, who was known to harbor the tumor mutation. However, this did not address the critical question of whether sonobiopsy could enhance the sensitivity in the detection of tumor mutations, which was one of the goals of this dissertation.

Though, recent advances to improve the sensitivity of blood LBx without disrupting the BBB have been fruitful[18], sonobiopsy provides spatially targeted and temporally controlled sample collection that conventional blood LBx cannot offer. Blood LBx reflects the global molecular status, i.e., coexistence of different genotypic profiles, but is inherently spatially

agnostic and cannot spatially resolve the genetic information[95,96]. On the other hand, FUS can precisely delivered acoustic energy to a discrete target with high lateral resolution to release biomarkers confined within that location. Therefore, sonobiopsy has the potential to provide more granularity to the GBM diagnosis by targeting different tumor sites and identifying the molecular profile unique to each spatial location[16,22,97]. Meanwhile, the level of circulating biomarkers is determined by a balance between biomarker release and clearance processes[98,99]. Sonobiopsy can not only enrich the concentration of circulating biomarkers, but also minimize the effect of clearance by collecting the blood samples immediately after biomarker release.

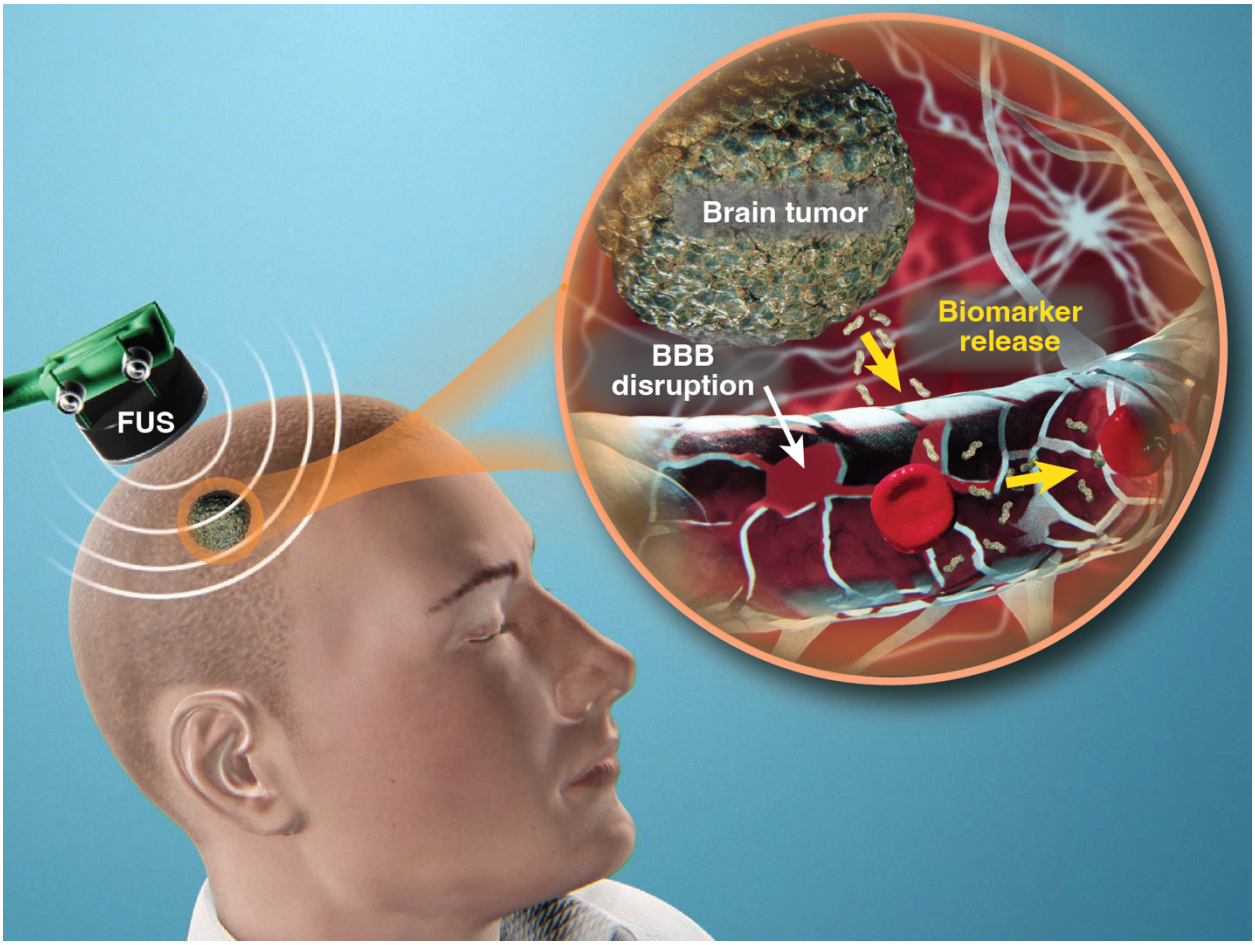

Figure 2. Mechanism of sonobiopsy. FUS sonication focuses the ultrasound energy at the target location. Microbubbles (MB) are intravenously injected and circulate throughout the body until it reaches the target area. The ultrasound waves induce MB cavitation (left), which elicits mechanical perturbation on the vessel wall to disrupt the tight junctions and increase BBB permeability (right).

1.8 Objective of work

There are unique advantages that sonobiopsy offers to the management of GBM patients. Thus, the objective of this dissertation was to evaluate the feasibility, safety, and efficacy of sonobiopsy in preclinical animal models to support future clinical applications. Specifically, evidence showing the safe release of tumor-derived biomarkers and the subsequent increase in detection sensitivity is critically needed to establish the potential for clinical translation. In Chapter 2, we will use an established mouse GBM model to optimize the parameters for safe and effective sonobiopsy. Then, we will use these optimized sonobiopsy parameters to determine the feasibility of improving the detection sensitivity for clinically relevant mutations in a mouse GBM model. In Chapter 3, we will develop a sonobiopsy system for large animals and evaluate the safety and feasibility to release brain-specific biomarkers from a non-tumor pig model. In Chapter 4, we will develop a pig GBM model and assess the ability of sonobiopsy to safely release tumor-derived biomarkers and improve the detection sensitivity for clinically relevant GBM mutations. Lastly, in Chapter 5, we will evaluate the potential to use sonobiopsy for the noninvasive diagnosis of neurodegenerative diseases.

Chapter 2: Evaluate feasibility, efficacy, and safety of sonobiopsy in mouse GBM model

2.1 Abstract

The objectives for this chapter were to optimize the parameters for safe and effective sonobiopsy, and then use these optimized sonobiopsy parameters to determine the feasibility for improving the diagnostic sensitivity of brain tumor-specific genetic mutations compared with conventional blood-based liquid biopsy. MRI-guided FUS sonication was performed to locally enhance the BBB permeability of the GBM tumor. Contrast-enhanced T_1-weighted MR images were acquired to evaluate the BBB permeability change. Blood was collected immediately after FUS sonication and droplet digital PCR was used to quantify the levels of brain tumor-specific genetic mutations in the ctDNA. Histological staining was performed to evaluate the potential for off-target tissue damage. The optimal sonobiopsy parameters to significantly increase biomarker release and reduce the risk for tissue damage were 1.0 MPa FUS pressure, 5× microbubble dose, and collect the blood within 10 minutes post-FUS. Sonobiopsy significantly increased the levels of EGFRvIII ctDNA ($p = 0.0056$) and TERT C228T ctDNA ($p = 0.04$). Subsequently, the diagnostic sensitivity of EGFRvIII improved from 7.14% to 64.71% and that of TERT C228T improved from 14.29% to 45.83%. Sonobiopsy has the potential to provide a sensitive molecular diagnosis of GBM without surgery. The long-term goal is to translate sonobiopsy to influence clinical decisions and improve patient care.

2.2 Determine optimal parameters for safe biomarker release in a mouse glioma model

In the first study demonstrating the potential of sonobiopsy[94], the acoustic pressures used were intentionally selected to be relatively high (1.52–3.53 MPa) to increase the chance of success in releasing biomarkers. As expected, hemorrhage was found in the FUS-targeted brain area in that

study. Thus, it is critical to evaluate the relationship between FUS pressure, biomarker release, and hemorrhage density to balance sufficient biomarker release with minimal tissue damage.

The microbubble (MB) dose may further increase the success rate for FUS-induced biomarker release. It was demonstrated that increasing the MB dose safely increases successful BBB disruption for drug delivery applications[78,100,101]. However, increasing the MB dose has led to safety concerns, such as astroglial activation and glial scar formation[102]. So, there is a need to identify the MB dose that will enhance biomarker release without causing significant safety risks.

It is imperative to the success of sonobiopsy to not only enhance the efficient transfer of tumor-specific biomarkers across the BBB but also collect the blood samples in a reasonable timeframe for sensitive detection. Different biomarkers have various circulating half-lives that are further complicated by its context-dependence. For example, circulating tumor DNA (ctDNA) has a half-life of approximately 2 hours[103]. Cell-free DNA (cfDNA) has a half-life between 16 minutes and 2.5 hours depending on the patient's state (e.g., before/after surgery, resting/exercising)[104]. Messenger RNA (mRNA) levels decrease dramatically within 30 minutes[105,106]. Thus, biomarker detection can be enhanced by stimulating their release from the tumor to the circulation and precisely controlling the blood-collection time to be shorter than their lifetimes in the blood.

2.2.1 Methods

Animal preparation

All animal studies were reviewed and approved by the Institutional Animal Care and Use Committee of Washington University in St. Louis in accordance with the National Institutes of Health Guidelines for Animal Research.

Mice (Strain 550, age:6–8 weeks, Charles River Laboratory, Wilmington, MA, USA) were implanted with GL261 murine glioblastoma cells on day 0 with an established protocol[94]. Briefly, the tumor implantation location was 2 mm posterior to the bregma and 1.5 mm lateral to the midline. The growth of the tumor was monitored using a dedicated 4.7T small animal MRI system (Agilent/Varian DirectDrive^{TM} console, Agilent Technologies, Santa Clara, CA, USA). After the first 7 days, T_1-weighted and T_2-weighted MRI scans were acquired every 3 days to monitor tumor growth and changes in neuroanatomy.

The mice were anesthetized with 2% diluted isoflurane (vaporized in oxygen 1 L/min) and placed in a small animal cradle with an MRI saddle coil (Image Guided Therapy, Pessac, France) and stabilized with a bite bar and ear bars (Figure 3A). The rectal temperature was monitored throughout the experiment and maintained at 37°C. Ultrasound gel was carefully placed atop the mouse head after the hair was removed with a depilatory cream (Nair, Church & Dwight Co., NJ, USA). Degassed water filled the FUS transducer's water balloon to ensure sufficient acoustic coupling.

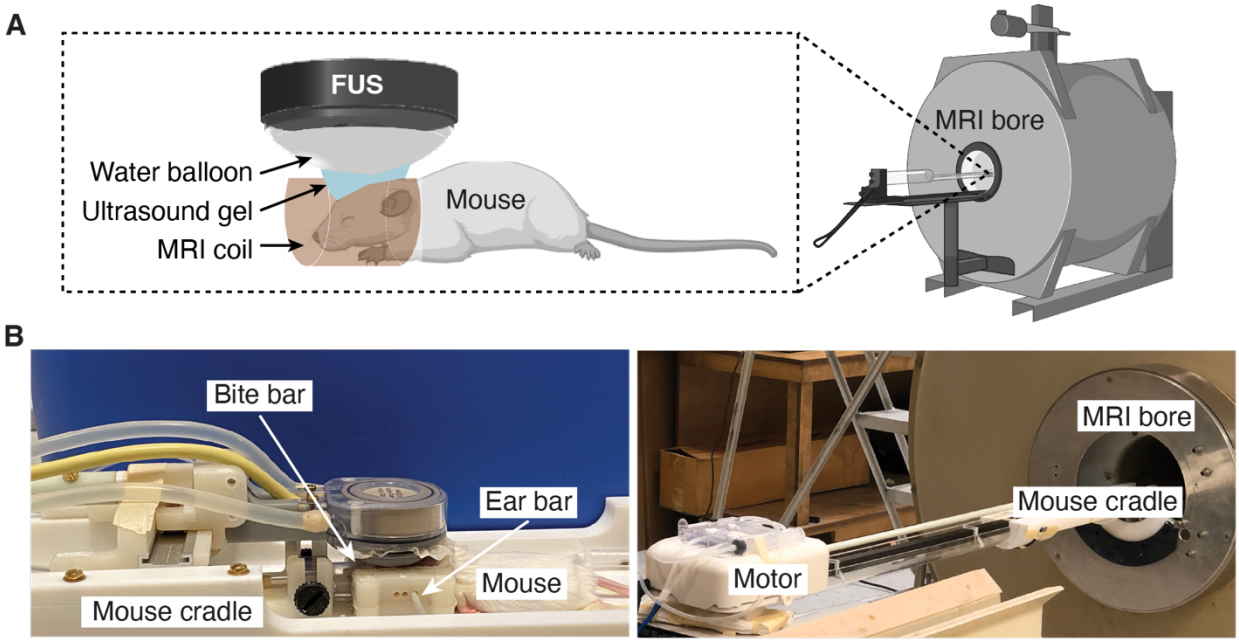

Figure 3. Experimental setup for sonobiopsy in mice. (A) Hardware setup for MRI-guided sonobiopsy in mice. The FUS transducer was coupled with the mouse head using ultrasound gel and a bladder filled with degassed water. (B) The mouse head was fixed in the MRI coil that was built into the mouse cradle using a bite bar and ear bars. (C) An MRI-compatible motor was attached to the mouse cradle to mechanically move the transducer to the planned target.

The mice were randomly assigned to different groups once the diameter of the tumor reached 2 mm in any direction, approximately 10 days, as measured by contrast-enhanced T_1-weighted scans (Table 1). First, the blood collection time was optimized based on which time point maximized the levels of circulating biomarkers. The first three groups had their blood collected either 10 min, 30 min, or 60 min post-FUS. The optimal time was then used for the rest of the experiment. Second, the optimal FUS pressure was evaluated by finding a compromise between increased concentration in biomarkers and FUS-induced tissue damage. The three groups for varying FUS pressure were sonicated at either 0.5 MPa, 1.0 MPa, or 1.5 MPa. The optimal pressure was selected and used for the remainder of the study. Third, the MB dose was optimized by comparing biomarker levels in the blood with FUS-induced tissue damage. The three groups for optimizing MB dose were either 8×10^8 MB/mL (1×), 40×10^8 MB/mL (5×), or 80×10^8 MB/mL (10×). The control group received no treatment, but the process of MRI acquisition and blood collection remained consistent. The groups 2, 5, and 8 were grouped together because their parameters were similar (10 min, 0.5 MPa, 1×).

Table 1. Study groups for sonobiopsy parameter optimization.

Group	# of animals	Blood collection time	FUS pressure	MB dose
1	6	10 min	–	–
2	4	**10 min**	0.5 MPa	20 μL/kg (1×)
3	4	**30 min**	0.5 MPa	20 μL/kg (1×)
4	2	**60 min**	0.5 MPa	20 μL/kg (1×)
5	4	10 min	**0.5 MPa**	20 μL/kg (1×)
6	5	10 min	**1.0 MPa**	20 μL/kg (1×)
7	6	10 min	**1.5 MPa**	20 μL/kg (1×)
8	4	10 min	0.5 MPa	**20 μL/kg (1×)**
9	5	10 min	0.5 MPa	**100 μL/kg (5×)**
10	5	10 min	0.5 MPa	**200 μL/kg (10×)**

Sonobiopsy sonication

The FUS transducer (Imasonics, Voray sur l'Ognon, France) was an 8-element annular array with a center frequency of 1.5 MHz. Prior calibration was performed in a water bath with a capsule hydrophone (Onda HGL-0200, Sunnyvale, CA, USA). The axial and lateral full-width at half-maximums were 5.5 mm and 1.2 mm, respectively. Pressure values were derated to account for the 18% mouse skull attenuation[107]. The FUS transducer was connected to an MRI-compatible piezoelectric motor to mechanically move the transducer in the lateral and anterior-posterior directions (Figure 3B). The annular array design allowed the FUS transducer to electronically steer the focus in the dorsal-ventral direction.

Coronal and axial T_2-weighted fast spin-echo MRI scans were acquired to image the mouse head and locate the geometrical focus of the transducer (repetition time (TR): 2000 ms; echo time (TE): 52 ms; slice thickness: 0.5 mm; in-plane resolution: 0.25×0.25 mm^2; matrix size: 128×128; averages: 4). The MRI images were imported to a software program (ThermoGuide, Image Guided Therapy, Pessac, France) to locate the focus of the transducer via 3-point triangulation. The transducer was moved to the tumor center for FUS sonication.

A 1:10 dilution of the gadolinium-based contrast agent, Dotarem (Gd-DOTA), and saline was intravenously injected through the tail vein. Gd-DOTA is too large to cross an intact BBB. Thus, the hyper-enhancement in the T_1-weighted images would indicate BBB disruption. A pre-FUS coronal T_1-weighted gradient echo MRI scan was performed to visualize the tumor-induced BBB permeability (TR/TE: 108/4 ms; slice thickness: 0.5 mm; in-plane resolution: 0.25×0.25 mm^2; matrix size: 128×128; averages: 16).

As previously described, microbubbles were prepared in-house to a mean diameter of 4–5 μm and diluted based on the treatment group[94]. A bolus of the MB solution was intravenously injected and flushed with saline. FUS sonication was performed 1 minute later (frequency: 1.5 MHz, pulse repetition frequency: 5 Hz, duty cycle: 3.35%, pulse length: 6.7 ms, treatment duration: 1 min).

A post-FUS coronal T_1-weighted gradient echo MRI scan was performed (with the same parameters as pre-FUS T_1-weighted sequence) to quantify the FUS-induced changes in BBB permeability.

Plasma eGFP mRNA level quantification

Depending on the treatment group, blood samples were collected from the heart 10 min, 30 min, or 60 min post-FUS. The methods of quantitative polymerase chain reaction (qPCR) analysis of eGFP mRNA have been described in our previous publication[94]. Briefly, RNA was extracted from the plasma samples using miRNeasy serum/plasma kit (Catalog no. 217184, Qiagen, USA) followed by Agencourt RNAClean XP beads (Catalog no. A63987, Beckman Coulter Inc., USA). Extracted RNA was then converted to cDNA using the Applied Biosystems high-capacity cDNA reverse transcription kit (Catalog no. 4368814, Thermo Fisher Scientific, USA). 5.8S rRNA was used as the internal control to normalize the PCR data by calculating the cycle

threshold change (ΔCT) by subtracting CT of the eGFP ($C_{T,eGFP}$) by the CT of the housekeeping gene, 5.8s rRNA ($C_{T,5.8S}$). The relative gene expression level was determined using the $2^{-\Delta CT}$ method.

MRI analysis

The BBB permeability was assessed by comparing the change in contrast-enhanced volume with a custom semi-automated MATLAB (The MathWorks Inc., Natick, MA, USA) script. First, a mask was used to differentiate the brain from the skull. Second, circular ROIs (diameter: 3 mm) was drawn around the contrast-enhanced area indicative of Gd-DOTA extravasation and the contralateral non-FUS site. Third, the contrast-enhanced volume (CE volume) was calculated from the sum of voxels in the treated area for each image slice that had an intensity greater than 3× standard deviations above the mean intensity within the non-FUS area. The change in CE volume (ΔCE volume) was the difference between the post-FUS and pre-FUS CE volumes.

Histological analysis

After blood collection, mice were deeply anesthetized through 5% diluted isoflurane (vaporized in oxygen 1 L/min) and the heart was exposed. The heart was first perfused with 0.01 M phosphate-buffered saline followed by 50 mL of 4% paraformaldehyde once the blood began to run clear. Brains were harvested and prepared for paraffin sectioning. The mouse brains were horizontally sectioned to 15 μm slices and used for H&E staining to examine red blood cell extravasation and cellular injury. The brain slices were digitally acquired with the Axio Scan.Z1 Slide Scanner (Zeiss, Oberkochen, Germany). QuPath v0.1.3[108] was used to detect areas of microhemorrhage. After color deconvolution (hematoxylin vs. eosin), areas of microhemorrhage were detected using the positive-pixel count algorithm. The microhemorrhage density was

calculated as the percentage of positive pixel area over the total stained area in the respective ROI.

Statistical analysis

Where appropriate, the data was analyzed with the paired t-test (Figure 4B) in Prism 9 (GraphPad, San Diego, CA, USA). To analyze significance across multiple comparisons, the Kruskal-Wallis test and post hoc Dunn's test with Bonferroni correction was performed (Figure 5A-F, H, I). Statistical differences were considered significant (*) when $p < 0.05$, (**) when $p < 0.01$, (***) when $p < 0.001$, and (****) when $p < 0.0001$. Descriptive statistics is represented as mean ± SD.

2.2.2 Results

FUS successfully disrupted BBB with lowest FUS pressure and MB dose

Contrast-enhanced (CE) T_1-weighted MRI scans (Figure 4A) were acquired to assess tumor growth and evaluate FUS-induced BBB disruption. The average tumor volume for groups 2–4 was 12.28 ± 6.51 mm^3. FUS significantly increased (p = 0.0013) the average volume of tissue with enhanced BBB permeability by approximately 1.5-fold (Figure 4B).

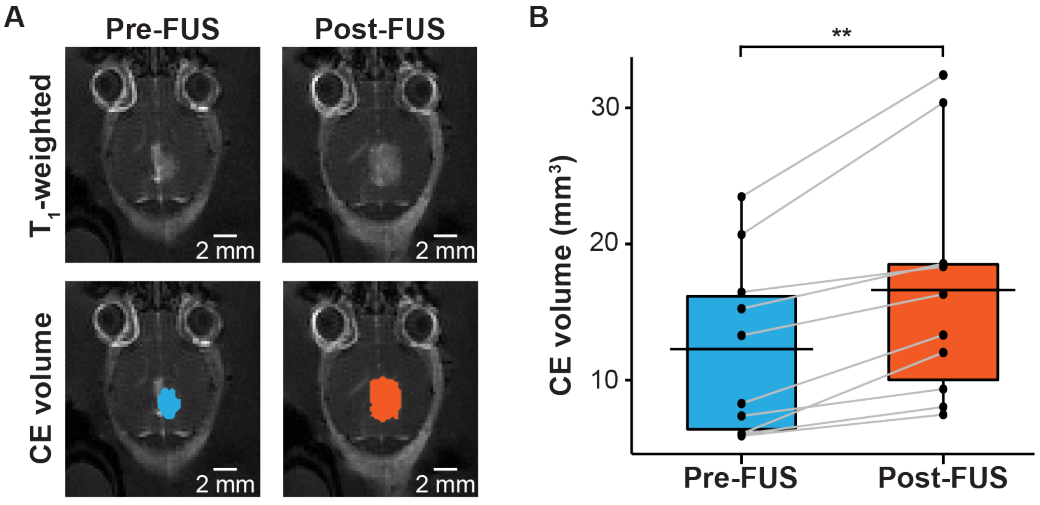

Figure 4. FUS-induced BBB disruption was achieved in mouse tumor model. (A) Contrast-enhanced (CE) volumes for mice in groups 2–4 (0.5 MPa, 1× MB dose) were acquired before FUS to quantify the tumor volume (blue area). Post-FUS coronal MRI scans confirmed FUS-induced BBB disruption (orange area) as an increase in CE volume. (B) FUS significantly increased the CE volume ($n = 10$; $p = 0.0013$; $^{**}p < 0.05$; paired t-test) from 12.28 ± 6.51 mm^3 to 16.62 ± 8.74 mm^3. Black bars indicate mean in B.

FUS-induced BBB disruption dependent on FUS parameters

The change in CE volume (ΔCE volume) was not significantly different between each of the treatment groups with different blood collection times compared with one another ($p = 0.87$) (Figure 5A). The average ΔCE volume was 4.38 ± 3.41 mm^3 for the 10-min group, 4.21 ± 3.71 mm^3 for the 30-min group, and 4.50 ± 2.08 mm^3 for the 60-min group. There was no significant difference between each group ($p_{10,30} = 1.0$, $p_{10,60} = 1.0$, $p_{30,60} = 1.0$; post hoc Dunn's test with Bonferroni correction). With increasing FUS pressure, there was a nonsignificant trend where higher pressures led to higher ΔCE volumes ($p = 0.06$) (Figure 5B). The average ΔCE volume was 4.38 ± 3.41 mm^3 for the 0.5 MPa group, 7.14 ± 4.91 mm^3 for the 1.0 MPa group, and 11.53 ± 4.48 mm^3 for the 1.5 MPa group. There was no significance between each group ($p_{0.5,1.0} = 1.0$, $p_{0.5,1.5} = 0.06$, $p_{1.0,1.5} = 0.37$; post hoc Dunn's test with Bonferroni correction). With increasing MB dose, there was no significant difference in ΔCE volume between each treatment group ($p = 0.16$) (Figure 5C). The average ΔCE volume was 4.38 ± 3.41 mm^3 for the 1× group, 3.82 ± 0.98 mm^3 for the 5× group, and 8.62 ± 5.65 mm^3 for the 10× group. There was no significance between each group ($p_{1\times,5\times} = 1.0$, $p_{1\times,10\times} = 0.42$, $p_{5\times,10\times} = 0.23$; post hoc Dunn's test with Bonferroni correction).

Increased release of biomarkers at early blood collection times

The plasma eGFP mRNA level at 10-min post-FUS blood was significantly greater (474-fold increase) than the untreated blood LBx level (Figure 5D).

Increased release of biomarkers at higher FUS pressures

When mice were treated with 1.0 MPa, the plasma eGFP mRNA level was significantly greater (9,694-fold increase) than the blood LBx level (Figure 5E). Additionally, mice treated with 1.5 MPa had a significantly greater eGFP mRNA level compared with the blood LBx group (26,514-fold increase).

Increased release of biomarkers at higher MB doses

When mice were treated with 5× microbubble dose, the plasma eGFP mRNA level was significantly greater (17,790-fold increase) than the blood LBx level (Figure 5F). Additionally, mice treated with 10× microbubble dose had a significantly greater eGFP mRNA level compared with the blood LBx group (18,208-fold increase).

Increased risk of damage for higher FUS pressures and MB doses

Hemorrhage was observed at the target site (Figure 5G). However, there was no significant difference between each of the treatment groups with higher FUS pressures ($p = 0.13$) or higher MB doses ($p = 0.10$). The hemorrhage density was 0.70 ± 0.02 pixels/μm^2 in the blood LBx group, 2.09 ± 0.94 pixels/μm^2 in the 0.5 MPa group, 3.12 ± 0.85 pixels/μm^2 in the 1.0 MPa group, and 6.05 ± 5.56 pixels/μm^2 in the 1.5 MPa group. There was a nonsignificant trend where higher FUS pressures led to more tissue damage ($p_{blood,0.5} = 1.0$, $p_{blood,1.0} = 0.42$; $p_{blood,1.5} = 0.15$; post hoc Dunn's test with Bonferroni correction) (Figure 5H). Similarly, there was a nonsignificant trend where higher MB doses led to more tissue damage ($p_{blood,1\times} = 1.0$, $p_{blood,5\times} = 0.25$; $p_{blood,10\times} = 0.14$; post hoc Dunn's test with Bonferroni correction) (Figure 5I). The hemorrhage density was 0.70 ± 0.02 pixels/μm^2 in the blood LBx group, 2.09 ± 0.94 pixels/μm^2 in the 1× group, 2.14 ± 0.70 pixels/μm^2 in the 5× group, and 1.47 ± 0.51 pixels/μm^2 in the 10× group.

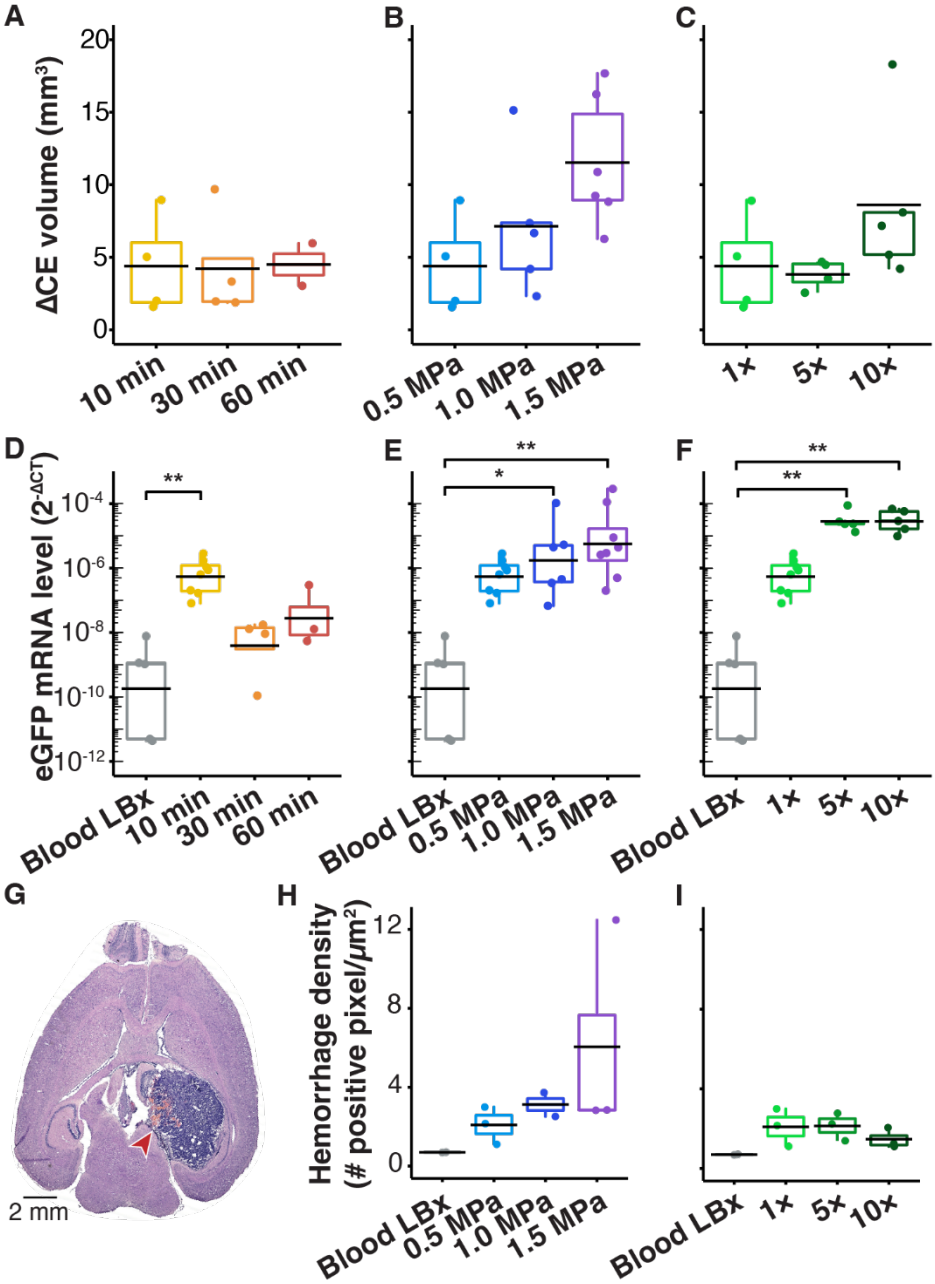

Figure 5. Sonobiopsy parameters were optimized to maximize biomarker release and minimize tissue damage. (A) There was no significant difference between different blood collection times ($p = 0.87$). (B) Higher FUS pressures non-significantly increased ΔCE volume ($p = 0.06$). (C) Increasing MB dose did not significantly increase ΔCE volume ($p = 0.16$). (D) There was a significant increase in eGFP mRNA level when the blood was collected within 10 minutes post-FUS ($n = 8$; $p_{blood,10} = 0.0015$; $^{**}p < 0.01$). € FUS pressures of 1.0 MPa ($n = 6$; $p_{blood,1.0} = 0.030$; $^{*}p < 0.05$) and 1.5 MPa ($n = 8$; $p_{blood,1.5} = 0.0013$; $^{**}p < 0.01$) significantly increased eGFP mRNA plasma level. (F) There was a significant increase in eGFP mRNA level when the mice were treated with 5× ($n = 5$; $p_{blood,5\times} = 0.0019$; $^{**}p < 0.01$) and 10× microbubble doses ($n = 5$;

$p_{blood,10\times} = 0.0017$; $^{**}p < 0.01$). (G) Representative whole-brain horizontal slice shows tumor (dark purple area) and hemorrhage (red area with red arrow). (H) There was no statistical difference in the extent of tissue damage, as indicated by hemorrhage density, between each of the treatment groups with different FUS pressures ($p = 0.13$). (I) There was no significant difference in hemorrhage density for different microbubble doses ($p = 0.10$). Statistical analysis was performed with Kruskal-Wallis multiple comparison test and post hoc Dunn's test with Bonferroni correction. Black bars indicate mean in A-F, H, and I.

2.2.3 Discussion

The robustness of our technique to disrupt the BBB for biomarker release is demonstrated through consistent hyper-enhancement at a constant FUS pressure and MB dose (Figure 5A). Sonobiopsy depends not only on successful BBB disruption to enhance the release of biomarkers, but also on sensitive detection of the biomarkers. The results from our study suggest that the time delay between FUS treatment and blood collection is pivotal to successful detection of FUS-induced biomarkers. The level of eGFP mRNA detected was significantly higher within 10 minutes post-FUS. The reason for this may be the short circulation half-life of the tumor-specific mRNA. It is possible that the clearance time for tumor-specific mRNA is similar to that of other mRNA biomarkers where the plasma levels decrease drastically within 30 minutes[105,106]. Thus, future translation of sonobiopsy must account for this narrow window of sensitive detection of biomarkers in the plasma.

The FUS pressure must also be considered during treatment planning. Our results demonstrated that a low pressure of 0.5 MPa increased the levels of biomarker in the blood by multiple orders of magnitude (470×), which may be an acceptable improvement over conventional liquid biopsies that detect a tumor-specific mRNA in a patient at levels 10–50× greater than the levels in a healthy control[109–112]. However, increasing the pressure to at least 1.0 MPa significantly increased the biomarker levels over the control group. Increasing FUS pressure is known to increase the volume of BBB disruption[100,113,114]. The positive trend for

hyper-enhancement volume demonstrated here is similar to the positive trend for eGFP mRNA levels. So, MRI scans can not only be used to verify the success of FUS-induced BBB disruption but also be indicative of the successful release of biomarkers into the blood circulation. The lower pressure may be beneficial from a safety standpoint to minimize the FUS-induced tissue damage while still enhancing the efficient release of biomarkers.

Our results suggest that the MB dose used during FUS sonication is an additional parameter for consideration. A 1× MB dose increased the eGFP mRNA levels by 470×. However, FUS sonication with either a 5× or 10× MB dose significantly increased the eGFP mRNA levels compared with the control group. This may be because a higher microbubble dose increases the harmonic emission, which increases the success rate for BBB disruption[78]. It is also known that increasing the microbubble dose increases the volume of BBB disruption[115]. The amount of FUS-induced hemorrhage did not change significantly with the different MB doses. Thus, while the MB dose may be important for BBB disruption and biomarker release, it does not have a significant role in tissue damage, in contrast with FUS pressure.

We analyzed the correlations between biomarker release and contrast enhancement. There was no significant correlation observed between eGFP mRNA level and ΔCE volume for different FUS pressures (n = 15, Pearson's correlation coefficient r = -0.21, p = 0.45) or for different MB doses (n = 13, r = -0.036, p = 0.91). The lack of a strong correlation suggests that FUS-induced biomarker release is a complex process that may be affected by many variables, such as the tumor microenvironment, and/or a larger sample size with more groups is needed to detect these correlations.

This study did have several limitations. First, the tumor volume was not well controlled because of the variability in tumor growth between subjects and the limited

availability of the MRI scanner to perform sonobiopsy at specific times. It is possible that the tumor properties, such as overall volume, presence of a necrotic core, and tumor vasculature have a role in biomarker release and sonobiopsy. Future work will utilize strict controls over tumor volume to reduce variability from the tumor microenvironment. Second, the biomarker release was only evaluated with mRNA. The dependence on the detection of a single biomarker may lead to false positive and false negative diagnoses in the clinic. To address this, we will evaluate the plasma levels of other biomarkers that will provide additional information on the brain tumor, such as cfDNA and ctDNA, in Chapter 2.3. Third, there are strategies that may improve sonobiopsy-induced release. We will evaluate whether multi-point sonication for large volume BBB disruption or passive cavitation detection (PCD) feedback is helpful for biomarker release in Chapter 2.3.

2.2.4 Conclusion

This study demonstrated the effects that blood collection time, FUS pressure, and MB dose have on the efficacy of tumor-specific biomarker release and the extent of associated hemorrhage to optimize the sonobiopsy technique. The blood should be collected within 10 minutes to maximize the biomarker levels in the plasma. Though FUS pressure as low as 0.5 MPa will increase the biomarker release, 1.0 or 1.5 MPa will significantly increase the plasma level of biomarkers. However, these pressures are associated with a higher burden of FUS-induced hemorrhage. In addition, a MB dose of 8×10^8 MB/mL will be sufficient to enhance biomarker release, but a dose greater than 40×10^8 MB/mL will significantly increase the level of biomarkers. This study suggests that careful optimization of FUS parameters will improve the potential for sonobiopsy to be a safe, sensitive technique to diagnose brain tumors.

2.3 Assess detection sensitivity for clinically relevant brain tumor mutations

The stage of tumor growth may be an important consideration when deciding whether sonobiopsy will be an effective diagnostic approach. GBM is one of the highest vascularized tumors and because it is a grade IV glioma, the BBB is inherently compromised[56]. When the tumor is small, for early-stage cancer, there are fewer tumor cells, and subsequently, there may be fewer molecular biomarkers available to be released into the blood circulation than larger tumors. As a result, it is important to understand whether sonobiopsy will be effective at increasing the biomarker yield for small tumors.

As the tumor grows, the inherently inefficient microcirculation, due to parenchymal edema and the compromised BBB[116], worsens and parts of the tumor may become more avascular and necrotic[117]. However, it has been conjectured that significant alterations in BBB permeability—that would enable significant biomarker release—are not linked with tumor size[56]. This was validated by two studies where there was no significant correlation between tumor volume and cfDNA[118,119]. Fontanilles et al. observed that the cfDNA level was not associated with tumor volume, but was correlated with relative cerebral volume, which is an indicator of tumor neoangiogenesis. Nabavizadeh et al. found that there was a threshold for BBB permeability, i.e., washout rate constant of contrast agent from extravascular extracellular space to the intravascular space, above which there is a positive correlation between cfDNA and tumor volume. The evidence from these two studies suggest that biomarker release is dependent on a sufficient level of BBB permeability, but not necessarily influenced by further disruptions, such as tumor growth. As a result, it may still be necessary to apply sonobiopsy on a large tumor to increase the BBB permeability above the threshold for efficient biomarker release. Given that the basis of sonobiopsy is the FUS-induced increase in BBB permeability and depends on intact

vasculature for microbubble delivery and biomarker release into the bloodstream, it is critical to understand whether sonobiopsy will work in large tumors.

Large volume sonication is a common technique used in FUS-induced drug delivery to steer to different targets during a single sonication with the goal of delivering therapeutic molecules to large regions of the brain[78,120]. Large volume BBB disruption has been achieved in preclinical models [74,121–126] and is currently the standard for clinical trials[83,84,127–130]. Under the two-way trafficking hypothesis, it stands that large volume sonication will also improve the yield of sonobiopsy by increasing the BBB permeability over a large, sonicated region to maximize FUS-induced biomarker release.

2.3.1 Methods

Animal preparation

All animal procedures were reviewed and approved by the Institutional Animal Care and Use Committee at Washington University in St. Louis in accordance with the Guide for the Care and Use of Laboratory Animals and the Animal Welfare Act.

Human GBM cells (U87) with EGFRvIII overexpression (U87-EGFRvIII^{+}) and carrying TERT C228T mutation[131] were used to establish the mouse model of GBM with clinically relevant mutations. The U87-EGFRvIII^{+} cells were kindly provided by Dr. Frank Furnari from the University of California at San Diego[132]. The cell line was cultured as an adherent monolayer in DMEM supplemented with 10% fetal bovine serum, 2 mmol/L l-glutamine, and 100 units/mL penicillin. The cells were maintained at 37°C in a humidified CO_2 (5%) atmosphere and the medium was changed as needed. Prior to implantation, cells were dispersed with a 0.05% solution of trypsin/EDTA and adjusted to concentrations needed for tumor implantation.

Immunodeficient mice (strain: NCI Athymic NCr-nu/nu, age: 6–8 weeks, Charles River Laboratory, Wilmington, MA, USA) were used to generate the xenograft GBM model. Briefly, mice were anesthetized and the head was fixed on a stereotactic device for injection of the tumor cells. Cells were injected and the tumor growth was monitored using a dedicated 4.7T small animal MRI system (Agilent/Varian DirectDrive^{TM} console, Agilent Technologies, Santa Clara, CA, USA). Starting at 7 days and continuing every 3 days thereafter, MRI scans were acquired to monitor tumor growth and changes in neuroanatomy.

Sonobiopsy sonication

The MRI-compatible FUS transducer (Imasonics, Voray sur l'Ognon, France) was made of a 7-element annular array with a center frequency of 1.5 MHz, an aperture of 25 mm, and a radius of curvature of 20 mm. The axial and lateral full width at half maximums (FWHM) of the FUS transducer were 5.5 mm and 1.2 mm, respectively. Pressure values were derated to account for the 18% mouse skull attenuation[107]. A catheter was placed in the mouse tail vein for intravenous injection.

Coronal and axial T_2-weighted MRI scans were acquired to image the mouse head and locate the geometrical focus of the transducer (same parameters as aforementioned T_2-weighted sequence used to monitor tumor growth). The MRI images were imported to a software program (ThermoGuide, Image Guided Therapy, Pessac, France) to locate the focus of the transducer via 3-point triangulation. The transducer was moved to the tumor center for FUS sonication. A pre-FUS axial T_1-weighted MRI scan was performed to visualize the tumor-induced BBB permeability (same parameters as aforementioned T_1-weighted sequence used to monitor tumor growth) after intravenous injection of MR contrast agent gadoterate meglumine

(Gd-DOTA; Dotarem, Guerbet, Aulnay sous Bois, France) at a dose of 1 mL/kg diluted 1:1 in 0.9% saline.

Definity microbubbles (Lantheus Medical Imaging, North Billerica, MA, USA) at a dose of 100 µL/kg (5× clinical MB dose) were injected intravenously to the mice. FUS sonication started 15 seconds prior to microbubble intravenous injection (frequency: 1.5 MHz, pressure: 1.0 MPa, pulse repetition frequency: 5 Hz, duty cycle: 3.35%, pulse length: 6.7 ms, treatment duration: 3 min). FUS sonication was performed at 3 points, evenly spaced apart by 0.5 mm, to enable coverage of the entire tumor volume.

After sonication, Gd-DOTA was re-injected and a post-FUS axial T_1-weighted MRI scan was performed (same parameters as pre-FUS T_1-weighted sequence) to quantify the FUS-induced changes in BBB permeability.

Mouse plasma isolation

Mouse whole blood (~500 µL) was collected via cardiac puncture using BD Vacutainer K_2 EDTA tubes (Becton Dickinson, Franklin Lakes, NJ, USA). Within 4 hours of collection, samples were centrifuged at 3000×*g* for 10 minutes at 4°C to separate the plasma from the hematocrit. Plasma aliquots were put on dry ice immediately for snap freezing and stored at -80°C subsequently for later downstream analysis.

DNA and RNA extraction

Plasma/Serum RNA/DNA Purification Mini Kit (Norgen Biotek, Thorold, ON, Canada) and Plasma/Serum cfc-DNA/cfc-RNA Advanced Fractionation Kit (Norgen Biotek, Thorold, ON, Canada) were used to extract cfDNA and cfRNA from mouse plasma per manufacturer's protocol. cfDNA and cfRNA were eluted in 20 µL of each corresponding buffer and were quantified using Qubit Fluorometric Quantitation (Thermo Fisher Scientific, Carlsbad, CA,

USA). The 2100 Bioanalyzer (Agilent Technologies, Palo Alto, CA, USA) was used to assess size distribution and concentration of cfDNA extracted from plasma samples. The total cfDNA concentration was determined with the software as the area under the peaks in the mononucleosomal size range (140–230 bp).

Reverse transcription was performed using High-Capacity cDNA Reverse Transcriptase Kit (Applied Biosystems, Foster City, CA, USA) to generate cDNA from plasma cfRNA per manufacturer's protocol. An initial preamplification reaction was run prior to ddPCR in the case of very low DNA/cDNA concentration. cfDNA were pre-amplified using Q5 hot start high-fidelity master mix (New England Biolabs, Beverly, MA, USA) with forward and reverse primer pair for EGFRvIII and TERT C228T (same primers used for ctDNA analysis) while cDNA was pre-amplified with EGFRvIII primer. Pre-amplification was performed with the Eppendorf Mastercycler: 98°C for 3 min; 12 cycles of 98°C for 30 s, 60°C for 1 min; a final extension of 72°C for 5 min, and 1 cycle at 4°C infinite. Preamplified products were directly used for further ddPCR reactions for ctDNA and mRNA quantification.

ctDNA and mRNA quantification

Custom sequence-specific primers and fluorescent probes were designed and synthesized for EGFRvIII and TERT C228T detection (Sigma Aldrich, St. Louis, MO, USA). The forward and reverse primer sequences for EGFRvIII were 5'-GGCTCTGGAGGAAAAGAAAGGTAATT-3' and 5'-CCTTCGCACTTCTTACACTTGC-3', respectively. The EGFRvIII probe sequence was 5'-CAGATCACGGCTCGTGCGTCCGAGCC-3' with the 6-carboxyfluorescein (6-FAM) fluorophore and the Black Hole Quencher 1 (BHQ1). The forward and reverse primer sequences for EGFRwt were 5'-TCTCAGCAACATGTCGATGGAC-3' and 5'-AGTTCTCCTCTCCTGCACC-3', respectively. The EGFRwt probe sequence was 5'-

CTCCCATTGGGACAGCTTGGATCACAC-3' with the hexachlorofluorescein (HEX) fluorophore. The forward and reverse primer sequences for TERT C228T mutant were 5'-CGTCCTGCCCCTTCACCTTC-3' and 5'-GCAGCGCTGCCTGAAACTCG-3', respectively. The TERT C228T mutant probe sequence was 5'-CGTCCCGACCCCTTCCGGGT-3' with 6-FAM and BHQ1. The forward and reverse primer sequences for TERT C228T wild type were the same as those for TERT C228T mutant. The TERT C228T wild type probe sequence was 5'-CGTCCCGACCCCTCCCGGGT-3' with HEX and BHQ1.

ddPCR reactions were conducted using Bio-Rad Q200X according to the manufacturer's instructions (Bio-Rad, Hercules, CA, USA). ddPCR reactions were prepared with 2× ddPCR Supermix for probes (no dUTP) (Bio-Rad, Hercules, CA, USA), 2 μL of target DNA product, of 0.1μM forward and reverse primers, and of 0.1μM probes. For TERT C228T reaction mix, 100μM 7-deaza-dGTP (New England Biolabs, Beverly, MA, USA) was added to improve PCR amplification of GC rich regions in the TERT promoter. The QX200 manual droplet generator (Bio-Rad, Hercules, CA, USA) was used to generate droplets. The PCR step was performed on a C1000 Touch Thermal Cycler (Bio-Rad, Hercules, CA, USA) by use of the following program: 1 cycle at 95°C for 10 min, 48 cycles at 95°C for 30 s and 60°C for 1 min, 1 cycle at 98°C for 10 min, and 1 cycle at 12°C for 30min, 1 cycle at 4°C infinite, all at a ramp rate of 2°C/s. All plasma samples were analyzed in technical duplicate or triplicate based on sample availability. Data were acquired on the QX200 droplet reader (Bio-Rad, Hercules, CA, USA) and analyzed using QuantaSoft Analysis Pro (Bio-Rad, Hercules, CA, USA). All results were manually reviewed for false positive and background noise droplets based on negative and positive control samples. Assays were considered positive if >3 droplets exceeded the threshold fluorescence[133,134]. Otherwise, the specimen was determined to have 0 copies/μl. EGFRvIII

and TERT C228T ctDNA and EGFRvIII mRNA concentrations (copies/µl plasma) were calculated by multiplying the concentration (provided by QuantaSoft) by elution volume, divided by the input plasma volume used during DNA extraction. A subject had a positive detection of the mutation when the levels of mutant ctDNA were >0 copies/µL. The EGFRvIII and TERT C228T sensitivities were calculated as the true positive rate, i.e., number of true positives divided by the sum of true positives and false negatives. The 95% confidence intervals were calculated according to the familiar, asymptotic Gaussian approximation $1.96\sqrt{p(1-p)/n}$, where p represents sensitivity and n was the sample size[135,136].

MRI analysis

MRI processing and analysis were consistent with Chapter 2.2 for the analysis of the U87-eGFP tumor.

Histological analysis

After blood collection, mice were transcardially perfused with 0.01 M phosphate-buffered saline (PBS) followed by 4% paraformaldehyde. Brains were harvested approximately 20 minutes after FUS and prepared for cryosectioning. The brains were horizontally sectioned to 15 µm slices and used for H&E staining to examine red blood cell extravasation and cellular injury or TUNEL staining to evaluate number of apoptotic cells. The brain slices were digitally acquired with the Axio Scan.Z1 Slide Scanner (Zeiss, Oberkochen, Germany). QuPath v0.2.0[108] was used to detect areas of microhemorrhage and TUNEL expression. The imaged slice for mouse histological analysis was segmented into the tumor region of interest (ROI) that includes the tumor mass and extends 0.5 mm into its periphery, which is consistent with the safety objectives from previous studies[74] and the potential damage caused by the external and lumen diameters of a biopsy needle[137,138]. The parenchyma ROI was defined as the whole imaged slice

without the tumor ROI. The tumor ROI for the histological analysis in mice included the tumor mass and a 3 mm margin[139].

After color deconvolution (hematoxylin vs. eosin), areas of microhemorrhage were detected using the positive-pixel count algorithm. The microhemorrhage density was calculated as the percentage of positive pixel area over the total stained area in the respective ROI. The number of apoptotic cells were detected using the positive cell detection algorithm. The TUNEL density was calculated as the percentage of positive cells over the total stained cells in the respective ROI.

Statistical analysis

Where appropriate, the data was analyzed with the paired t-test (Figure 6C, D, **Error! Reference source not found.**B, Figure 11G) or the unpaired two-sample Wilcoxon signed rank test (Figure 7A, B, Figure 8B, Figure 10A, B, Figure 13B, D). To analyze significance across multiple comparisons, the Kruskal-Wallis test and post hoc Dunn's test with Bonferroni correction was performed (Figure 12A, B). Statistical differences were considered significant (*) when $p < 0.05$, (**) when $p < 0.01$, (***) when $p < 0.001$, and (****) when $p < 0.0001$. Descriptive statistics is represented as mean ± SD.

2.3.2 Results

Sonobiopsy can increase detection sensitivity for small and large tumors

Contrast-enhanced T_1-weighted MR images were acquired approximately twice per week to monitor the tumor growth and segment the mice to small tumor and large tumor groups. The small tumor group had an average tumor volume of 5.70 ± 2.50 mm^3 approximately 5–7 days after intracranial implantation. The large tumor group had an average tumor volume of 25.63 ± 14.47 mm^3 approximately 10–12 days after intracranial implantation. In the small tumor group, FUS significantly increased ($p = 0.0053$) the CE volume by approximately 6-fold on average

(Figure 6C). In the large tumor group, FUS significantly increased ($p = 3.9\times10^{-7}$) the average CE volume by approximately 1.75-fold (Figure 6D).

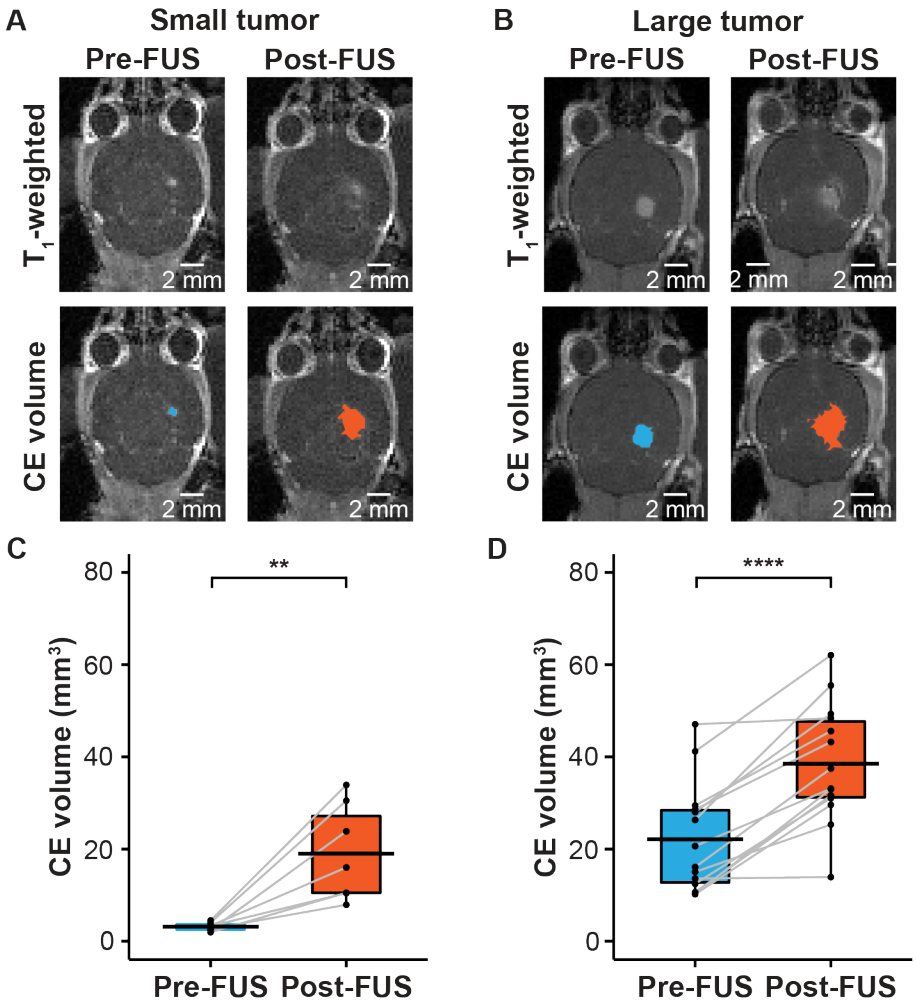

Figure 6. FUS successfully disrupted BBB in small and large tumor cases. Pre-FUS MRI scans show the tumor volume (blue area) and post-FUS MR images verify BBB disruption (orange area) for the small tumor group (A) and the large tumor group (B). (C) FUS significantly increased the CE volume ($p = 0.0053$; $^{**}p < 0.01$; paired t-test) from 3.17 ± 0.91 mm^3 to 19.01 ± 10.45 mm^3 for the small tumor group ($n = 7$). (D) FUS significantly increased the CE volume ($p = 3.9\times10^{-7}$; $^{****}p < 0.0001$; paired t-test) from 22.11 ± 11.77 mm^3 to 38.51 ± 12.87 mm^3 for the large tumor group ($n = 23$). Black bars indicate mean in C and D.

Blood LBx had low detection levels of EGFRvIII mRNA for small (0.14 ± 0.25 copies/µL) and large (4.47 ± 17.18 copies/µL) tumors (Figure 7A). These biomarker levels

corresponded to low detection sensitivities for small (TP: 0; FN: 14; sensitivity: 0.00%; FNR: 100.00%) and large (TP: 8; FN: 15; sensitivity: 34.78%; FNR: 65.22%) tumors (Figure 7B).

Sonobiopsy increased ($p = 0.29$) the plasma level of EGFRvIII mRNA to 0.45 ± 0.61 copies/μL for small tumors and significantly increase ($p = 0.0033$) the level to 41.59 ± 51.99 copies/μL for large tumors (Figure 7A). In addition, sonobiopsy detected significantly higher levels of EGFRvIII mRNA in large tumors compared with small tumors ($p = 0.047$). These biomarker levels did not improve the detection sensitivity for small tumors (TP: 0; FN: 7; sensitivity: 0.00%; FNR: 100.00%), but the detection sensitivity for large tumors increased (TP: 15; FN: 8; sensitivity: 65.22%; FNR: 64.78%) (Figure 7B). The sensitivity with 95% confidence interval is shown in Table 2. Sonobiopsy was the most effective in increasing plasma biomarker levels and improving the detection sensitivity for large tumors with an average tumor volume approximately 25 mm^3.

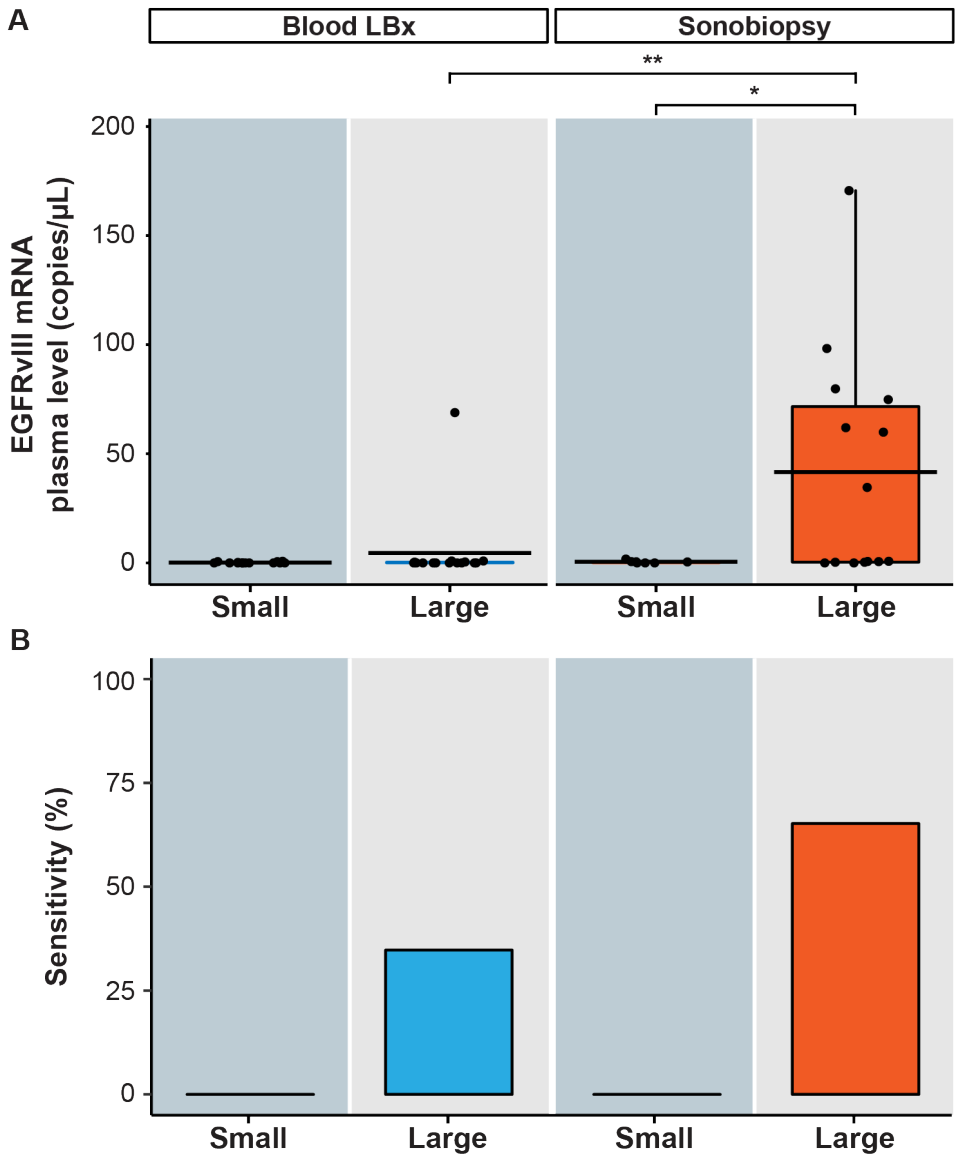

Figure 7. Sonobiopsy-induced release of biomarkers was more effective for larger tumors. (A) The level of EGFRvIII mRNA was nearly undetectable in plasma using conventional blood LBx in both the small tumor (n = 14; 0.14 ± 0.25 copies/μL) and large tumor groups (n = 23; 4.47 ± 17.18 copies/μL). With sonobiopsy, the plasma level of EGFRvIII mRNA increased to 0.45 ± 0.61 copies/μL (n = 7) in the small tumor group (p = 0.29; unpaired two-sample Wilcoxon signed rank test) and significantly increased to 41.59 ± 51.99 copies/μL (n = 23) in the large tumor group (p = 0.0033; $^{**}p < 0.01$; unpaired two-sample Wilcoxon signed-rank test). By leveraging sonobiopsy, the plasma level of EGFRvIII mRNA was significantly greater for large tumors compared with small tumors (p = 0.047; $^{*}p < 0.05$; unpaired two-sample Wilcoxon signed-rank test). (B) The sensitivity of blood LBx was 0.00% for small tumors and was 34.78% for large tumors. While sonobiopsy did not improve the sensitivity for small tumors (0.00%), the sensitivity for large tumors nearly doubled (65.22%). Black bars indicate mean in B.

Table 2. Sensitivities (±95% confidence interval) for different tumor sizes in mice.

	Blood LBx	Sonobiopsy
Tumor size	Sensitivity % (95% confidence interval)	Sensitivity % (95% confidence interval)
Small	0.00 ± 0.00	0.00 ± 0.00
Large	34.78 ± 19.46	65.22 ± 19.46

Sonobiopsy enhanced release of non-specific cell-free DNA (with single-point sonication)
The U87-EGFRvIII+ cell line that carry the TERT C228T mutation was used to compare the detection of EGFRvIII and TERT C228T mutations with sonobiopsy or conventional blood-based LBx (blood LBx). The mice with the large tumors were used to analyze the levels of cfDNA and ctDNA. The average tumor volumes for the blood LBx (n = 14) group and the sonobiopsy group (n = 14) were not significantly different ($p = 0.21$; unpaired t-test) at 29.15 ± 16.42 mm^3 and 22.11 ± 11.77 mm^3, respectively.

Terminal blood collection via cardiac puncture was performed 10 minutes after FUS sonication. Analysis of the plasma cell-free DNA (cfDNA) found that sonobiopsy enhanced the release of cfDNA compared to conventional blood LBx (Figure 8A). The plasma levels of mononucleosomal cfDNA, i.e., 140–230 base pairs (bp) increased approximately 2-fold with sonobiopsy ($p = 0.093$) (Figure 8B).

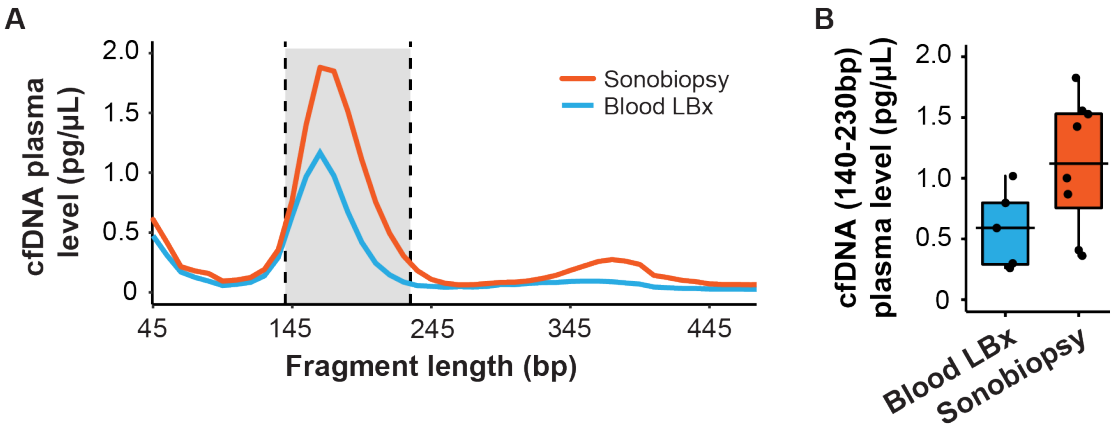

Figure 8. Fragmentation profile of sonobiopsy-released cfDNA. (A) The average size distributions of cfDNA fragment levels were evaluated in the blood collected after FUS for the sonobiopsy group (orange line, n = 8) and without FUS for the blood LBx group (blue line, n = 5). The plasma levels of mononucleosomal cfDNA fragments between 140 and 230 bp (gray dashed area) were quantified. (B) Sonobiopsy increased the cfDNA levels from 0.030 ± 0.016 pg/μL to 0.056 ± 0.027 pg/μL in the mononucleosomal size range (p = 0.09; unpaired two-sample Wilcoxon signed rank test).

Sonobiopsy enhanced release of circulating tumor DNA (with single-point sonication)
Custom ddPCR primers and probes for the detection of EGFRvIII and TERT C228T mutations were validated *in vitro* with cell lines that have known mutation statuses (Figure 9). The EGFRvIII ctDNA level in the sonobiopsy group (22.78 ± 39.96 copies/μL) was significantly greater (1,084-fold; $p = 0.012$) compared with the level in the blood LBx group (0.021 ± 0.078 copies/μL) (Figure 10A). The TERT C228T ctDNA level was not significantly different ($p = 0.46$) in the sonobiopsy group (0.25 ± 0.74 copies/μL) compared with the blood LBx group (0.064 ± 0.181 copies/μL) (Figure 10B).

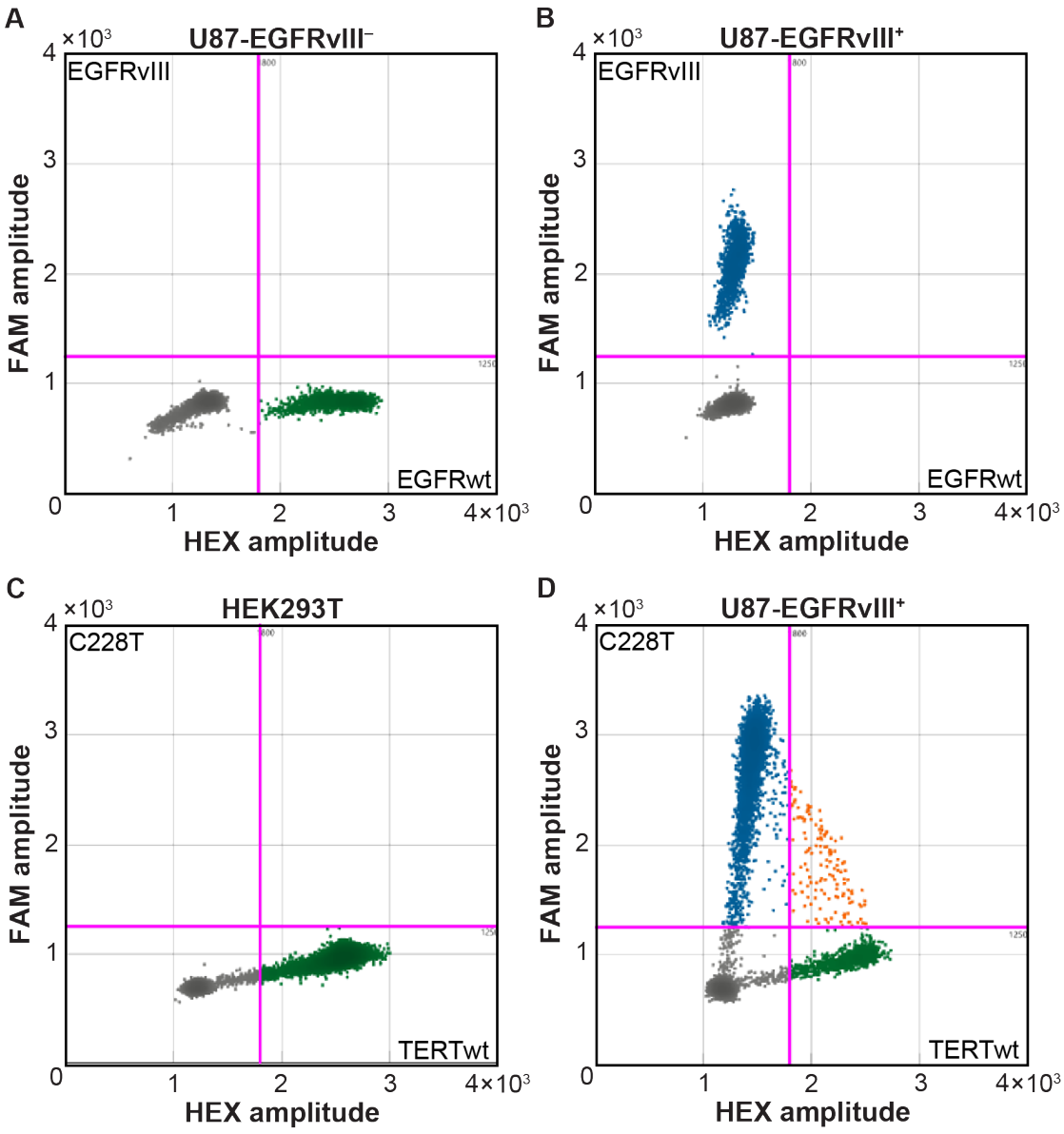

Figure 9. Validation of custom ddPCR primers and probes to detect EGFRvIII and TERT C228T. (A) While the wild type U87 cell line without EGFRvIII expression (U87-EGFRvIII⁻) had detectable copies of EGFRwt (green points), there were no detectable copies of EGFRvIII (blue points). (B) Meanwhile, the U87 cell line transfected with EGFRvIII overexpression (U87-EGFRvIII⁺) had positive detection of EGFRvIII. (C) While the human embryonic kidney cells (HEK293T) had detectable copies of TERTwt (green points), there were no detectable copies of TERT C228T (blue points). (D) ddPCR detected both TERT C228T and TERT wild type (TERTwt) in U87 cell line with known TERT C228T expression (U87-EGFRvIII⁺). The green color indicates droplets with positive expression of the genetic target along the horizontal axis, i.e., EGFRwt for A and B or TERTwt for C and D. The blue color indicates droplets with positive

expression of the genetic target along the vertical axis, i.e., EGFRvIII for A and B or TERT C228T for C and D. The orange color indicates droplets with positive expression of the genetic targets along the horizontal and vertical axes.

The diagnostic performance for detecting EGFRvIII ctDNA with blood LBx (number of true positives [TP]: 1; number of false negatives [FN]: 13; sensitivity: 7.14%; false negative rate [FNR]: 92.86%) was less sensitive than sonobiopsy (TP: 10; FN: 12; sensitivity: 45.45%; FNR: 54.55%) (Figure 10C). Similarly, blood LBx (TP: 3; FN: 18: sensitivity: 14.29%; FNR: 85.71%) was less sensitive in detecting TERT C228T ctDNA than sonobiopsy (TP: 4; FN: 12; sensitivity: 25%; FNR: 75%) (Figure 10C). The sensitivity with 95% confidence interval is shown in Table 3.

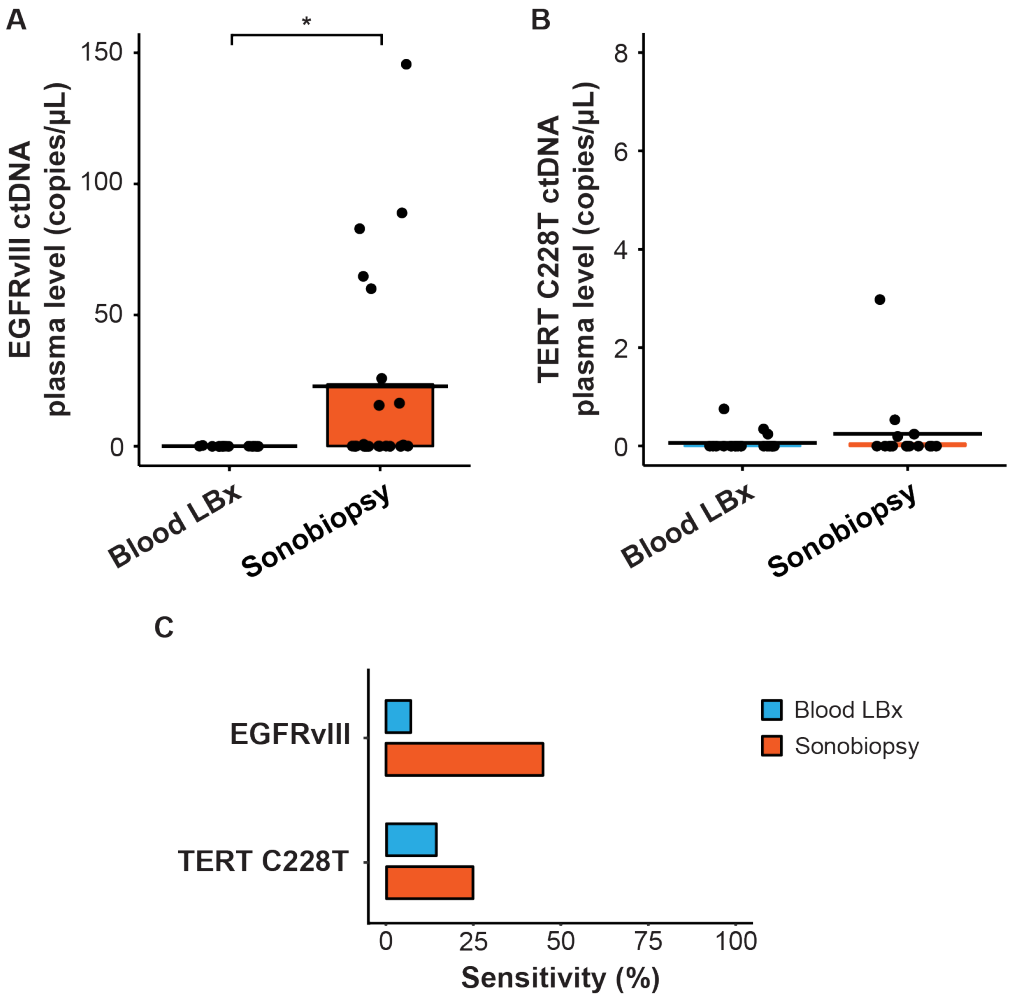

Figure 10. Sonobiopsy increased the detection sensitivity of EGFRvIII and TERT C228T mutations in mouse plasma by ddPCR. (A) The plasma level of EGFRvIII ctDNA in the sonobiopsy group (n = 22; 22.78 ± 39.96 copies/μL) was significantly greater (p = 0.012; $^{*}p < 0.05$; unpaired two-sample Wilcoxon signed rank test) compared with that in the blood LBx group (n = 14; 0.021 ± 0.078 copies/μL). (B) The plasma level of TERT C228T ctDNA in the sonobiopsy group (n = 16; 0.25 ± 0.74 copies/μL) was not significantly different (p = 0.46; unpaired two-sample Wilcoxon signed rank test) compared with that in the blood LBx group (n = 21; 0.064 ± 0.181 copies/μL). (C) With ddPCR, sonobiopsy is more sensitive than blood LBx with a detection rate of 45.45% for EGFRvIII and 25% for TERT C228T compared with 7.14% and 14.29% for blood LBx, respectively. Black bars indicate mean in A and B.

Large volume sonobiopsy improved detection sensitivity of circulating tumor DNA

In contrast to the single-point trajectory (Figure 11A), which was previously used for sonobiopsy in mice with large tumors, large volume sonobiopsy consisted of 3 points spaced 0.5 mm apart that were sonicated sequentially from anterior to posterior (Figure 11B). The total sonication duration and power at each point remained constant as if 3 single-point trajectories were performed. The average tumor volumes for the large volume sonobiopsy group (n = 13; 28.69 ± 13.37 mm^3) was not significantly different ($p = 0.34$; ANOVA with post hoc Bonferroni correction) than the tumor volumes for the blood LBx group (n = 14; 29.15 ± 16.42 mm^3) and the sonobiopsy group (n=14; 22.11 ± 11.77 mm^3). CE T_1-weighted MRI scans for single-point sonication (Figure 11C) and large volume sonication (Figure 11D) were acquired to assess tumor growth and evaluate FUS-induced BBB disruption. While the single-point sonobiopsy significantly increased the CE volume (Figure 11E), large volume sonobiopsy also significantly increased ($p = 6.3\times10^{-5}$) the average volume of tissue with enhanced BBB permeability by approximately 1.5-fold from 28.69 ± 13.37 mm^3 to 54.50 ± 17.38 mm^3 (Figure 11F).

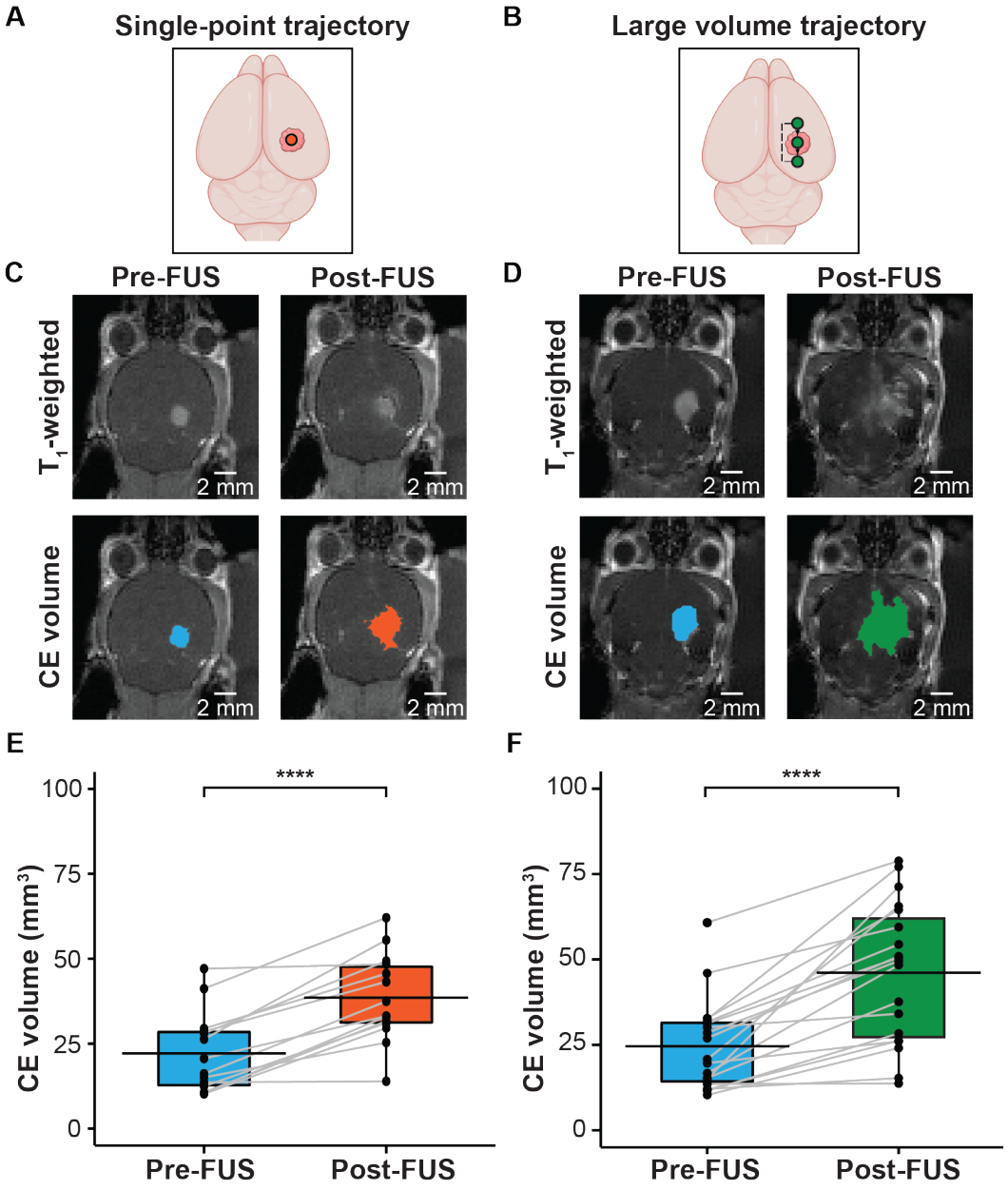

Figure 11. Single-point and large volume FUS sonication can achieve BBB disruption. (A) The single-point trajectory that was used for the previous experiments targeted the tumor center. (B) The proposed large volume trajectory was designed to sonicate the tumor center and the periphery to ensure maximal BBB disruption of the tumor volume. (C) The pre-FUS and post-FUS MR images shown previously for single-point sonobiopsy. (D) Pre-FUS and post-FUS MRI scans were acquired to assess BBB disruption (green area) using large volume sonobiopsy. (E) As previously shown, FUS significantly increased the CE volume ($p = 3.9\times10^{-6}$; $^{****}p < 0.0001$; paired t-test) from 22.11 ± 11.77 mm^3 to 38.51 ± 12.87 mm^3 ($n = 14$). (F) With the large volume trajectory, FUS significantly increased the CE volume ($p = 6.3\times10^{-5}$; $^{****}p < 0.0001$; paired t-

test) from 28.69 ± 13.37 mm^3 to 54.50 ± 17.38 mm^3 (n = 13). Black bars indicate mean in E and F.

The EGFRvIII ctDNA level in the large volume sonobiopsy group (19.06 ± 24.74 copies/µL) was significantly greater (p = 0.0056) compared with the level in the blood LBx group (0.021 ± 0.078 copies/µL) (Figure 12A). The TERT C228T ctDNA level in the large volume sonobiopsy group (0.64 ± 1.19 copies/µL) was significantly greater (p = 0.040) compared with the level in the blood LBx group (0.064 ± 0.181 copies/µL) (Figure 12B).

The diagnostic performance for detecting EGFRvIII ctDNA with blood LBx (number of true positives [TP]: 1; number of false negatives [FN]: 13; sensitivity: 7.14%; false negative rate [FNR]: 92.86%) was less sensitive than single-point sonobiopsy (TP: 10; FN: 12; sensitivity: 45.45%; FNR: 54.55%). However, large volume sonobiopsy was the most sensitive (TP: 11; FN: 6; sensitivity: 64.71%; FNR: 35.29%) (Figure 12C). Similarly, the diagnostic performance for detecting TERT C228T ctDNA was lowest with blood LBx (TP: 3; FN: 18: sensitivity: 14.29%; FNR: 85.71%), followed by single-point sonobiopsy (TP: 4; FN: 12; sensitivity: 25%; FNR: 75%), with large volume sonobiopsy as the most sensitive (TP: 11; FN: 13; sensitivity: 45.83%; FNR: 54.17%) (Figure 12C). The sensitivity with 95% confidence interval is shown in Table 3.

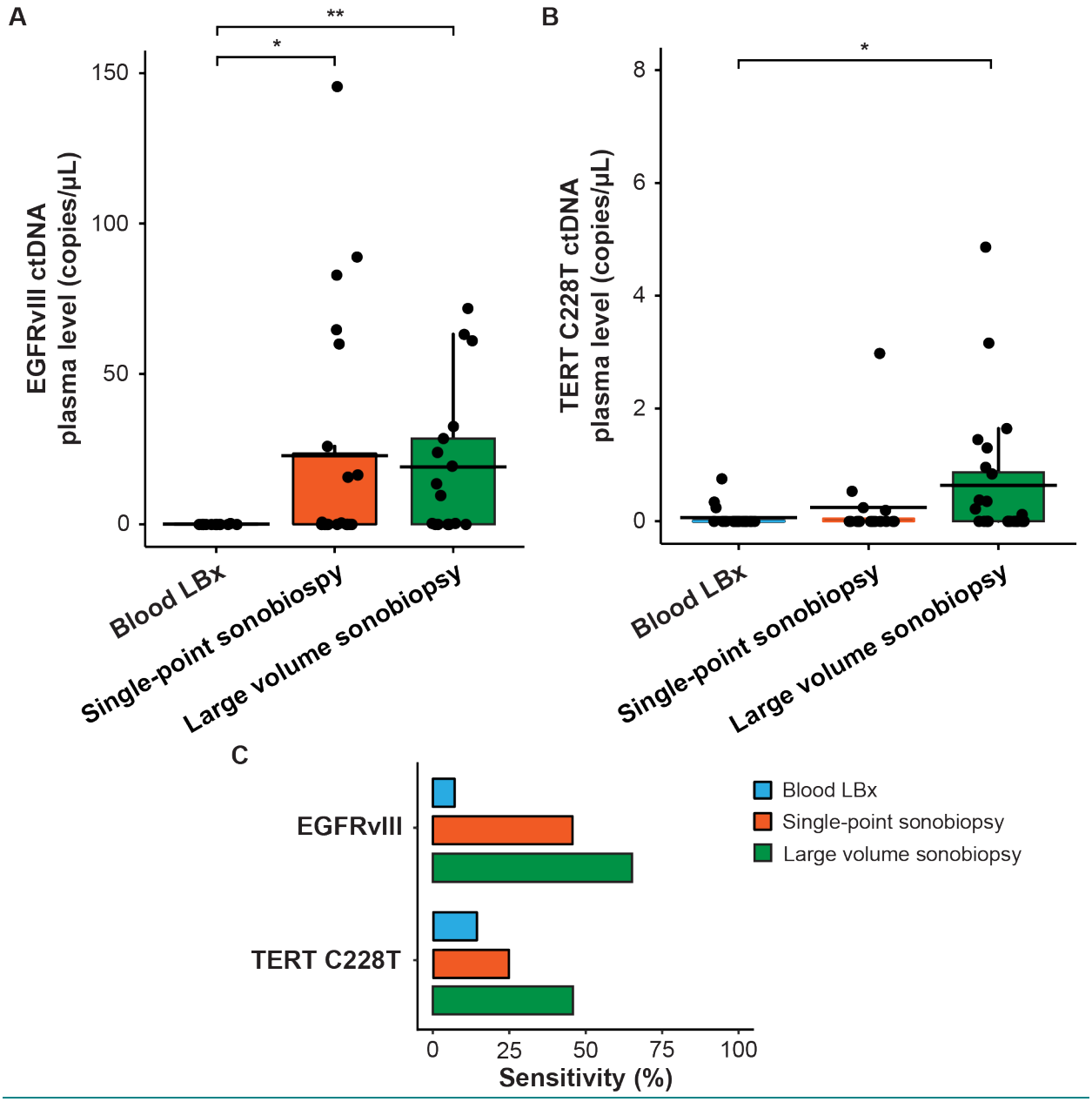

Figure 12. Large volume sonobiopsy was more effective to improve detection sensitivity. (A) Large volume sonobiopsy significantly increased ($p = 0.0056$; $^{**}p < 0.01$; Kruskal-Wallis multiple comparison test and post hoc Dunn's test with Bonferroni correction) the plasma level of EGFRvIII ctDNA (n = 17; 19.06 ± 24.74 copies/µL) compared with blood LBx, which was a more significant difference than the single-point sonobiopsy ($p = 0.012$; $^{*}p < 0.05$). (B) While single-point sonobiopsy did not significantly increase the plasma level of TERT C228T ctDNA, large volume sonobiopsy significantly increased ($p = 0.040$; Kruskal-Wallis multiple comparison test and post hoc Dunn's test with Bonferroni correction) the plasma level of TERT C228T ctDNA n = 24; 0.64 ± 1.19 copies/µL) compared with the blood LBx. (C) With ddPCR, large

volume sonobiopsy is more sensitive than blood LBx with a detection rate of 64.71% for EGFRvIII and 45.83% for TERT C228T compared with 7.14% and 14.29% for blood LBx, respectively. Black bars indicate mean in A and B.

Table 3. Sensitivities (±95% confidence interval) for different mutations and sonication trajectories in mice.

	Blood LBx	Single-point sonobiopsy	Large volume sonobiopsy
Mutation	Sensitivity % (95% confidence interval)	Sensitivity % (95% confidence interval)	Sensitivity % (95% confidence interval)
EGFRvIII	7.14 ± 13.49	45.45 ± 20.81	64.71 ± 22.72
TERT C228T	14.29 ± 14.97	25.00 ± 21.22	45.83 ± 19.93

Large volume sonobiopsy did not cause significant off-target damage

One safety concern with large volume sonobiopsy was the potential for tissue damage in the parenchyma. H&E staining was performed to quantify the extent of FUS-induced microhemorrhage and TUNEL staining was used to evaluate the number of apoptotic cells. Sonobiopsy led to a non-significant ($p = 0.18$) increase in detected microhemorrhage within the tumor region of interest (ROI) (Figure 13A,B). There was no significant off-target damage in the brain parenchyma ($p = 0.33$). Sonobiopsy also did not significantly change the TUNEL expression in the tumor ROI ($p = 0.73$) or the brain parenchyma ($p = 0.11$) (Figure 13C,D).

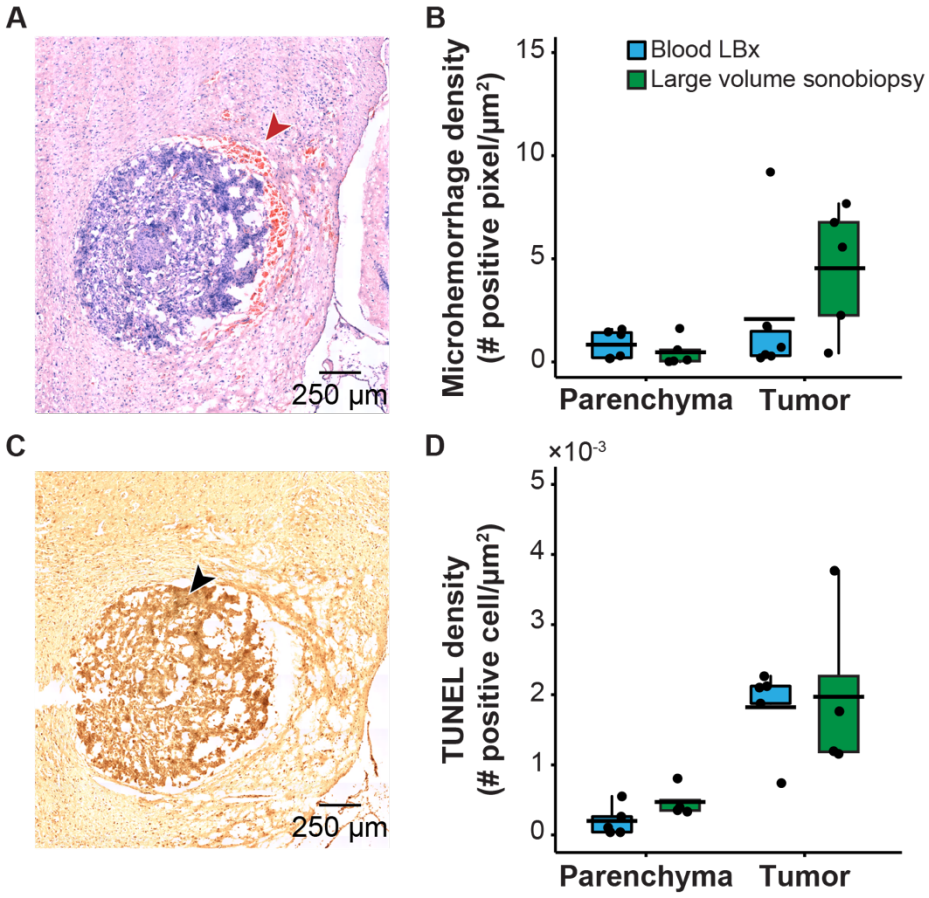

Figure 13. Large volume sonobiopsy did not cause significant acute damage. (A) Representative H&E staining for a subject treated with large volume sonobiopsy. The red arrow points to microhemorrhage in the tumor ROI. (B) The microhemorrhage density in the parenchyma after large volume sonobiopsy (n = 5; 0.47 ± 0.68 positive pixels/µm^2) was not significantly different compared with that after blood LBx (n = 5; 0.83 ± 0.69 positive pixels/µm^2; p = 0.33; unpaired two-sample Wilcoxon signed rank test). There was a nonsignificant increase in microhemorrhage occurrence in the tumor ROI after large volume sonobiopsy (n = 5; 4.54 ± 3.08 positive pixels/µm^2) compared with that after blood LBx (2.08 ± 3.54 positive pixels/µm^2; n = 5; p = 0.18; unpaired two-sample Wilcoxon signed rank test). (C) Representative TUNEL staining for a subject treated with large volume sonobiopsy depicts increased apoptotic signal in the tumor ROI. The black arrow points to an apoptotic cell. (D) There was no significant difference in TUNEL density for the parenchyma between blood LBx (n = 5; 0.20×10^{-3} ± 0.22×10^{-3} positive cells/µm^2) and large volume sonobiopsy (n = 5; 0.47×10^{-3} ± 0.22×10^{-3} positive cells/µm^2; p = 0.11; unpaired two-sample Wilcoxon signed rank test). There was no significant difference in TUNEL density for the tumor ROI between blood LBx (n = 5; 1.82×10^{-3} ± 0.62×10^{-3} positive cells/µm^2) and large volume sonobiopsy (n = 5; 1.97×10^{-3} ± 1.22×10^{-}

^{3} positive cells/μm^{2}; p = 0.73; unpaired two-sample Wilcoxon signed rank test). Black bars indicate mean in B and D.

2.3.3 Discussion

Sonobiopsy addresses the fundamental challenge of obtaining specimens for the sensitive diagnosis and molecular characterization of brain cancer. Sonobiopsy improved the plasma levels of EGFRvIII ctDNA by 920-fold and TERT C228T ctDNA by 10-fold. Furthermore, sonobiopsy increased the detection sensitivity for EGFRvIII by 57.57% and TERT C228T by 31.54%. The enhanced plasma levels and detection rate of EGFRvIII are striking compared to those of TERT C228T. This discrepancy may be attributed to the overexpression of the EGFRvIII mutation in the U87-EGFRvIII^{+} cell line. On the other hand, TERT C228T was only expressed on a single chromosome. As a result, the EGFRvIII biomarkers may experience a larger accumulation during tumor growth and greater release after FUS-mediated BBB disruption compared with TERT C228T biomarkers. By using two biomarkers to represent two different gene mutation expression levels, this study demonstrated the range of potential for sonobiopsy.

The mouse models, while well-characterized and common due to their ease of genetic manipulation, short breeding times, and evolutionary similarities, lack a gyrencephalic structure and other human-like features that are relevant for sonobiopsy, such as skull thickness, brain volume, and blood volume[140,141]. Therefore, the results from the mouse experiments in this study demonstrate the feasibility for improving the detection sensitivity of mutations in ctDNA, but this may not be clinically relevant. We will utilize a large animal model in Chapter 3 to establish the potential for clinical translation.

The integration of sonobiopsy with advanced blood analysis assays has the promise to provide minimally invasive, spatiotemporal-controlled, and sensitive diagnosis of brain cancer.

Compared to completely noninvasive technology for detecting circulating markers *in vivo*[142], sonobiopsy is minimally invasive because it requires venipuncture for intravenous delivery of microbubbles and blood collection. ddPCR is a targeted approach to rapidly detect specific known mutations with high sensitivity and high tissue concordance[25,143,144]. Thus, ddPCR was used in our study to detect ctDNA with *a priori* knowledge of the mutations expressed by the implanted GBM tumors. In the clinic, this information may not be known, e.g., if sonobiopsy is performed prior to surgical biopsy or if the tumor evolves over time. Thus, future studies should examine the molecular landscape independent of hotspot mutations with approaches such as whole genome sequencing, next-generation sequencing, or bisulfite sequencing.

We analyzed the correlations between biomarker release, contrast enhancement, and tissue damage. There was no strong correlation observed in the mouse experiment between microhemorrhage density and EGFRvIII ctDNA plasma level (n = 5, Pearson's correlation coefficient $r = 0.12$, $p = 0.72$), microhemorrhage density and change in CE volume (n = 5, $r = 0.025$, $p = 0.96$), or EGFRvIII ctDNA plasma level and change in CE volume (n = 17, $r = 0.13$, $p = 0.66$). The lack of a strong correlation suggests that FUS-induced biomarker release is a complex process that may be affected by many variables and/or a larger sample size is needed to detect these correlations.

2.3.4 Conclusion

This study demonstrated that the optimization of sonobiopsy parameters is crucial to both maximize biomarker release and minimize tissue damage. Blood collection time, FUS pressure, MB dose, and volumetric sonication were all critical variables to consider when designing sonobiopsy procedure. Though sonobiopsy had a similar detection sensitivity of mRNA as conventional blood LBx for small tumors, sonobiopsy improved the detection sensitivity for

large tumors. In addition, sonobiopsy increased the plasma level of cfDNA and ctDNA. Importantly, large volume sonobiopsy significantly improved the biomarker release and was more sensitive than single point sonobiopsy. Further, large volume sonobiopsy did not cause significant off-target damage. This work provides convincing evidence that supports the feasibility for sonobiopsy to enrich the blood with brain tumor-derived biomarkers for the sensitive detection of tumor mutations.

Chapter 3: Assess potential for clinical translation with large animal model

3.1 Abstract

The goal for this chapter was to develop a sonobiopsy system for large animals and evaluate the feasibility and safety of sonobiopsy in the normal brain tissue of a pig model. Increased BBB permeability was confirmed by the significant increase in CE volume ($p = 0.0156$) and in K^{trans} ($p = 0.0053$) when comparing the FUS-sonicated brain area with the contralateral non-sonicated area. Meanwhile, there was a significant increase in the blood concentrations of glial fibrillary acidic protein (GFAP, $p = 0.0074$) and myelin basic protein (MBP, $p = 0.0039$) after FUS sonication as compared with before FUS. There was no detectable tissue damage by T_2^*-weighted MRI and histological analysis. Findings from this study suggest that sonobiopsy is a promising technique for noninvasive and localized diagnosis of the molecular profiles of brain diseases with the potential to translate to the clinic.

3.2 Evaluate feasibility for sonobiopsy in nontumor pig

To demonstrate the clinical translation potential of sonobiopsy, large animal models are required because a small animal model cannot represent the technical challenge of FUS delivery through the thick human skull and biomarkers released by sonobiopsy will be far more diluted in humans and large animals than in mice. In the current study, we used pigs as the large animal model for demonstrating the feasibility of sonobiopsy. The pig model was selected because its similarity in blood volume/body weight, skull thickness, and brain morphology to humans[145–147] and it has fewer ethical concerns compared with the primate model.

As healthy pigs without tumors were used, we could not evaluate the release of tumor-specific biomarkers. Instead, we selected brain-specific biomarkers as a proof of concept

to demonstrate the feasibility and sensitivity of sonobiopsy. Specifically, glial fibrillary acidic protein (GFAP) and myelin basic protein (MBP) were selected to represent brain-specific biomarkers. These two biomarkers were selected for two reasons: they have been used as brain-specific biomarkers[148,149], and protein biomarkers can be detected in the plasma using well-established enzyme-linked immunosorbent assays (ELISA). In particular, GFAP is an important prognostic biomarker for brain diseases because its levels are associated with high-grade glioma volume and short progression free survival[150–152]. MBP is a diagnostic marker for brain damage and its evaluation can characterize severity and stage of disease[153,154]. In addition, expression of the MBP gene may be a useful molecular marker to subtype gliomas[155].

3.2.1 Methods

Animal preparation

All animal procedures were reviewed and approved by the Institutional Animal Care and Use Committee at Washington University in St. Louis in accordance with the Guide for the Care and Use of Laboratory Animals and the Animal Welfare Act. A total of 16 pigs (age: 3–4 weeks old; sex: male) were used in this study. These pigs were divided into two groups. The first group consisted of 8 pigs that were used to optimize the design of a customized MRI-guided FUS (MRgFUS) system for BBB opening in pigs and establish the standard operation procedure (SOP) for the FUS sonication of the pig brain. The second group consisted of 8 pigs that were used to evaluate the sonobiopsy technique using the optimized MRgFUS system and the established SOP. This Methods section describes the established SOP.

Pigs were sedated with an intramuscular injection of ketamine (2 mg/kg), xylazine (2 mg/kg) and telazol (4 mg/kg), intubated, and maintained under general anesthesia using diluted isoflurane and positive pressure ventilation. The hair on the pig head was removed using depilatory cream (Nair, Church & Dwight Co., Princeton, NJ) to ensure optimal acoustic

coupling. A catheter was placed in the ear vein for microbubble and MRI contrast agent injections. A fiber-optic pulse oximeter (Nonin 7500FO, Plymouth, MN) was used to monitor the blood oxygen level and pulse rate during the procedure. The animal body temperature was monitored and maintained with heated blankets.

Customized sonobiopsy device

An MRgFUS device was developed for the BBB opening in pigs. The major hardware components of the MRgFUS system are shown in Figure 14. The FUS system was developed by modifying a commercial MRI-compatible FUS system (Image Guided Therapy, Pessac, France) that was originally designed for small animal applications by replacing the FUS transducer and changing the design of the animal support. The FUS transducer (Imasonics, Voray sur l'Ognon, France) used for the pig study was a 15-element annular array with a center frequency of 650 kHz, an aperture of 6.5 cm, and a radius of curvature of 6.5 cm. The transducer was spherically shaped with a hole in the center for integration with a single-element transducer (center frequency of 650 kHz and a −6 dB bandwidth of 260 kHz) for passive cavitation detection (PCD). The FUS transducer was driven by an RF generator (Image Guided Therapy, Pessac, France). The annular array design allowed the FUS transducer to electronically steer the focus in the axial direction of the transducer (Z-axis). The transducer was connected to an MRI-compatible piezoelectric motor, allowing the position of the transducer to be mechanically adjusted (Figure 14A). The transducer was connected to a water balloon filled with degassed water and coupled to the pig head through a water chamber. The pig's head was supported and stabilized by a bite bar and two side-supports. We designed and manufactured the MRI-compatible frame (Figure 14A) with the help from the staff of the Washington University Instrument Machine Shop, which combines all components on a single platform, which

simplified the integration of the FUS system with the clinical MRI scanner (Ingenia 1.5 T, Philips Medical Systems, Inc., Cleveland, OH). A loop coil (dStream Flex L coil, Philips Medical Systems, Inc., Cleveland, OH) was placed on top of the FUS transducer for MR imaging (Figure 14B). The FUS transducer was calibrated using a needle hydrophone in a water tank with a piece of pig skull placed in front of the FUS transducer. The pressure levels reported in this study were based on these hydrophone measurements.

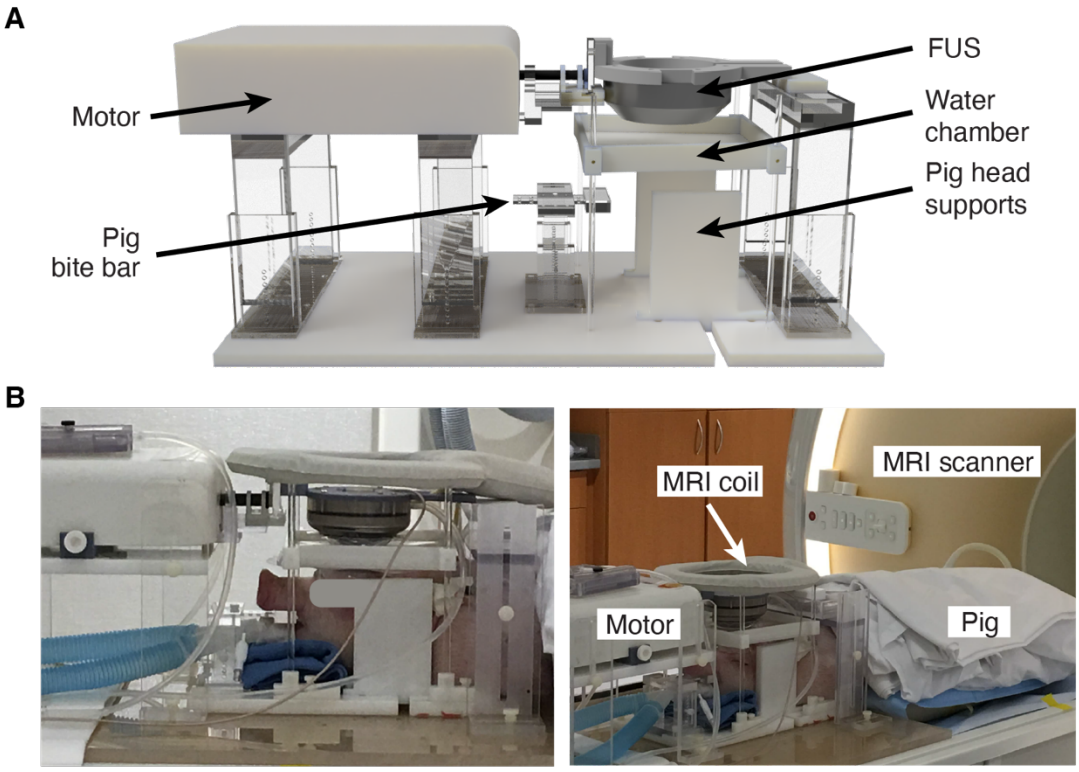

Figure 14. Customized MRI-guided FUS device for sonobiopsy in pigs. (A) 3D rendering of the FUS system. An MRI-compatible motor moved the FUS transducer to target a specific brain area. The pig head was fixed and stabilized by a bite bar and two side-supports. The transducer was coupled with the pig head through a water chamber. (B) View of the pig head along with the FUS transducer, motor, and MRI coil positioned on the MRI bed in the clinical MRI scanner.

Workflow for sonobiopsy

The overall workflow for sonobiopsy is summarized in Figure 15. It consists of seven steps: treatment planning, quality assurance, FUS sonication, sonication monitoring, outcome

assessment, safety evaluation, and blood sample analysis. Details of these steps are described below.

First, treatment planning began with a T_2-weighted MRI scan to image the pig head along with the FUS transducer (repetition time (TR): 1300 ms; echo time (TE): 130 ms; slice thickness: 1.2 mm; in-plane resolution: 0.58×0.58 mm^2; matrix size: 448×448; flip angle: 90°). The MRIs were imported to a software program (ThermoGuide, Image Guided Therapy, Pessac, France) to locate the geometrical focus of the transducer using 3-point triangulation. A specific brain location was targeted using a combination of mechanical movements by the MRI-compatible motor in 2D and electronic beam steering along the FUS axis.

Second, quality assurance was performed because one key challenge in transcranial FUS energy delivery is ensuring sufficient acoustic coupling between the transducer and the animal skin. A T_2^*-weighted scan was obtained to visualize the presence of air bubbles in the acoustic coupling media (TR/TE: 710/23 ms; slice thickness: 2.5 mm; in-plane resolution: 0.98×0.98 mm^2; matrix size: 224×224; flip angle 18°). Susceptibility artifacts associated with T_2^*-weighted scans highlight the presence of air bubbles by amplifying the size of local magnetic field inhomogeneities, such as the air-liquid interface of bubbles in the coupling media. If air bubbles were detected, as shown in the representative image (Figure 14), the preparation procedure was repeated until no bubbles were detected.

Third, FUS sonication was performed while real-time PCD was used to further verify sufficient acoustic coupling. If broadband emissions were present in the PCD when the FUS was turned on without microbubble injection, the most likely cause was due to air bubbles trapped in the coupling media that the T_2^*-weighted MRI scan was not able to detect. The experimental preparation procedure was repeated until there were no broadband emissions in the PCD. A T_1-

weighted MRI scan was acquired as a pre-treatment baseline for BBB permeability quantification (TR/TE: 5/2 ms; slice thickness: 1.5 mm; in-plane resolution: 0.68×0.68 mm^2; matrix size: 320×320; flip angle 10°). Then, FUS and PCD were turned on. The FUS parameters were: center frequency (f_0): 0.65 MHz; pressure: 1.5 MPa; pulse repetition frequency: 1 Hz; pulse duration: 10 ms; treatment duration: 3 min. Fifteen seconds after FUS sonication began, perflutren lipid-shelled microbubbles (Definity, Lantheus Medical Imaging, North Billerica, MA) were administered intravenously with a dose of 0.2 mL/kg body weight and followed with a 3 mL saline flush. The dose of microbubbles (MB) was increased to 5× the recommended clinical dose to increase the harmonic emission while maintaining safe sonication[156].

Fourth, the PCD signal was acquired for 15 seconds before microbubble injection was used as the baseline for quantifying the signals acquired after microbubble injection. Referencing the method to calculate cavitation levels used by our previous publication[157], a custom MATLAB script was written to process the acquired PCD data to evaluate the stable cavitation (SC) and inertial cavitation (IC) levels. Briefly, the stable and inertial cavitation levels were calculated as the root-mean-squared amplitudes of subharmonic ($f_0/2 \pm 0.15$ MHz) and broadband (0.3–2 MHz after removing $f_0/2 \pm 0.15$ MHz and $nf_0 \pm 0.15$ MHz where n = 1,2,3) signals, respectively. While the SC is a proxy of FUS-induced BBB opening, IC should generally be avoided because it may be associated with the presence of vessel damage.

Fifth, dynamic contrast-enhanced MRI (DCE-MRI) was performed to evaluate the dynamic extravasation of the MRI contrast agent, gadobenate dimeglumin (Gd-BOPTA; MultiHance, Bracco Diagnostics Inc., Monroe Township, NJ), from the blood circulation into brain tissue. Since Gd-BOPTA is too large to cross an intact BBB, the hyper-enhancement of

signal in the T_1-weighted images would indicate a successful BBB opening. A variable flip angle method was used to generate T_1 maps (TR/TE: 4.8/1.7 ms; slice thickness: 3 mm; in-plane resolution: 0.74×0.74 mm^2; matrix size: 336×336; flip angle: 25°, 20°, 15°, 10°, 5°). One minute after starting the DCE-MRI scan, Gd-BOPTA was intravenously injected at a dose of 0.2 mL/kg and a rate of 2 mL/s. The DCE-MRI imaging sequence (TR/TE: 4.8/1.7 ms; slice thickness: 3 mm; in-plane resolution: 0.74×0.74 mm^2; matrix size: 336×336; flip angle: 25°; temporal resolution: 7.5 s) monitored the extravasation of Gd-BOPTA over 10 minutes. An open-source MATLAB software package, ROCKETSHIP[158], was used to estimate K^{trans}, which is the influx rate constant for Gd-BOPTA to transfer from the blood to the tissue extravascular extracellular space and has been commonly used as an index of BBB permeability. The analysis of DCE-MRI started by converting the signal intensity data to concentration curves using T_1 maps. Second, the reference region for the arterial input function was selected. Third, the extended Tofts model[159–161] was fit to the data. The estimated K^{trans} values were averaged within a 5 voxel × 5 voxel region of interest at the FUS-targeted brain region (FUS^+) and the contralateral non-treated region (FUS^-).

Following the DCE-MRI sequence, a T_1-weighted MRI scan was acquired (with the same parameters as the pre-treatment T_1-weighted sequence) to further assess the BBB permeability. The outcome of FUS-induced BBB opening was evaluated by comparing the T_1-weighted images of pre- and post-FUS using a custom MATLAB script. The analysis started by defining an elliptical ROI (major axis: 19 mm; minor axis: 8 mm) in the FUS^+ and FUS^-. The ventricles were avoided in both ROIs because the hyperintensity of Gd-BOPTA in the ventricles would confound the calculation of hyper-enhancement in the tissue due to BBB disruption. Next, a voxel in the ROI was considered to contain an open BBB if the voxel intensity within the

FUS^+ ROI was greater than 3× standard deviations above the mean intensity within the FUS^- ROI. Then, the volume of BBB opening was estimated by calculating the sum of enhanced voxels for each image slice. Additionally, the contrast-enhanced T_1-weighted scan was overlaid with the planned transducer focus to guide the qualitative assessment of BBB opening and quantify the spatial offset between the planned and actual BBB opening.

Sixth, safety assessment was evaluated with a T_2^*-weighted MRI scan (with the same parameters as the pre-treatment T_2^*-weighted sequence) to detect FUS-induced hemorrhages approximately 1 hour after sonication. Hemorrhages would appear as hypointensity spots on the T_2^*-weighed images because the local magnetic field is distorted and signal is lost due to the distribution of methemoglobin[162].

Lastly, blood was collected before and after FUS sonication to quantify the concentration of brain-specific biomarkers in the blood using enzyme-linked immunosorbent assays (ELISA). Because normal pigs were used, representative brain-specific biomarkers, GFAP and MBP, were selected for the blood analysis using the appropriate ELISA assay (Cusabio Biotech, Wuhan, China) and standard protocol provided by the manufacturer.

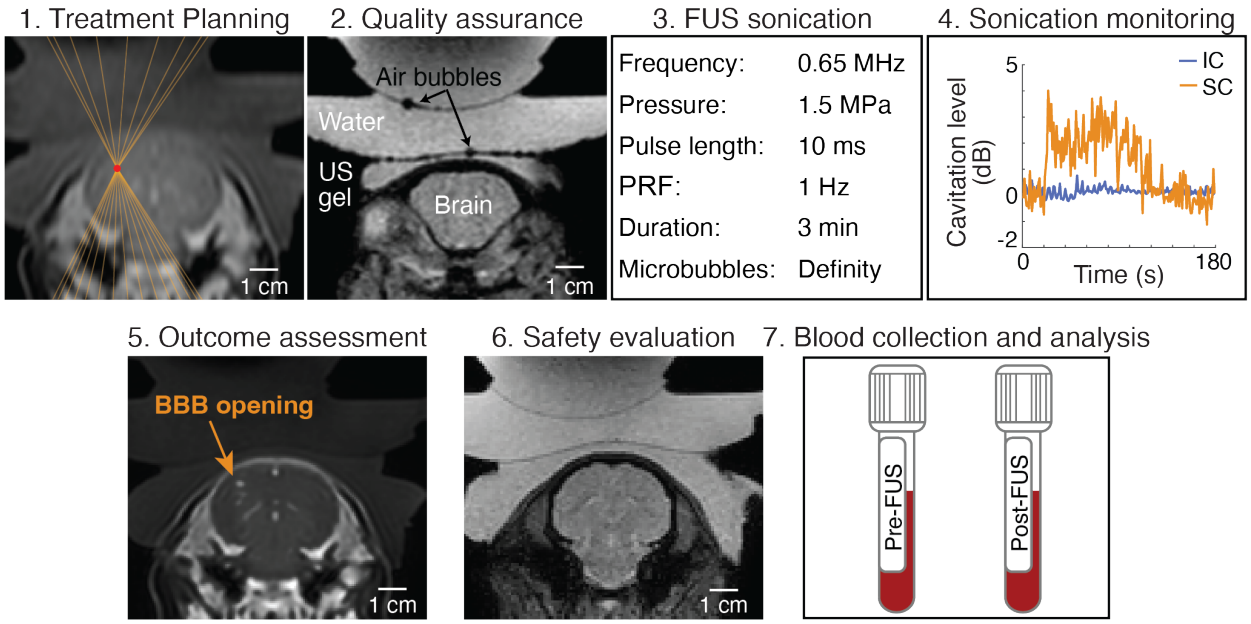

Figure 15. Workflow for sonobiopsy in pigs. The procedure started with treatment planning where the geometrical focus of the FUS transducer was aligned at the targeted brain location based on anatomic images acquired by T_1-weighted and T_2-weighted MRIs. Next, a T_2^*-weighted image, with the susceptibility artifact, was acquired to check whether the acoustic coupling media had air bubbles. If air bubbles were detected, as shown in the representative image, the preparation procedure was repeated until no bubbles were detected. FUS treatment began while monitoring cavitation activity with a PCD sensor. After treatment, contrast-enhanced T_1-weighted imaging was performed to assess BBB opening via MRI contrast agent extravasation. Additionally, T_2^*-weighted imaging was used to detect hemorrhages. Blood samples were collected pre-FUS and post-FUS for the analysis of brain-specific biomarkers

Histological analysis

After the sonobiopsy treatment was completed, the pigs were euthanized via sodium pentobarbital overdose (150 mg/kg intravenously) and the brain was collected approximately 60 minutes after FUS. After the brain was fixed for 1 week in 10% formalin, the whole brain was placed in a 3D-printed brain slicing matrix to cut the brain into 3-mm thick slabs around the FUS treatment area. A gross examination of the target slice would determine the presence of FUS-induced macroscopic damage at the treatment site. The 3-mm thick slabs were embedded in paraffin and cut into 7 µm thin slices for hematoxylin and eosin (H&E) staining to examine red blood cell extravasation and cellular injury. The whole-brain horizontal slices were imaged on

the Axio Scan.Z1 Slide Scanner (Zeiss, Oberkochen, Germany). A pathologist examined the stained slices and verified the results.

Statistical analysis

Where appropriate, the data was analyzed with the Wilcoxon matched-pairs signed-rank test (Figure 16B) or the paired t-test (Figure 16C, Figure 17, Figure 19A). Statistical differences were considered significant (*) when $p < 0.05$, (**) when $p < 0.01$, (***) when $p < 0.001$, and (****) when $p < 0.0001$. Descriptive statistics are represented as mean ± SD.

3.2.2 Results

Sonobiopsy successfully disrupted BBB

Successful BBB opening evidenced by contrast enhancement following FUS was achieved in 7 out of 8 pigs. One pig did not show obvious BBB opening, which could be attributed to the relatively large size of this pig (12.5 kg) compared to the other 7 pigs (8.16 ± 1.96 kg), leading to underestimated skull attenuation. Results obtained from the 7 pigs are presented in the following sections. Pharmacokinetic analysis of K^{trans} was performed on the last 4 pigs because the DCE-MRI sequence was not properly set up for the first 3 subjects. Figure 16A presents representative contrast-enhanced MRIs that show successful BBB disruption at the targeted brain location. The targeting accuracy as measured by the spatial offset between the target location and the actual BBB opening site was −1.9 ± 1.8 mm in the left-right direction (X), −0.4 ± 1.4 mm in head-foot direction (Y), and 5.3 ± 4.2 mm in the anterior-posterior direction (Z). The quantified BBB opening volume in the treated FUS + area (1.21 ± 1.84 cm^3) was significantly greater ($p = 0.0156$) than the BBB opening volume (0.013 ± 0.018 cm^3) in the contralateral FUS^- site (Figure 16B). The BBB permeability, quantified by K^{trans}, of the targeted brain site ($9.9 \times 10^{-3} \pm 3.9 \times 10^{-3}$ min^{-1}) was significantly greater ($p = 0.0053$) than that ($1.4 \times 10^{-3} \pm 0.8 \times 10^{-3}$ min^{-1}) of the contralateral side (Figure 16C).

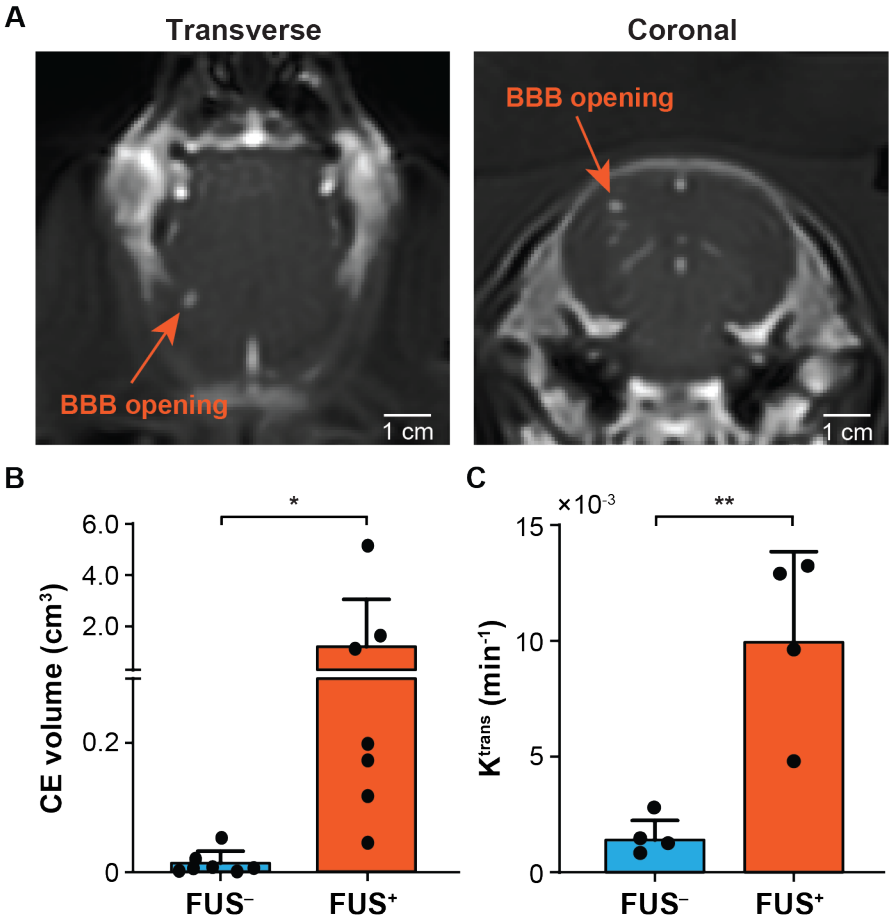

Figure 16. Customized sonobiopsy device induced successful BBB disruption in pigs. (A) Transverse and coronal T_1-weighted MRIs of a pig show successful BBB opening as indicated by the MRI contrast agent extravasation at the FUS-targeted site. (B) Significant increase in CE volume ($n = 7$; $p = 0.0156$; $^{*}p < 0.05$; Wilcoxon matched-pairs signed-rank test) at FUS-targeted brain region (FUS^{+}) and the contralateral non-treated region (FUS^{-}). Each circular point represents the result obtained from each pig. (C) Significant increase in K^{trans} values ($n = 4$; $p = 0.0053$; $^{**}p < 0.01$; paired t-test) in the FUS^{+} area compared with the FUS^{-} site. K^{trans} estimation was performed for the last 4 pigs.

Sonobiopsy enhanced the release of brain-specific biomarkers

FUS significantly enhanced the plasma concentration of the two brain-specific biomarkers, GFAP and MBP (Figure 17). The GFAP concentration significantly increased ($p = 0.0074$) from 0.156 ± 0.068 ng/mL in pre-FUS blood samples to 0.353 ± 0.149 ng/mL in post-FUS blood

samples. The MBP concentration in blood significantly increased ($p = 0.0039$) from 0.091 ± 0.034 ng/mL to 0.364 ± 0.159 ng/mL.

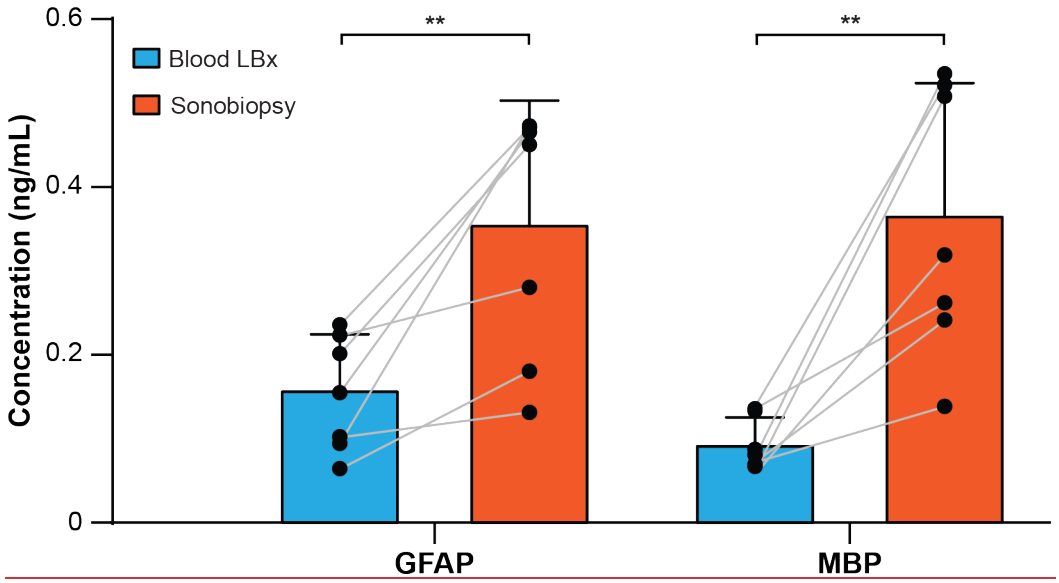

Figure 17. Sonobiopsy enhanced the release of brain-specific biomarkers, GFAP and MBP. The blood concentration of GFAP significantly increased post-FUS compared with pre-FUS ($n = 7$; $p = 0.0074$; $^{**}p < 0.01$; paired t-test). The concentration of MBP was significantly greater post-FUS compared with pre-FUS ($n = 7$; $p = 0.0039$; $^{**}p < 0.01$; paired t-test).

Sonobiopsy did not cause detectable tissue damage

MRI, FUS cavitation monitoring, gross pathological assessment, and histological analysis did not detect any tissue damage. Representative images display no sign of hemorrhage in the treated site compared with the contralateral area (Figure 18A). There was no significant change ($p = 0.50$) in the hypointensity volume between the pre-FUS T_2^*-weighted image (6.75 ± 5.50 mm^3) and the post-FUS T_2^*-weighted image (11.09 ± 15.40 mm^3) (Figure 18B). The lack of a significant IC increase post-MB compared to pre-MB ($p = 0.30$), while the SC significantly increased ($p = 0.0016$), suggests FUS did not induce violent MB activity that would lead to tissue damage (Figure 19A). There were no macroscopic signs of bleeding or tissue damage on this representative brain surface or at the treatment site based on gross pathology (Figure 19B).

H&E staining of the target slices from a second representative subject did not find tissue damage or hemorrhage at the FUS-treated site (Figure 19C).

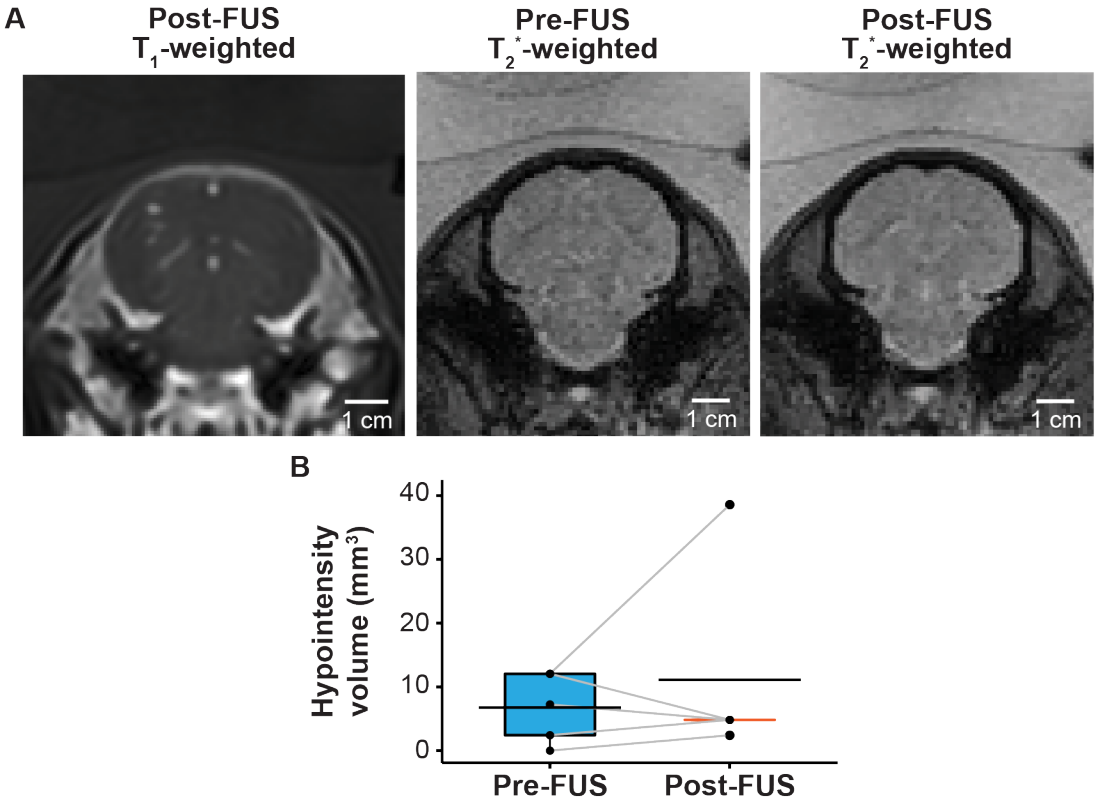

Figure 18. Sonobiopsy did not cause tissue damage detectable by MRI. (A) Representative MR images show localized BBB opening in T_1-weighted images and lack of signal change in T_2^*-weighted images after FUS sonication. (B) There was no significant increase in hypointensity volume after FUS sonication (n = 5; p = 0.50; paired t-test). Black bars indicate mean in B.

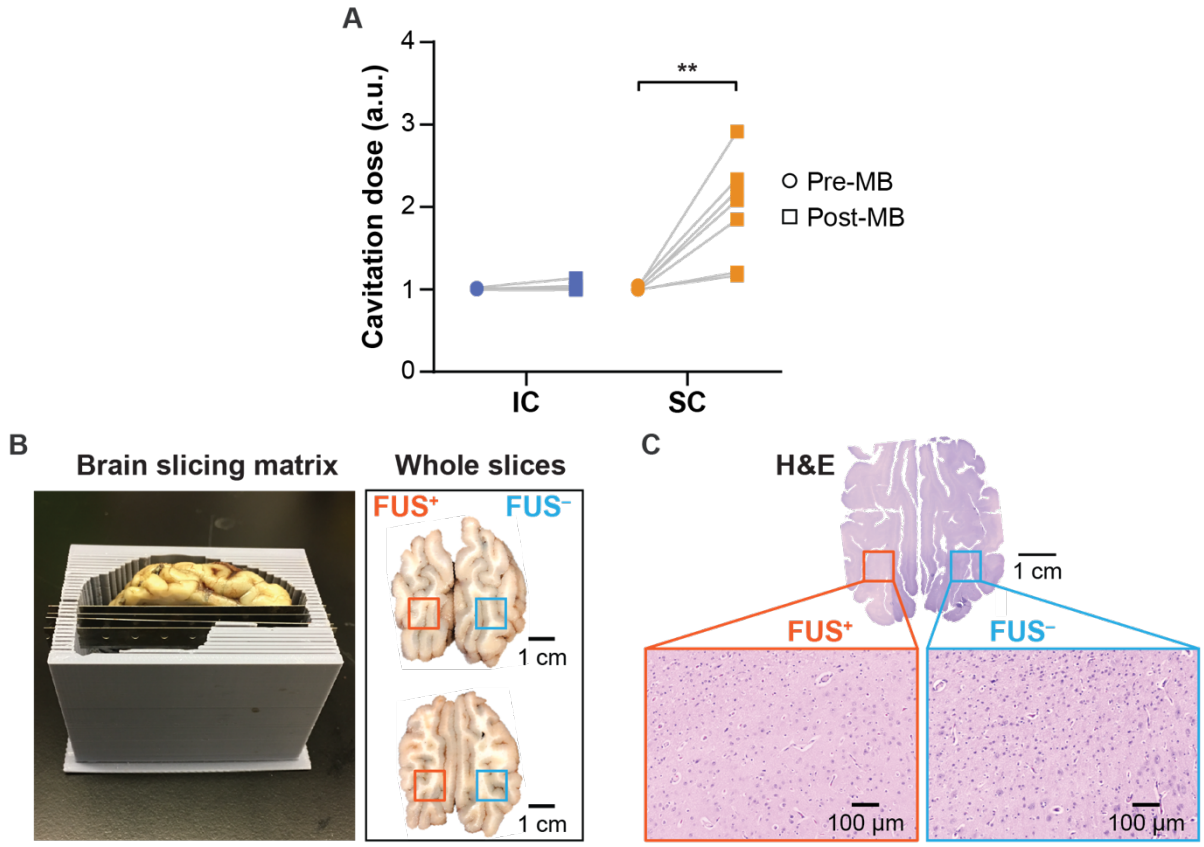

Figure 19. Sonobiopsy did not cause tissue damage detectable by cavitation or histological analysis. (A) Calculated cavitation levels for each of the 7 pigs found no significant increase of IC ($p = 0.30$; paired t-test) after microbubble injection (post-MB) compared with before microbubble injection (pre-MB). There was a significant increase in SC after microbubble injection ($p = 0.0016$; $^{**}p < 0.01$; paired t-test). (B) The 3D-printed brain slicing matrix was used to cut the brain into 3-mm thick slabs around the FUS treatment area. The gross pathological examinations did not find visible signs of tissue damage. The dark spots visible in the upper-right area of the whole brain slices were from uneven slicing where the lateral ventricle (black) was becoming visible on the right hemisphere but not visible on the left hemisphere. (C) H&E staining of the whole brain slices with microscopic views at FUS^+ and FUS^- sites did not suggest cellular damage.

3.2.3 Discussion

Ever since FUS was introduced for brain applications in the 1940s, it has been used as a therapeutic tool[163,164]. Recently, FUS has been established as a promising tool for brain drug delivery by disrupting the BBB to enable the transfer of drugs from the blood circulation to the brain. The current study demonstrated the feasibility and safety of sonobiopsy to enhance the

release of brain-specific biomarkers to the blood circulation in a porcine model for the diagnosis of brain diseases, suggesting that FUS is a promising theranostic tool for not only brain drug delivery but also brain disease diagnosis.

The noninvasive nature of the proposed sonobiopsy technique is especially advantageous over conventional neurosurgical tissue biopsies. Sonobiopsy is proposed to complement tissue biopsies instead of replacing them, by enabling repeated longitudinal sampling to monitor treatment response, which is often impossible to perform by tissue biopsies for brain tumor patients. It may also provide complementary information in situations where assessment based on neuroimaging alone remains challenging, for example, to differentiate tumor pseudoprogression induced by treatment from the true tumor progression and recurrence as the treatment often interferes with tumor imaging properties[165]. Sonobiopsy has the potential to radically advance the diagnosis, monitoring, and understanding of brain disease by precisely, rapidly, and safely identifying molecular signatures of brain diseases. Further, the technique presents a unique advantage in the assessment of spatially heterogeneous tumors. FUS can precisely target different locations of the tumor over time, thereby releasing biomarkers in a spatially-localized, temporally-resolved manner.

The current study suggests that the “two-way transfer” hypothesis, first proposed using mouse GBM models, is also valid in a large animal model. The customized sonobiopsy device achieved successful BBB opening in the pig model as verified with the detection of MRI contrast agent extravasation from the blood circulation to the brain tissue and the significant increase in BBB permeability as measured by K^{trans}. Meanwhile, the enhanced release of two brain-specific biomarkers from the brain to the blood circulation was confirmed by comparing the concentration of these biomarkers in the blood post-FUS with pre-FUS via ELISA

quantification. The enhanced biomarker release was achieved without causing detectable brain tissue damage.

The study is not without its limitations. First, this study investigated brain-specific biomarkers, not brain tumor-specific biomarkers. We verified that the enhanced release of these brain-specific biomarkers was induced by BBB disruption, not tissue damage. Regardless, we will evaluate the feasibility for sonobiopsy to release disease-specific biomarkers by using a pig GBM model in Chapter 4. Second, only a single brain location was targeted and the increase in biomarker release was sufficient to establish the feasibility of the technique. With this single-point sonication, there was no strong correlation between CE volume and GFAP (n = 5, Pearson's correlation coefficient $r = 0.30$, $p = 0.62$) or MBP (n = 7, $r = 0.46$, $p = 0.30$). We will evaluate the efficacy of biomarker release with a large volume sonication in Chapter 4, just as the large volume sonobiopsy improved detection sensitivity in the mouse GBM model.

3.2.4 Conclusion

This study demonstrated the feasibility and safety of FUS-mediated release of brain-specific biomarkers from the brain to the blood in a pig model. A customized sonobiopsy system was designed and built for BBB disruption in pigs, and workflow for sonobiopsy in the pig model was established. Localized BBB opening was verified with contrast-enhanced MRI, while the increased concentration of brain-specific biomarkers, GFAP and MBP, in blood was confirmed with ELISA quantification. This study was the first to verify the hypothesis that FUS-induced BBB opening enables two-way transfer across the BBB in a large animal model. This proof-of-concept study in a large animal model laid the foundation for the future clinical translation of sonobiopsy as a noninvasive and localized brain tumor liquid biopsy technique. This study

suggests that FUS is a promising theranostic tool for not only brain drug delivery but also brain disease diagnosis in combination with liquid biopsies.

Chapter 4: Evaluate feasibility of sonobiopsy in pig GBM model

4.1 Abstract

The objectives for this chapter were to develop a pig GBM model, assess the ability of sonobiopsy to safely release tumor-derived biomarkers, and leverage sonobiopsy to improve the detection sensitivity for clinically relevant GBM mutations. A pig GBM model was developed to characterize the translational implications of sonobiopsy in humans. MRI-guided FUS sonication was performed to locally enhance the BBB permeability of the GBM tumor. Contrast-enhanced T_1-weighted MR images were acquired to evaluate the BBB permeability change. Blood was collected immediately after FUS sonication and droplet digital PCR was used to quantify the levels of brain tumor-specific genetic mutations in the ctDNA. Histological staining was performed to evaluate the potential for off-target tissue damage. Sonobiopsy significantly increased the levels of EGFRvIII ctDNA ($p = 0.016$) and TERT C228T ctDNA ($p = 0.022$). Subsequently, the diagnostic sensitivity of EGFRvIII improved from 28.57% to 100% and that of TERT C228T improved from 42.86% to 71.43%. This study demonstrated that sonobiopsy disrupted the BBB at a spatially-targeted brain location, released tumor-derived DNA into the blood circulation, and enabled timely collection of ctDNA. The evidence from the clinically relevant pig GBM model strongly supports the clinical translation of sonobiopsy for the minimally invasive, spatiotemporally-controlled, and sensitive molecular characterization of brain cancer.

4.2 Assess efficacy to improve detection sensitivity of tumor-specific mutations

A clinically relevant large animal GBM model was needed to support the clinical translation of sonobiopsy because prior work only demonstrated feasibility in a mouse GBM model and a non-tumor pig model. The spontaneous canine glioma model is one large animal model that has similar tumor initiation and progression as humans in a comparable brain size[140,166]. However, the tumor incidence is low and the wide variation in size and location limit the reproducibility of the tumor. A GBM model in immunosuppressed cats has been developed, but the unpredictable tumor growth, small brain size, and unique brain vasculature limit its value in preclinical studies[167]. The pig model is unique for its human-like brain size, anatomy, and vasculature. In addition, pigs are less expensive and pose fewer ethical concerns than a non-human primate[167]. However, only one group in the world had reported successful development of a pig GBM model[167,168], which may be due to technical challenges in adapting existing stereotactic devices for tumor cell implantation in the pig brain, the difficulty in achieving adequate immunosuppression, as well as the associated high cost for the surgery and animal care. Thus, it is critical to develop a robust pig GBM model and evaluate the feasibility for sonobiopsy to improve the detection of GBM-specific mutations and provide convincing evidence that supports the clinical translation of sonobiopsy.

4.2.1 Methods

Preparation of porcine model of GBM

The same U87-EGFRvIII^{+} tumor cells from the mouse GBM model were used for this study. Pigs (breed: Yorkshire white, age: 4 weeks, sex: male, weight: 15 lbs., Oak Hill Genetics, Ewing, IL, USA) were implanted with the tumor cells on day 0 with an established protocol[167,168]. After the pig was sedated by the Veterinary Surgical Services at Washington University, the

head was shaved, prepared for sterile surgery, and immobilized in a stereotactic frame on the operating table. The bite bar and ear bars were positioned to secure the head such that the top of the skull was level with the operating table. A 2–3 cm midline cranial skin incision was made and two 5 mm burr holes were drilled 5 mm posterior from bregma and 7 mm to the subject's right and left from midline without breaking the dura (Dremel, Racine, WI, USA). A 50 µL syringe (Hamilton, Reno, NV, USA) used for tumor cell injection was fixed on the stereotactic frame and positioned in the burr hole with the tip at the dura. The syringe was lowered 9 mm to the injection site and the Micro4 controller (World Precision Instruments, Sarasota, FL, USA) infused 40 µL with a rate of 44 nL/sec. Approximately 3×10^6 cells for each tumor were implanted in pigs. There was a 5-minute delay between infusion completion and needle withdrawal to allow the cells to settle in the tissue and prevent backflow. The burr holes were filled with gel foam and the skin incisions were closed with two layers of sutures. A cyclosporine oral solution (Neoral, Novartis Pharmaceuticals, East Hanover, NJ, USA) was administered (25 mg/kg) twice daily via gavage.

Seven days post-surgery, a contrast-enhanced sagittal T_1-weighted gradient echo MRI scan (TR/TE: 23/3.03 ms; slice thickness: 0.9 mm; in-plane resolution: 0.94×0.94 mm^2; matrix size: 192×192; flip angle: 27°) was acquired on the 3T Siemens PRISMA Fit clinical scanner (Siemens Medical Solutions, Malvern, PA, USA) to validate tumor growth. An intravenous catheter was placed in the ear for ease of microbubble and gadolinium injections. During the treatment and MR scans, a pulse oximeter (Nonin 7500FO, Plymouth, MN, USA) monitored blood oxygen levels and pulse rate, while heated blankets were used to regulate the temperature.

FUS setup and sonobiopsy procedure for pigs

A similar sonobiopsy device and workflow from the non-tumor pig study was used for this study. The pig head was fixed in a stereotactic head frame with a bite bar and head supports and coupled with the transducer. The FUS system (Image Guided Therapy, Pessac, France) included an MR-compatible 15-element transducer with a center frequency of 650 kHz, an aperture of 65 mm, and a radius of curvature of 65 mm, and an adjustable coupling bladder. The FUS system was attached to an MR-compatible motor for enhanced targeting precision. The *in vivo* acoustic pressure was estimated with the top portion of a harvested *ex vivo* pig skull. The axial and lateral FWHM of the transducer was 3.0 mm and 20.0 mm, respectively.

FUS was performed under MR guidance of the 1.5T Philips Ingenia clinical MR scanner (Philips Medical Systems, Inc., Cleveland, OH, USA). Coronal and axial T_2-weighted spin echo MR images were acquired to examine the neuroanatomy for treatment planning (TR/TE: 1300/130 ms; slice thickness: 1.2 mm; in-plane resolution: 0.58×0.58 mm^2; matrix size: 448×448; flip angle: 90°). Coronal and axial T_2^*-weighted gradient echo MR scans were used to visualize the presence of air bubbles in the acoustic coupling media (TR/TE: 710/23 ms; slice thickness: 2.5 mm; in-plane resolution: 0.98x0.98 mm^2; matrix size: 224x224; flip angle 18°). The FUS targeting was performed with the same ThermoGuide workflow as the mouse sonobiopsy. Gadobenate dimeglumine (Gd-BOPTA; Multihance, Bracco Diagnostics Inc., Monroe Township, NJ, USA) was intravenously injected at a dose of 0.2 mL/kg and an axial T_1-weighted ultrafast spoiled gradient echo MR scan was acquired as a pre-FUS baseline (TR/TE: 5/2 ms; slice thickness: 1.5 mm; in-plane resolution: 0.68x0.68 mm^2; matrix size: 320x320; flip angle 10°).

Definity microbubbles (Lantheus Medical Imaging, North Billerica, MA, USA) at a dose of 20 µL/kg were injected intravenously. FUS sonication started 15 seconds prior to

microbubble intravenous injection using the following parameters: frequency: 0.65 MHz, pressure: 2.3 MPa, pulse repetition frequency: 1 Hz, duty cycle: 1%, pulse length: 10 ms, treatment duration: 3 min. The bolus injection was determined by the precedence set by the clinical papers that have a similar injection paradigm[83,127–129] and the observation that the contrast enhancement via bolus is greater than the enhancement via infusion[169]. The 3-minute sonication was previously determined as the time point when all the microbubbles were depleted, as observed by a lack of stable cavitation during passive cavitation detection. The treatment was repeated at 4 individual points spaced 3 mm apart to ensure coverage of the tumor.

After FUS sonication was completed, Gd-BOPTA was intravenously injected and an axial T_1-weighted MR scan was acquired (same parameters as the pre-FUS T_1-weighted sequence) to assess the BBB permeability. Coronal T_2^*-weighted images were acquired (same parameters as pre-FUS) to assess the potential for FUS-induced tissue damage.

Analysis of plasma ctDNA with ddPCR

Pig whole blood (~10 mL) was collected via percutaneous catheter within peripheral vessel using BD Vacutainer K_2 EDTA tubes (Becton Dickinson, Franklin Lakes, NJ, USA). The ddPCR analysis of ctDNA in this study was the same process as the U87-EGFRvIII$^+$ mouse study in Chapter 2.3.

MRI analysis

The MRI analysis in this study was consistent with Chapter 3 for the analysis of the non-tumor pig study.

Histological analysis

Pig brains were harvested and prepared for histological analysis with the same procedure as the nontumor pig study in Chapter 3.2. The remaining histological analysis was the same as that from the U87-EGFRvIII^{+} mouse study in Chapter 2.3.

Statistical analysis

Where appropriate, the data was analyzed with paired samples Wilcoxon signed rank test (Figure 20D, Figure 21A, B, Figure 23C) or unpaired two-sample Wilcoxon signed rank test (Figure 22B, D). Statistical differences were considered significant (*) when $p < 0.05$, (**) when $p < 0.01$, (***) when $p < 0.001$, and (****) when $p < 0.0001$. Descriptive statistics is represented as mean ± SD.

4.2.2 Results

Sonobiopsy enhanced detection of brain tumor-specific mutations

To validate the clinical translatability of sonobiopsy to enhance the detection of brain tumor-specific mutations, a porcine model of GBM was developed. This model was comprised of a bilateral implantation of the same U87-EGFRvIII^{+} cells as the mouse model in the pig cortex followed by immunosuppressant treatment to prevent rejection of the grafted cells[167,168]. The bilateral tumor model capitalized on the unique feature of the large brain volume in pigs and provided the opportunity for sonobiopsy to target two distinct targets in individual pigs. Sonobiopsy was performed approximately 11 days after intracranial implantation. The customized MRI-guided FUS device was developed to sonicate each large animal tumor sequentially (1 hour delay to minimize cross-contamination from biomarker release of the first sonication) in a clinical MRI scanner. A large volume trajectory was employed to ensure sonication of the entire tumor (Figure 20A). Contrast-enhanced T_1-weighted MRI scans confirmed successful BBB disruption of both tumors (Figure 20B). The CE volume significantly increased ($p = 0.031$) from 348.70 ± 358.02 mm^3 to 799.50 ± 501.19 mm^3 (Figure 20C).

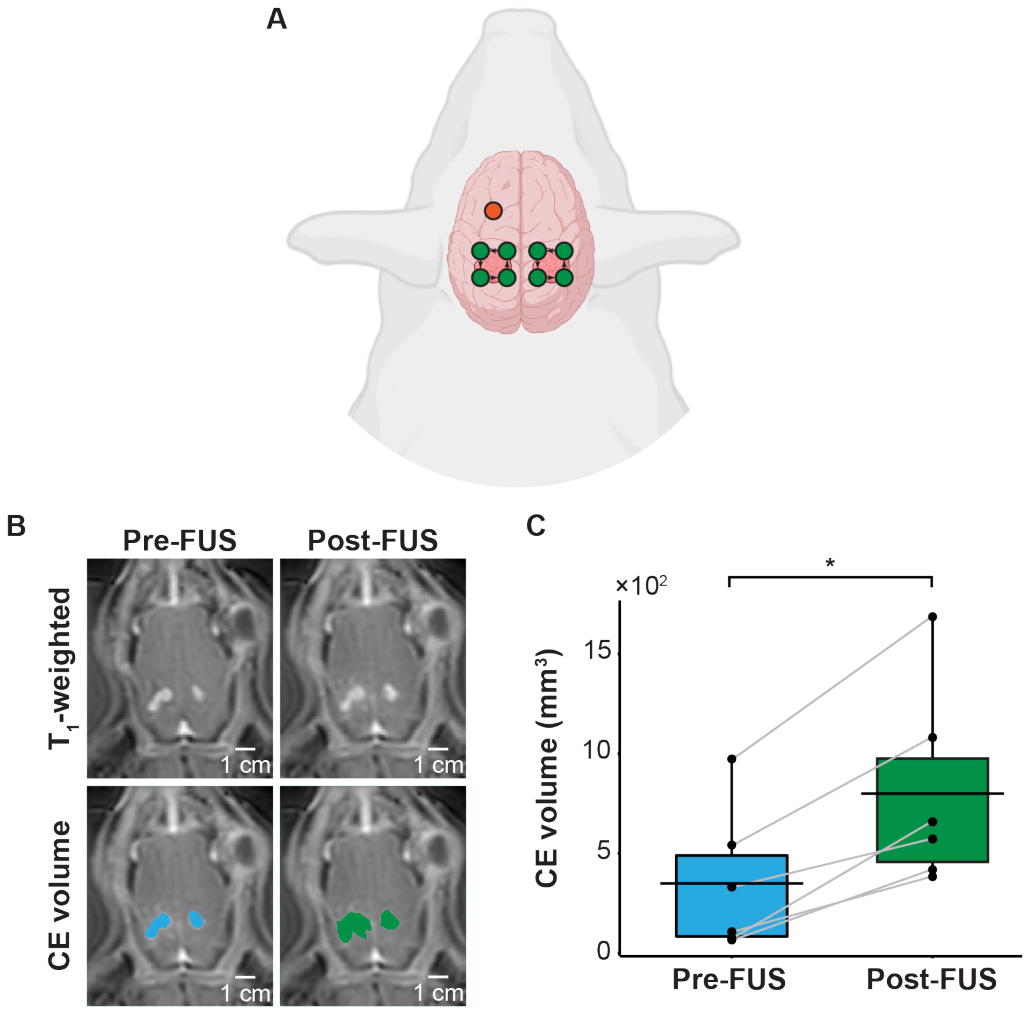

Figure 20. Sonobiopsy successfully disrupted BBB in pig GBM model. (A) The trajectory for large volume sonobiopsy in pig GBM model. A non-tumor area was sonicated to verify successful BBB disruption (orange dot). The large volume trajectory was used to sonicate the entire tumor volume for both tumors in the bilateral GBM model (green dots). (B) CE T_1-weighted MRI scan shows tumor volume (blue area) and FUS-induced BBB disruption (green area). The CE volume significantly increased ($n = 6$; $p = 0.031$; $^*p < 0.05$; paired samples Wilcoxon signed rank test) from 348.70 ± 358.02 mm^3 to 799.50 ± 501.19 mm^3 after sonication of both tumor targets. Black bars indicate mean in C.

Blood samples (5 mL) were collected immediately before and 10 minutes after FUS sonication of each tumor. Sonobiopsy significantly enhanced the release of EGFRvIII ctDNA into the blood by 270-fold (Figure 21A). The plasma level of EGFRvIII ctDNA significantly increased (p = 0.016) from 13.69 ± 28.62 copies/mL to 3697.54 ± 3780.61 copies/mL. Sonobiopsy significantly

enhanced the release of TERT C228T ctDNA by 9-fold with sonobiopsy (Figure 21B). The plasma level of TERT C228T ctDNA significantly increased (p = 0.022) from 13.07 ± 23.08 copies/mL to 112.25 ± 150.75 copies/mL.

Sonobiopsy had a higher detection sensitivity for EGFRvIII ctDNA (TP: 7; FN: 0; sensitivity: 100%; FNR: 0%) than blood LBx (TP: 2; FN: 5; sensitivity: 28.57%; FNR: 71.43%) (Figure 21C). Similarly, sonobiopsy (TP: 7; FN: 3; sensitivity: 70%; FNR: 30%) outperformed blood LBx (TP: 4; FN: 6; sensitivity: 40%; FNR: 60%) in detecting TERT C228T ctDNA (Figure 21C). The sensitivity with 95% confidence interval is shown in Table 4.

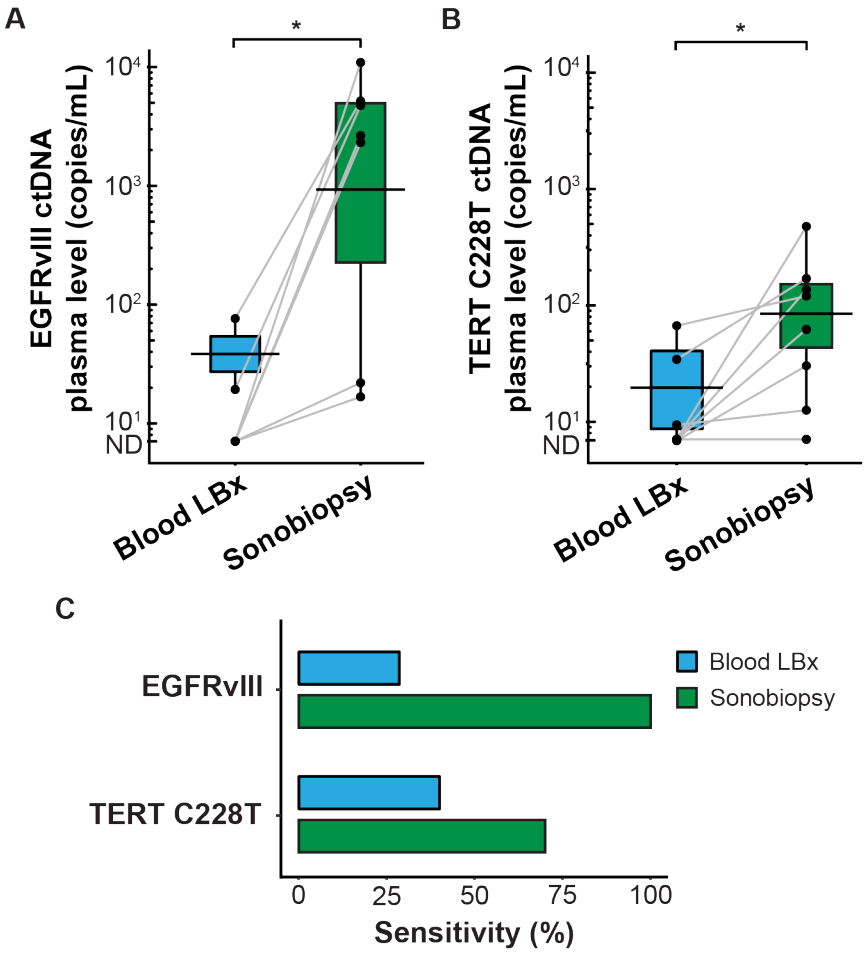

Figure 21. Sonobiopsy increased the detection sensitivity of EGFRvIII and TERT C228T mutations in pig plasma by ddPCR. (A) Sonobiopsy significantly increased plasma levels of

EGFRvIII ctDNA (n = 7; p = 0.016; $^{*}p < 0.05$; paired samples Wilcoxon signed rank test) from 13.69 ± 28.62 copies/mL to 3697.54 ± 3780.61 copies/mL. (B) Sonobiopsy significantly increased the plasma levels of TERT C228T ctDNA (n = 10; p = 0.022; $^{*}p < 0.05$; paired samples Wilcoxon signed rank test) from 13.07 ± 23.08 copies/mL to 112.25 ± 150.75 copies/mL. (C) With ddPCR, sonobiopsy is more sensitive than blood LBx with a detection rate of 100% for EGFRvIII and 71.43% for TERT C228T compared with 28.57% and 42.86% for blood LBx, respectively. Black bars indicate mean in A and B.

Table 4. Sensitivities (±95% confidence interval) of mutation detection in pigs.

	Blood LBx	Sonobiopsy
Mutation	Sensitivity % (95% confidence interval)	Sensitivity % (95% confidence interval)
EGFRvIII	28.57 ± 33.47	100.00 ± 0.00
TERT C228T	42.86 ± 36.66	71.43 ± 33.47

Sonobiopsy did not cause significant off-target damage

The safety risks associated with large animal sonobiopsy were evaluated by histological staining with H&E and TUNEL. H&E staining shows the presence of microhemorrhage near the edge of the tumor in some cases (Figure 22A). However, there was no significant difference in microhemorrhage density between the sonicated tumor ROI and the unsonicated parenchyma (p = 0.20; unpaired two-sample Wilcoxon signed rank test) (Figure 22B). In addition, the TUNEL staining (Figure 22C) suggests there was no significant difference between the number of apoptotic cells in the parenchyma compared with the tumor ROI (p = 0.55) (Figure 22D). MRI was used to evaluate acute tissue damage post-FUS. Abnormalities in the post-FUS T_2^*-weighted images, i.e., signal intensity changes, were observed in 5 of the 6 pigs. A representative of the hypointensity, which may indicate microhemorrhage, is shown in Figure 23B. Though the volume of hypointensity increased post-FUS (87.29 ± 79.80 mm^3) compared with pre-FUS (5.79 ± 10.46 mm^3), this change was not significant (p = 0.063) (Figure 23C). The observed tissue

damage was consistent with the reversible damage observed in clinical trials of FUS-induced BBB disruption for brain drug delivery[83,127,129,170].

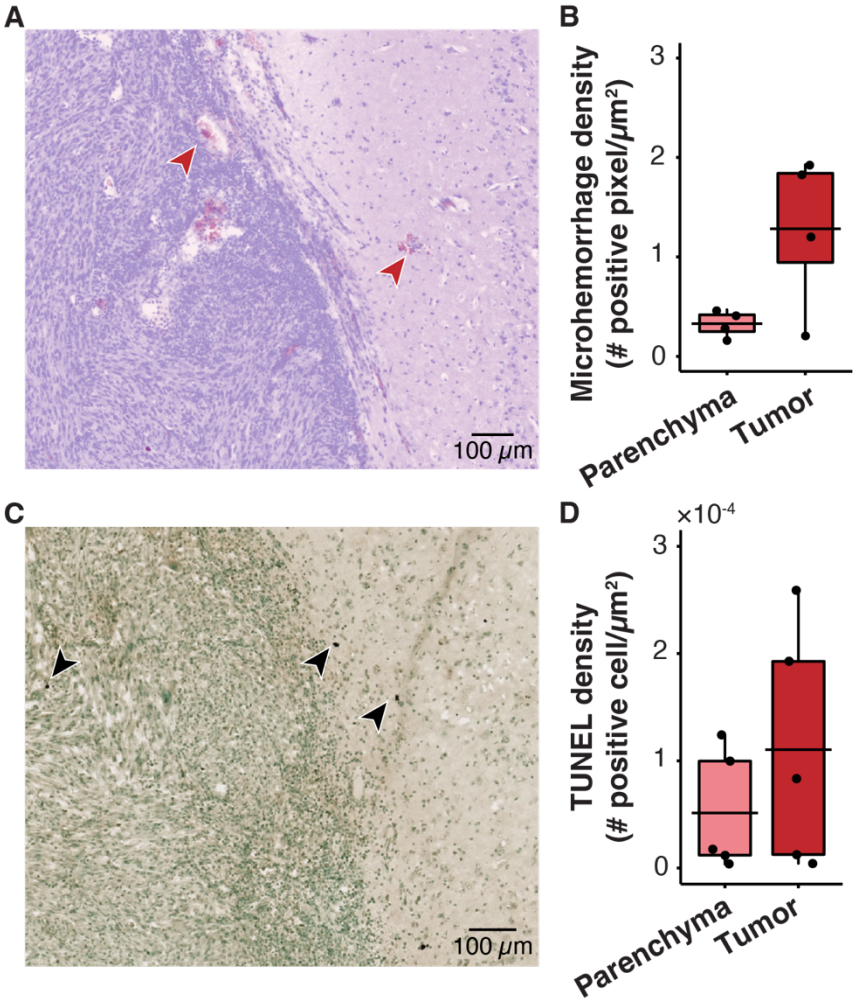

Figure 22. Histological analysis showed no significant off-target tissue damage in pig GBM model. (A) Representative horizontal slice with H&E staining. The microhemorrhage occurs in some cases near the edge of the tumor (red arrows). (B) Microhemorrhage density was not significantly different between parenchyma (n = 4; 0.33 ± 0.13 positive pixels/μm^2) and tumor (n = 4; 1.28 ± 0.79 positive cells/μm^2; p = 0.20; unpaired two-sample Wilcoxon signed rank test). (C) Representative TUNEL staining depicts the apoptotic cells (black arrows). (D) There was no significant difference between the TUNEL density in the tumor (n = 4; 110.40×10^{-4} ± 112.25×10^{-4} positive cells/μm^2) compared with that in the parenchyma (n = 4; 51.34×10^{-4} ± 56.12×10^{-4} positive cells/μm^2; (p = 0.55; unpaired two-sample Wilcoxon signed rank test). Black bars indicate mean in B and D.

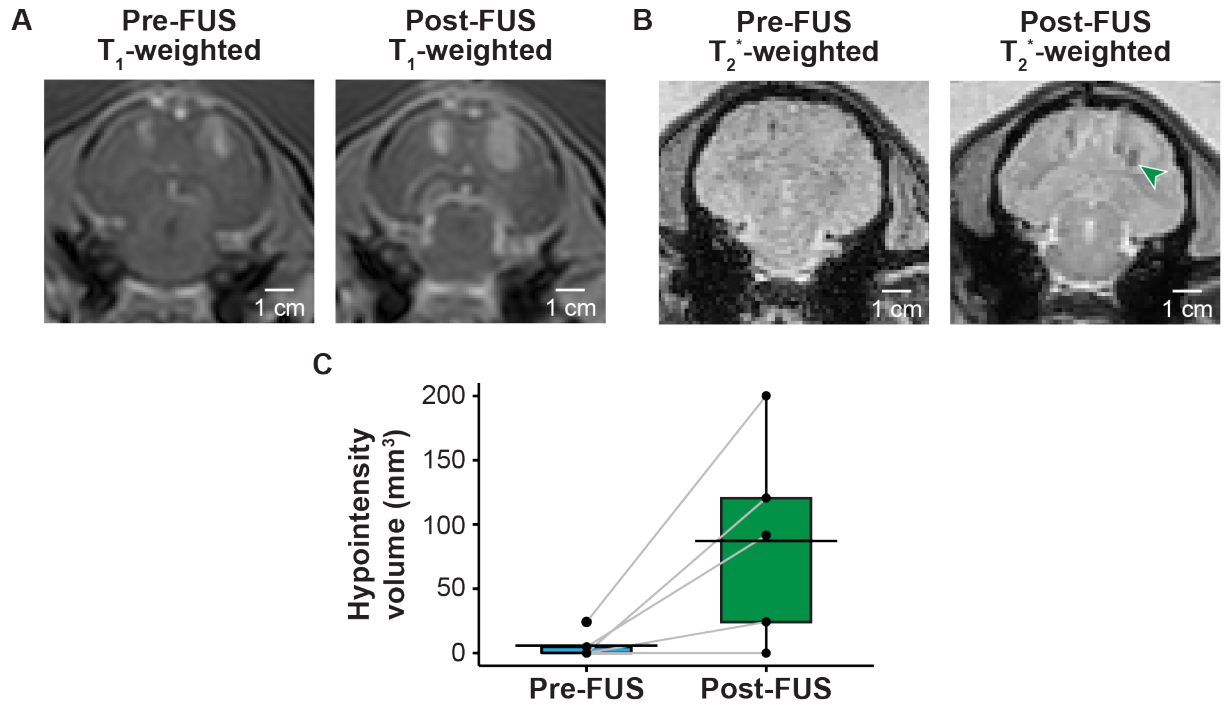

Figure 23. Abnormalities from MRI suggests tissue damage at site of FUS-induced BBB opening. (A) FUS-induced BBB opening observed in T_1-weighted MR image. (B) Abnormality in T_2^*-weighted MR images (green arrow) indicative of microhemorrhage was observed at the FUS sonication target site. (C) There was a nonsignificant increase in hypointensity volume (n = 5; p = 0.063; paired t-test) from the T_2^*-weighted images.

4.2.3 Discussion

The results from this study and the previous U87-EGFRvIII$^+$ mouse model can be combined to extrapolate for the clinical application of sonobiopsy for detecting tumor mutations. In mice, sonobiopsy enhanced the release of EGFRvIII ctDNA by 920-fold and the release of TERT C228T ctDNA by 10-fold when approximately 30% of the total blood volume was collected (0.5 mL collected from 1.7 mL total). In pigs where approximately 5% of the total blood volume (30 mL collected from 620 mL total) was collected, sonobiopsy enhanced the release of EGFRvIII ctDNA by 270-fold and the release of TERT C228T ctDNA by 9-fold. In humans, approximately 1% of the total blood volume can be collected (50 mL collected from 5000 mL total). Assuming linearity between fold change and the fraction of total blood volume collected, it is estimated that

sonobiopsy may increase the release of EGFRvIII ctDNA by 212-fold and TERT C228T ctDNA by 8.5-fold.

Although not statistically significant, the average microhemorrhage and TUNEL densities were higher in the tumor after sonobiopsy than the control group. There was a trend for the pigs where the average microhemorrhage density was higher in the tumor than the parenchyma. In addition, hypointensities that indicate microhemorrhages were observed in the post-FUS T_2^*-weighted MR images for pigs. This evidence indicated that FUS-mediated BBB disruption led to tissue damage in the FUS-targeted region with minimal off-target effects in the parenchyma outside the FUS-targeted region. FUS-induced tissue damage has been reported in previous studies where the abnormalities recovered within 4 days in mice[171] and within 1-2 months in humans[83,129]. In addition, Meng et al., who published the retrospective study on MR-guided focused ultrasound liquid biopsy observed similar damage during the clinical study that was resolved within 24 hours[84,127]. It is not expected that sonobiopsy would contribute to GBM metastasis. Brain tumors, such as GBM, grow locally and rarely metastasize outside the central nervous system (incident rate: 0.4–0.5%)[19,36,172,173]. There have not been any documented cases of metastasis or release of tumor cells in preclinical and clinical studies of FUS-induced BBB disruption. This may be the case because existing assays have low sensitivities compared with advanced techniques that have been developed for the purpose of detecting circulating tumor cells[174,175]. Regardless, the release of tumor cells is not likely because FUS is less invasive than needle biopsy and laser treatment, which could increase the circulating tumor cells[176]. Future studies will be performed to verify the long-term safety of sonobiopsy by performing a survival study and monitoring any neurologic symptoms associated with sonobiopsy and the presence of subacute or chronic tissue damage.

We analyzed the correlations between biomarker release, contrast enhancement, and tissue damage. There was no strong correlation observed in the pig experiment between microhemorrhage density and change in EGFRvIII ctDNA plasma level (n = 4, r = -0.74, p = 0.26), microhemorrhage density and change in CE volume (n = 4, r = -0.62, p = 0.38), or change in EGFRvIII ctDNA plasma level and change in CE volume (n = 6, r = -0.43, p = 0.29). The lack of a strong correlation suggests that FUS-induced biomarker release is a complex process that may be affected by many variables and/or a larger sample size is needed to detect these correlations.

Sonobiopsy has the potential to substantially advance brain cancer diagnosis, treatment monitoring, and recurrence detection. This enhanced capability could have an important impact throughout the continuum of patient care (Figure 24).

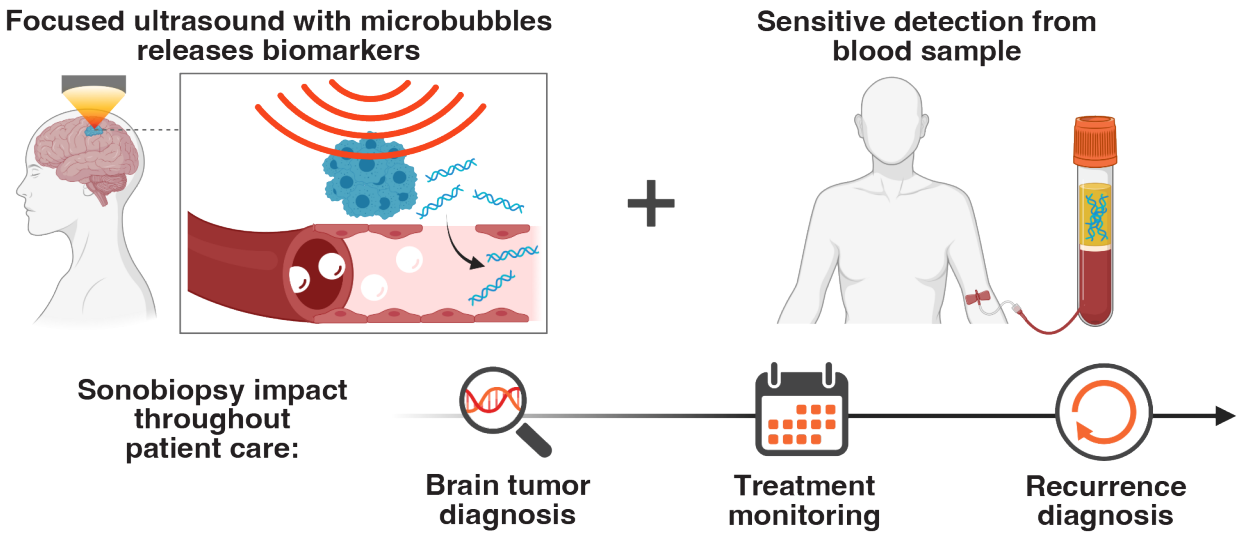

Figure 24. Sonobiopsy can be used throughout the continuum of patient care. Three areas where sonobiopsy will have significant impact are: 1) improve the accuracy and sensitivity of early diagnosis without the need for surgery, 2) enable longitudinal monitoring of disease progression and treatment response, and 3) differentiate between radiation necrosis and tumor recurrence.

In the early diagnostic phase, sonobiopsy could rapidly determine the molecular profile of suspicious lesions observed on neuroimaging scans without the need for surgery.

ctDNA has been identified as a promising biomarker for brain cancer diagnosis. The DNA alterations that drive cancer progression, including mutations, copy number changes, and modifications in key driver genes, are detectable in ctDNA[177]. By understanding the genetic alterations early, the cancer can be more effectively managed. There is a reported specificity >99% to distinguish cancer patients from healthy individuals[178,179]. Technical improvements of analytical approaches may lower the limit of detection to identify mutations with allele frequency as low as 0.1%[180–182]. Despite these metrics that make ctDNA a promising early diagnosis biomarker, the main limitation preventing the use of ctDNA for early diagnosis is that early-stage tumors have a low disease burden and do not shed enough ctDNA[25,177,183]. This poor sensitivity (43–50% for stage I non-brain cancers using CancerSEEK[179] or CAPP-Seq[184]) is the motivation for sonobiopsy. By improving the sensitivity for ctDNA, sonobiopsy may be the missing key to enable early diagnosis with ctDNA, In a mathematical model of plasma biomarker kinetics, Hori and Gambhir showed that a tumor can grow unnoticed for more than 10 years before it is detectable by current clinical blood assays[185]. However, if the biomarker shedding rate, i.e., the number of biomarkers entering the blood circulation, was increased 1000-fold (similar to the 920-fold increase of EGFRvIII ctDNA), the detection time reduces to 5 years. This would be crucial for clinicians to diagnose early-stage tumors and initiate treatment to improve progression-free survival and quality of life. Future studies should be performed to investigate the correlation between tumor volume and sonobiopsy sensitivity to demonstrate the capability of sonobiopsy in early-stage cancer diagnosis.

In the treatment phase, sonobiopsy could also enable repeated longitudinal sampling to monitor treatment response. Though surgical tissue biopsy is the gold standard to sample a tumor's genetic information[19,25], it can only be performed once or twice because of the

surgical risk associated with intracranial surgery. The invasiveness of repeated CSF sampling also precludes routine interrogation necessary to evaluate treatment response[50]. The low sensitivity of blood LBx, which is one of the most minimally invasive biopsy techniques, is a major limiting factor to treatment monitoring. By enriching the blood with brain tumor-derived biomarkers, sonobiopsy could potentially enable the sensitive molecular characterization of brain cancer for longitudinal clinical monitoring. Future studies should investigate how sonobiopsy can be used to monitor the change in genetic profile during treatment and differentiate non-responders who are receiving subtherapeutic doses of therapy from responders who are receiving sufficient treatment.

In the post-treatment phase, sonobiopsy could provide complementary information in situations where assessment based on neuroimaging alone remains challenging (e.g., differentiating treatment-induced pseudoprogression from true relapse)[19,186]. Future studies should evaluate how sonobiopsy can provide a differential diagnosis of radiation-induced injury and tumor recurrence.

4.2.4 Conclusion

This study demonstrated that sonobiopsy can successfully disrupt the BBB at the targeted brain location, release tumor-derived DNA into the blood circulation, and improve the detection sensitivity for two clinically relevant GBM mutations in a pig GBM model. Localized BBB opening was verified with contrast-enhanced MRI and the increased plasma level of ctDNA was confirmed with ddPCR quantification. Further, sonobiopsy improved the detection sensitivity for EGFRvIII and TERT C228T. Immunohistochemical staining revealed that there was no significant off-target tissue damage. This work provides convincing evidence that supports the

clinical translation of sonobiopsy for minimally invasive, spatiotemporally-controlled, and sensitive genetic profiling of GBM tumors.

Chapter 5: Assess feasibility for expanding diagnostic capability of sonobiopsy

5.1 Abstract

The goal for this chapter was to evaluate the feasibility and safety of sonobiopsy in the diagnosis of brain-derived protein biomarkers in a transgenic mouse model of tauopathy (PS19). Sonobiopsy was performed by sonicating the cerebral hemisphere in 2-month-old PS19 and wild-type mice, followed by measurement of plasma phosphorylated tau (pTau) species. Next, spatially-targeted sonobiopsy was performed by sonicating either the cerebral cortex or the hippocampus in 6-month-old PS19 mice. To detect changes in plasma neurofilament light chain (NfL, a biomarker of neurodegeneration) levels, blood was collected before and after sonication. Histological staining was performed to evaluate tissue damage following sonobiopsy. In the 2-month-old mice, sonobiopsy significantly increased the normalized levels of plasma pTau species compared with the conventional blood-based liquid biopsy (pTau-181/mouse-Tau [mTau] ratio: 1.7-fold-increase, $p = 5.8\times10^{-3}$; pTau-231/mTau ratio: 1.4-fold-increase, $p = 4.8\times10^{-2}$). In the 6-month-old PS19 mice, spatially targeted sonobiopsy resulted in a 2.3-fold increase in plasma NfL following the sonication of the hippocampus and cerebral cortex ($p = 2.2\times10^{-4}$). Optimization of the sonobiopsy parameters reduced the observed microhemorrhage density from 1.38 ± 0.92% to 0.52 ± 0.32%. This study demonstrated the feasibility of sonobiopsy to release pTau species and a key marker of neurodegeneration (NfL) to the circulation for the diagnosis of neurodegenerative disorders.

5.2 Evaluate potential of sonobiopsy for neurodegenerative disease

A hallmark of age-related neurodegenerative disorders is the accumulation of abnormal protein species in the brain[187]. In tauopathies, hyperphosphorylation of the tau protein leads to its

dissociation from the microtubule, misfolding, aggregation, and ultimately triggering a secondary cascade of neurotoxic effects that culminates in neuronal death. Akin to driver mutations in brain tumors, there are considerable variations in the post-translational modifications of pathogenic tau species. These variations even exist between individuals that share the same clinical diagnosis (e.g., Alzheimer's disease) and are associated with the disease stage and pathogenicity[188–190]. Characterizing the complex landscape of primary proteinopathies and their secondary effects in neurodegenerative disorders requires brain tissue sampling and histopathological analysis. However, unlike brain tumors, given the potential risks of local injury, invasive brain tissue biopsies are rarely performed for the diagnosis of neurodegenerative disorders[191]. Non-invasive detection of brain-derived pathogenic tau molecules and biomarkers of neurodegeneration is imperative to advance the understanding of tauopathies and develop personalized therapeutic strategies.

Recently, highly sensitive assays have been developed to detect plasma biomarkers of primary proteinopathy and secondary biomarkers that herald downstream processes in neurodegenerative disorders[192,193]. Neurofilament light chain protein (NfL) is one of the emerging secondary biomarkers that is released from damaged axons into the extracellular space and subsequently into the bloodstream[194], and has shown promise to predict disease progression[195]. However, beyond screening for early detection of neurodegenerative disorders, the clinical utility of these blood-based biomarkers faces crucial challenges. First, the BBB acts as a biased filter with differential permeability to brain-derived biomarkers, limiting detectability of various pathogenic protein species[196,197]. Second, traditional fluid biomarkers lack anatomical information on the location of the pathology. Accordingly, variations in disease-related brain-derived biomarkers can be obscured by their release from peripheral tissues or

nonspecific release from normal brain tissue. Therefore, conventional approaches are unable to colocalize the source of biomarker release with observed neuroimaging abnormalities, which is key to establish the underlying molecular pathways driving the neurodegenerative changes. Lastly, biomarker levels in biofluids are in a steady state between their production and clearance. Rapid clearance of biomarkers from biofluids may render them undetectable. In addition, the variability caused by inter-individual/intra-individual differences in clearance rates could limit the accuracy of fluid biomarker approaches. Thus, it is critical to leverage sonobiopsy to enable a sensitive, spatiotemporally-precise diagnosis for neurodegenerative diseases.

5.2.1 Methods

Animal preparation

Two-month-old (first experiment) and 6-month-old (second experiment) male transgenic PS19 (B6;C3-Tg(Prnp-MAPT*P301S)PS19Vle/J) mice were purchased from the Jackson Laboratory (Stock No: 008169). PS19 mice express P301S human tau (1N4R) under the murine prion promoter[198]. Noncarrier wild-type mice were used as controls for the first experiment. The mice were held in a temperature-controlled facility under 12–12 light and dark conditions (light on at 6 AM). They were housed in groups of no more than five. Food and water were provided *ad libitum*. All animal procedures were reviewed and approved by the Institutional Animal Care and Use Committee at Washington University in St. Louis in accordance with the Guide for the Care and Use of Laboratory Animals and the Animal Welfare Act.

Sonobiopsy treatment procedure

The MRI-guided FUS setup from Chapter 2.2 was used for the sonication of the 2-month-old and 6-month-old mice. Coronal and axial T_2-weighted fast spin-echo MRI scans were acquired to image the mouse head and locate the geometrical focus of the transducer (TR/TE: 2000/52ms; slice thickness: 0.5 mm; in-plane resolution: 0.25×0.25 mm2; matrix size: 128×128; averages:

4). The MRI scans were imported to a software program (ThermoGuide, Image Guided Therapy, Pessac, France) to locate the focus of the transducer via 3-point triangulation. For the first experiment, the FUS target covered the hippocampus, piriform cortex, and entorhinal cortex where phosphorylated tau has been observed as young as 1 month of age[199,200]. For the second experiment, FUS sonication was performed at either the cerebral cortex or the hippocampus.

A baseline PCD scan was acquired to ensure sufficient acoustic coupling by the lack of harmonic emission and to validate successful sonication by comparing the change in cavitation activity before and after microbubble injection. Definity microbubbles (Lantheus Medical Imaging, North Billerica, MA) were withdrawn with an additional 18-gauge needle to vent the vial and diluted with preservative-free normal saline to prepare a diluted bolus (microbubble diameter: 1.38 ± 0.13 mm; concentration: $3.87 \pm 0.66 \times 10^9$ microbubbles/mL). Microbubbles were injected 30 seconds prior to the start of FUS sonication (frequency: 1.5 MHz, peak negative pressure: 0.68 MPa, pulse repetition frequency: 5 Hz, duty cycle: 3.35%, pulse length: 6.7 ms, treatment duration: 32 sec) to allow the circulation of bubbles to reach a steady-state. To ensure FUS sonication encompasses both the entorhinal cortex and hippocampus, two sonication targets of 4×1 mm were placed with a 1 mm lateral gap between each other. The transducer moved along the anterior-posterior axis to sonicate the medial target first. There was a 5-minute delay before acquiring a second baseline PCD scan and starting FUS sonication of the lateral target to ensure sufficient microbubble clearance[156,201,202].

After sonication, 50 μL of 1:1 dilution of gadolinium-based MR contrast agent, gadoterate meglumine (Gd-DOTA; Dotarem, Guerbet, Aulnay sous Bois, France) was intravenously injected and followed by a 0.25 mL saline flush. The hyper-enhancement in the T_1-

weighted images would indicate BBB disruption. An axial post-FUS coronal T_1-weighted gradient-echo MRI scan (TR/TE: 108/4 ms; slice thickness: 0.5 mm; in-plane resolution: 0.25×0.25 mm^2; matrix size: 128×128; averages: 16) was performed to quantify the FUS-induced changes in BBB permeability.

Plasma biomarker detection

Mouse blood was collected into EDTA tubes and spun at 6,000 g for 5 min at 4 °C. The top plasma layer was transferred to a 0.5 ml microcentrifuge tube and stored at −80 °C. Frozen plasma samples were thawed at room temperature. All plasma protein measurements were performed in duplicates on a fully automated HD-X Analyzer (Quanterix, Lexington, MA, United States) using ultrahigh sensitive Single Molecule Array (Simoa) kits for mouse tau (Quanterix #102209), pTau-181 (Advantage V2 assay; Quanterix #103714), pTau-231 (Quanterix #102292), and NfL (NF-LIGHT, Quanterix #103186).

MRI analysis

MRI processing and analysis were consistent with Chapter 2.2 for the analysis of the U87-eGFP tumor.

Cavitation analysis

The stable cavitation level was calculated as the root-mean-squared amplitudes of subharmonic ($f_0/2 \pm 0.01$ MHz), ultraharmonic ($3f_0/2 \pm 0.01$ MHz), second harmonic ($2f_0/2 \pm 0.01$ MHz), and third harmonic ($3f_0/2 \pm 0.01$ MHz). The inertial cavitation level was calculated as the root-mean-squared amplitude of the broadband (0.5–4.5 MHz after removing $f_0/2 \pm 0.01$ MHz and $nf_0 \pm 0.01$ MHz where $n = 1, 3/2, 2, 3$) signal.

Histological analysis

After blood collection, the mice were transcardially perfused with phosphate-buffered saline followed by 4% paraformaldehyde. Mouse brains were collected and fixed to prepare for paraffin

sectioning. The whole brain was sectioned horizontally to ensure the treated tissue was captured in each slice. H&E staining was performed to examine red blood cell extravasation and cellular injury. The slices were imaged on the Axio Scan.Z1 Slide Scanner (Zeiss, Oberkochen, Germany). QuPath v0.2.0[108] was used to detect the presence of FUS-induced hemorrhage. After color deconvolution (hematoxylin vs. eosin), areas of microhemorrhage were detected using the positive-pixel count algorithm. Microhemorrhage density was calculated as the percentage of microhemorrhage surface area over the entire evaluated surface area (%).

Statistical analysis

All statistical analyses were performed using R v4.1.2 (https://www.r-project.org/). Plots were generated using the *ggplot2* package v3.3.5 in R[203]. All absolute plasma levels of biomarkers were log-transformed before statistical comparison, while the plasma level ratios were directly compared with no transformation. Two sample t-tests were performed to assess group differences. Paired t-tests were conducted to compare pre/post-sonication levels of NfL and ipsi/contralateral microhemorrhage density. As we expected increases in biomarker levels and tissue microhemorrhage density following FUS treatment, all reported *p*-values are one-tailed, unless otherwise specified (considered significant at $p < 0.05$).

5.2.2 Results

Sonobiopsy increased normalized concentration of circulating phosphorylated tau species

We first demonstrated the efficacy of sonobiopsy to enrich the blood with pathologic pTau species compared with conventional blood-based liquid biopsy. FUS sonication was performed at the right cerebral hemisphere (Figure 25A), which includes areas that exhibit early pTau deposition in young PS19 mice, i.e. hippocampus, piriform cortex, and entorhinal cortex[199,200]. Blood samples were collected via cardiac puncture after either FUS sonication in the sonobiopsy group

or no treatment in the blood LBx group. The plasma levels of pTau species, phosphorylated at threonine position 181 (pTau-181) and threonine position 231 (pTau-231), were measured in FUS-treated PS19 and wild-type mice. In addition, the plasma levels of mouse tau (total mTau) were measured as an internal control to normalize pTau levels in plasma.

Following FUS sonication, contrast-enhanced T_1-weighted MRI was performed to verify and quantify BBB opening (Figure 25B,C). Except for one wild-type mouse, successful BBB opening was observed in the targeted right hemisphere of all FUS-treated mice (wild-type: 7 out of 8; PS19: 7 out of 7). There was no significant group difference in the volume of FUS-mediated BBB opening and no evidence of off-target BBB opening. The wild-type mouse with no evidence of BBB opening following FUS was excluded from further analysis.

As expected, the absolute levels of pTau species were higher in the PS19 mice than the wild-type mice (Figure 26). Though the absolute levels of pTau species were not significantly higher in the FUS-treated PS19 mice (Figure 26), there was a significant 1.7-fold increase (p = 0.0058) in the normalized levels of pTau-181 (pTau-181/mTau) from the sonobiopsy-treated PS19 mice (0.58 ± 0.18) compared with the blood LBx PS19 mice (0.34 ± 0.10) (Figure 25D). There was a significant 1.4-fold increase (p = 0.048) in the normalized levels of pTau-231 (pTau-231/mTau) from the sonobiopsy-treated PS19 mice (0.17 ± 0.06) compared with the blood LBx PS19 mice (0.12 ± 0.03) (Figure 25E). There was no significant increase in normalized pTau-181 or pTau-231 levels between the sonobiopsy and blood LBx groups for wild-type mice (Figure 27). Taken together, these results show that sonobiopsy selectively increased the normalized levels of circulating pTau species in pathologic mice because sonobiopsy had no effect on wild-type mice.

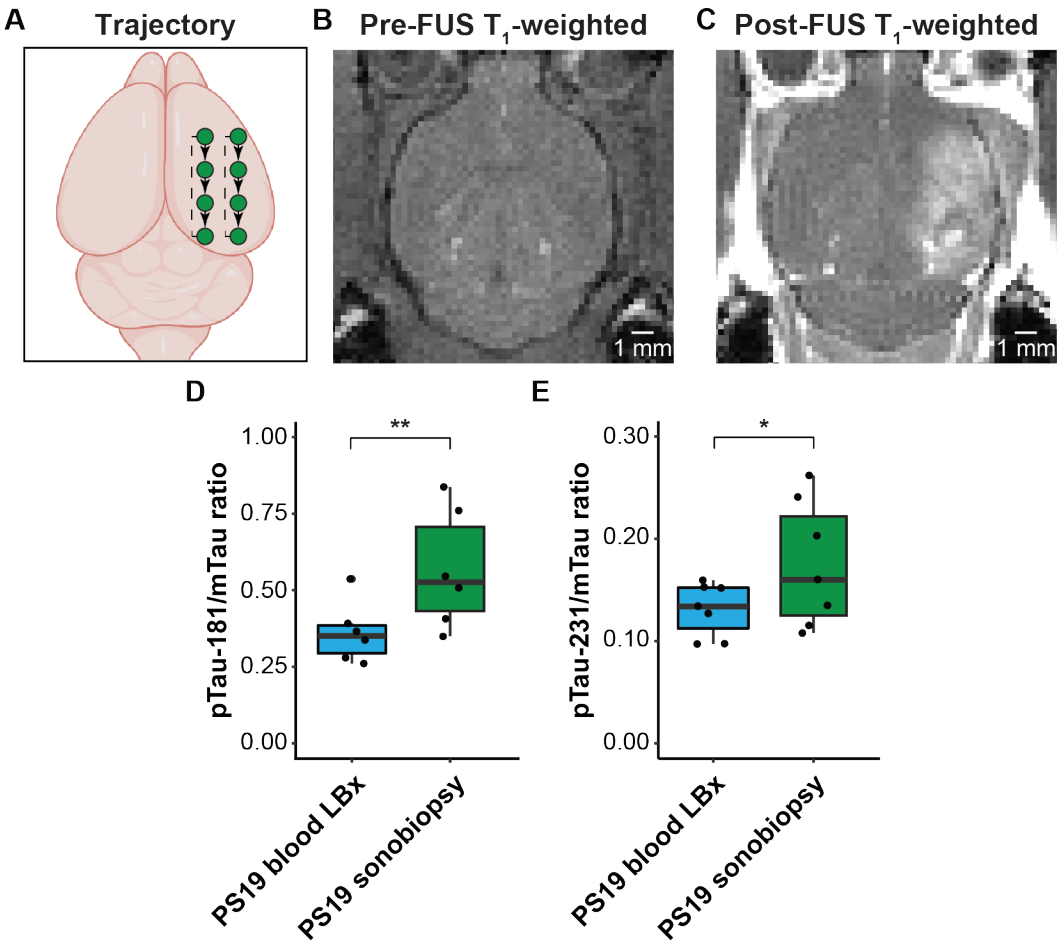

Figure 25. Sonobiopsy changed the composition of circulating phosphorylated tau species. (A) Schematic of the FUS trajectory targeting the right cerebral hemisphere. (B) T_1-weighted MRI scans were acquired before FUS. (C) Post-FUS T_1-weighted MRI scans confirmed FUS-induced BBB disruption as a signal enhancement. There was no significant group difference ($p = 0.71$) in the volume of FUS-mediated BBB opening between PS19 (30.9 ± 17.9 mm^3) and wild-type mice (35.1 ± 22.9 mm^3). (D) In PS19 mice, the normalized pTau-181 (pTau-181/mTau ratio) was significantly greater ($p = 0.0058$) in the sonobiopsy group ($n = 6$; 0.57 ± 0.19) compared with the normalized pTau-181 in the blood LBx group ($n = 6$; 0.36 ± 0.09). (E) In PS19 mice, the normalized pTau-231 (pTau-231/mTau ratio) was significantly greater ($p = 0.048$) in the sonobiopsy group ($n = 6$; 0.17 ± 0.06) compared with the normalized pTau-181 in the blood LBx group ($n = 6$; 0.13 ± 0.03). Black bars indicate median in D and E.

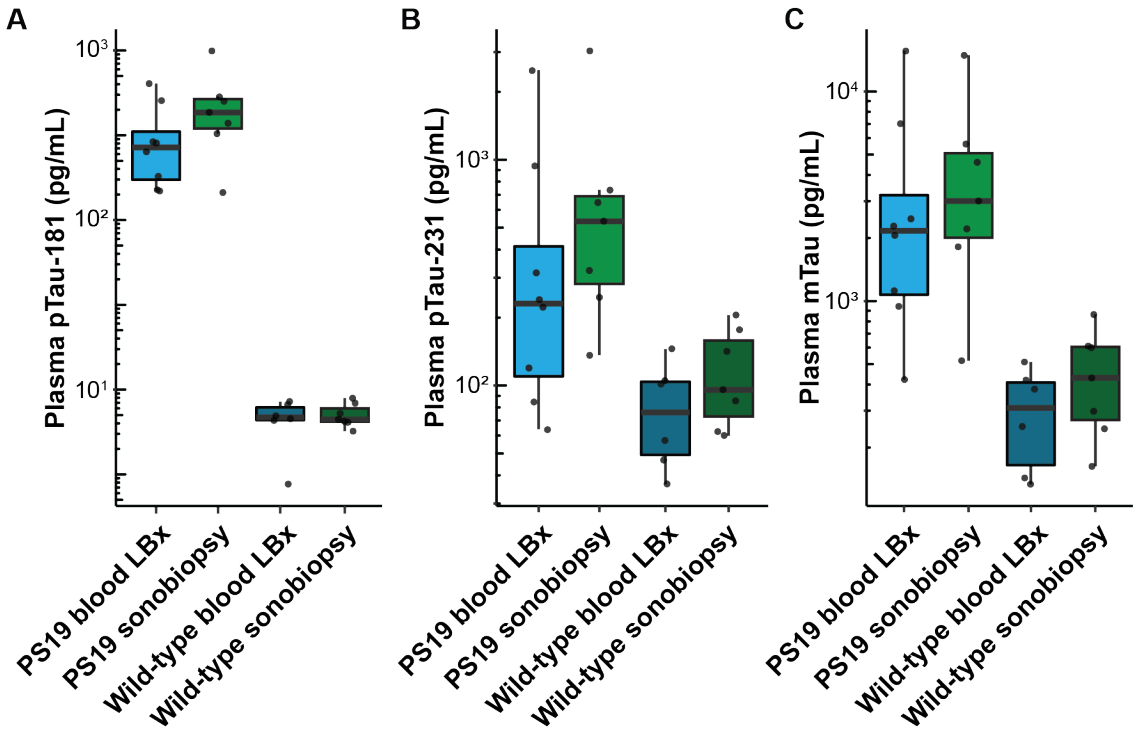

Figure 26. Sonobiopsy slightly increased absolute levels of pTau-181, pTau-231, and mTau. (A) The plasma level of pTau-181 in the PS19 mice (blood LBx: 1523.99 ± 1486.82 pg/mL; sonobiopsy: 1643.18 ± 972.79 pg/mL) was higher than the wild-type mice (blood LBx: 0.47 ± 0.22 pg/mL; sonobiopsy: 0.52 ± 0.17 pg/mL). There was no significant difference in the absolute plasma level of pTau-181 in either the PS19 (p = 0.56) or the wild-type mice (p = 0.64). (B) The absolute level of pTau-231 in the plasma of the PS19 mice (blood LBx: 628.05 ± 873.03 pg/mL; sonobiopsy: 806.95 ± 1002.73 pg/mL) was higher than the wild-type mice (blood LBx: 81.91 ± 41.83 pg/mL; sonobiopsy: 118.03 ± 57.13 pg/mL). There was no significant difference in the absolute plasma level of pTau-231 in either the PS19 (p = 0.64) or the wild-type mice (p = 0.89). (C) The absolute level of mTau was greater in the PS19 mice (blood LBx: 4403.10 ± 5393.20 pg/mL; sonobiopsy: 4669.61 ± 4831.65 pg/mL) compared with the wild-type mice (blood LBx: 306.79 ± 155.02 pg/mL; sonobiopsy: 458.35 ± 246.66 pg/mL). There was no significant difference in the absolute plasma level of mTau in either the PS19 (p = 0.54) or the wild-type mice (p = 0.90). Black bars indicate median in A, B, and C.

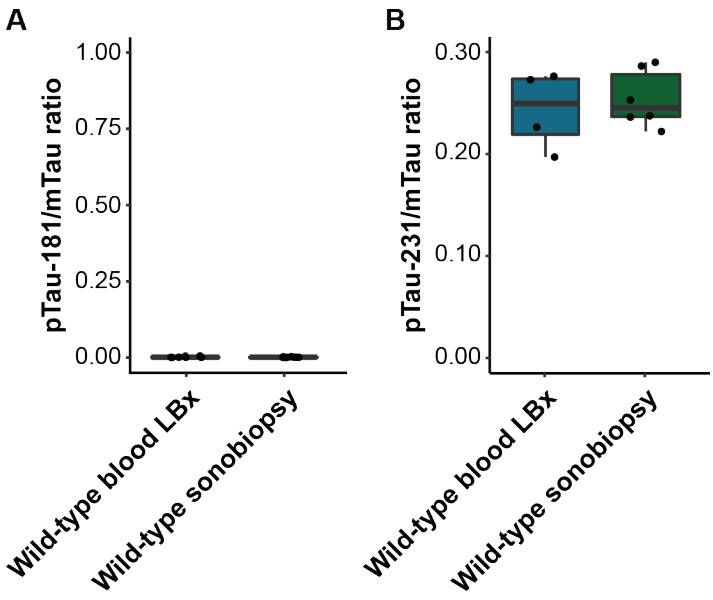

*Figure 27. Sonobiopsy did not increase the normalized pTau-181 and pTau-231 levels for wild-type mice. (A) The normalized level of pTau-181 in the sonobiopsy group ($1.4\times10^{-3} \pm 0.9\times10^{-3}$) was not significantly different ($p = 0.71$) from that in the blood LBx group ($1.9\times10^{-3} \pm 1.8\times10^{-3}$). **(B)** The normalized level of pTau-231 in the sonobiopsy group (0.27 ± 0.05) was not significantly different ($p = 0.55$) from that in the blood LBx group (0.27 ± 0.06). Black bars indicate median in A and B.*

Sonobiopsy released NfL

We further evaluated the capability of sonobiopsy to release secondary biomarkers of tauopathy. We also assessed the potential of survival blood collection and the capability to target specific brain regions. NfL is one of the most abundant intermediate cytoskeletal filaments in neurons and a sensitive marker for neurodegeneration[194]. In the second experiment, we sought to determine whether sonobiopsy would increase the levels of circulating NfL in the early neurodegenerative stages of PS19 mice (6-month-old)[198]. We applied a lower peak negative pressure compared with that used in the first experiment (0.4 MPa vs. 0.68 MPa) and targeted smaller brain areas. Specifically, we either targeted the ventral anterolateral cerebral cortex, i.e., olfactory cerebral cortex that includes the piriform cortex and amygdala (Figure 28A), or the hippocampus (Figure 28D), which both exhibit early neurodegenerative changes in PS19 mice[198,204]. The selection

of a smaller target region of the brain enabled examination of the regional specificity of sonobiopsy by evaluating the biomarker release from each localized region. Similar to the first experiment, contrast-enhanced T_1-weighted MRI was performed to verify and quantify the volume of BBB disruption. Figure 28B and Figure 28E are representative pre-FUS MR images for either the olfactory cerebral cortex or the hippocampus, respectively. Figure 28C and Figure 28F are representative post-FUS MR images for each target, respectively. There was no significant difference in the volume of FUS-mediated BBB disruption between mice treated at the olfactory cerebral cortex or the hippocampus.

To mitigate the effects of variabilities in baseline plasma biomarkers among the PS19 mice, a pre-post study design was adopted to evaluate changes in NfL levels by sampling blood before FUS (sample A, submandibular blood collection), 15 minutes after FUS (sample B, submandibular blood collection), and 45–60 minutes after FUS (sample C, terminal cardiac puncture). In the blood LBx group, a submandibular blood collection (sample A) was followed by a cardiac puncture (sample C). Unlike sample C, NfL measurements of samples A and B in the FUS treated group are directly comparable, as these samples were obtained using the same blood collection method, and plasma NfL levels were measured in the same batch of reagents with the same sample dilutions. There was a 2.3-fold (SD: 0.78) increase in plasma NfL following FUS (sample B vs. sample A: $p = 2.2 \times 10^{-4}$, n = 8; Figure 28G). Next, we calculated the ratio of plasma NfL levels in the terminal cardiac sample (sample C) to sample A (submandibular blood; pre-sonication in the FUS-treated group). Compared to the blood LBx group (non-FUS treated PS19 mice), the sample C to sample A plasma NfL level ratio was 2.6-fold higher in the FUS-treated PS19 mice ($p = 0.011$; FUS-treated mice: 3.3 ± 2.2, n=9; blood LBx mice: 1.3 ± 0.22, n = 5) (Figure 28H). There was no clear difference in FUS-induced NfL release between the hippocampus and the

cortex sonicated groups (Figure 28G). Altogether, by accounting for the baseline levels of plasma NfL, our findings show that sonication of the hippocampus and cerebral cortex leads to an increase in NfL plasma levels in the PS19 mice even at an early neurodegenerative stage.

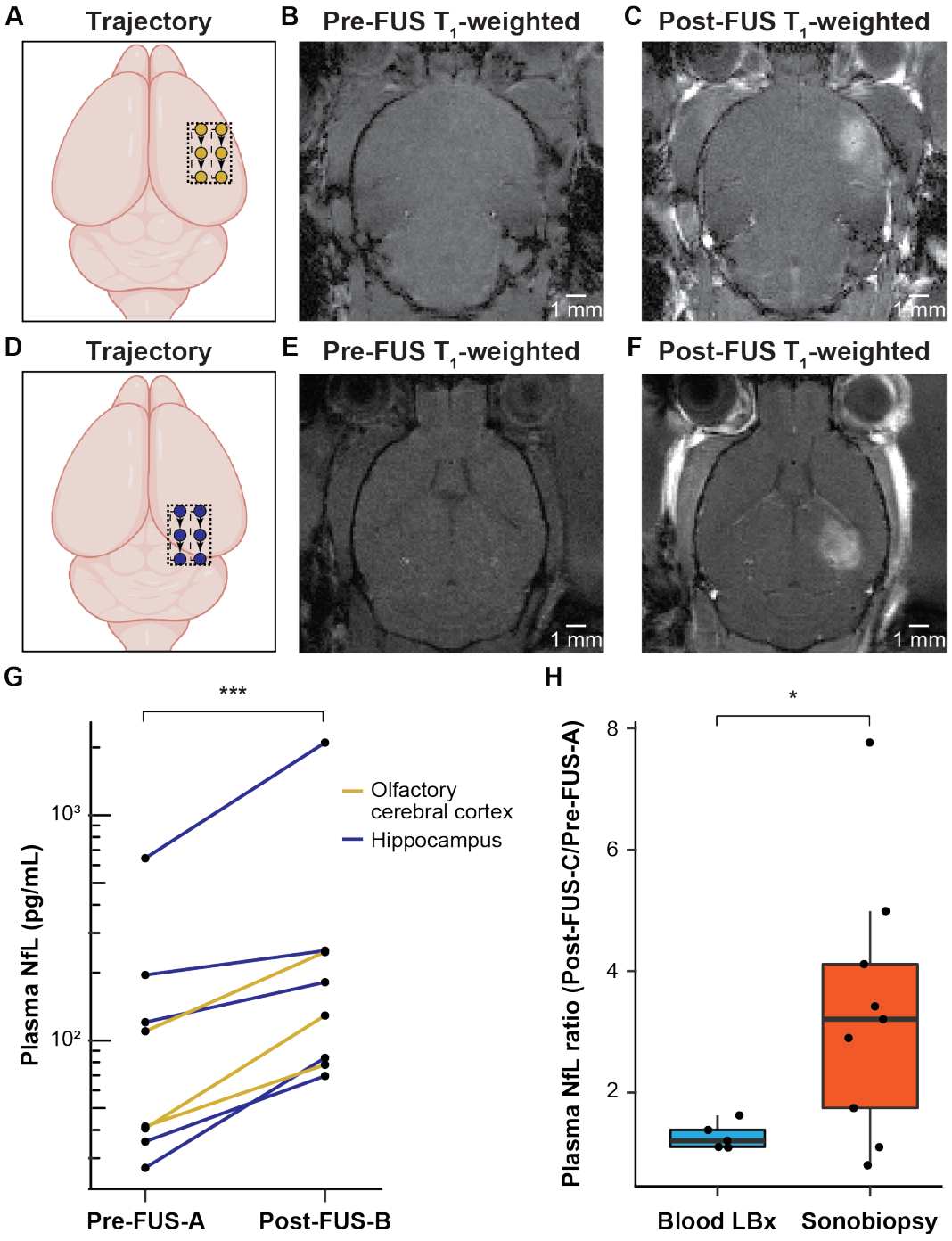

Figure 28. Sonobiopsy enhanced levels of plasma NfL. (A) Schematic of the FUS trajectory targeting the olfactory cerebral cortex (piriform cortex and amygdala). (B) T_1-weighted MRI scans were acquired before FUS. (C) Post-FUS T_1-weighted MRI scans confirmed FUS-induced BBB disruption as a signal enhancement. (D) Schematic of the FUS trajectory targeting the hippocampus. (E) T_1-weighted MRI scans were acquired before FUS. (F) FUS T_1-weighted MRI scans confirmed FUS-induced BBB disruption as a signal enhancement. There was no significant difference ($p = 0.17$) in the volume of FUS-mediated BBB disruption between mice treated at the olfactory cerebral cortex (21.7 ± 5.8 mm^3) or the hippocampus (15.4 ± 5.8 mm^3). (G) Sonobiopsy resulted in a 2.3-fold (± 0.78) increase in plasma NfL levels ($n = 8$; $p = 2.2 \times 10^{-4}$). (H) The normalized plasma NfL (post-FUS/pre-FUS) was significantly greater ($p = 0.011$) in the sonobiopsy group ($n = 9$; 3.34 ± 2.15) than the blood LBx group ($n = 5$; 1.28 ± 0.22). Black bars indicate median in H.

Sonobiopsy did not pose significant safety risks

To detect potential FUS-induced tissue damage and hemorrhage in the targeted brain areas, histological examination and hematoxylin and eosin staining (H&E) staining were performed. Microhemorrhage density was calculated as the percentage of microhemorrhage surface area to the treated hemisphere, using the positive pixel algorithm in QuPath[108]. The H&E staining of the 2-month-old PS19 mice (Figure 29A) revealed that the microhemorrhage density in the treated hemisphere ($1.38 \pm 0.92\%$) was significantly greater than that in the contralateral hemisphere ($0.48 \pm 0.44\%$; $p = 0.04$, n = 8) (Figure 29B). For the 6-month-old PS19 mice that were treated with a lower FUS peak negative pressure and a smaller target region, the H&E staining (Figure 29C) revealed no increase in the microhemorrhage density in the treated hemisphere ($0.52 \pm 0.32\%$), compared to the contralateral hemisphere ($0.42 \pm 0.29\%$; $p = 0.2$, n = 13) (Figure 29D). With these optimal sonobiopsy parameters, the microhemorrhage area decreased from 0.051 ± 0.038 mm^2 to 0.013 ± 0.007 mm^2 (Figure 30). In addition, transcranial passive cavitation detection (PCD) was used to monitor microbubble cavitation during focused ultrasound sonication. The inertial cavitation dose, a predictor for FUS-induced tissue damage, was minimal for all FUS-treated groups in experiments 1 and 2 (Figure 31). Altogether, these suggest that even minimal brain injury can be avoided by lowering FUS peak negative pressure.

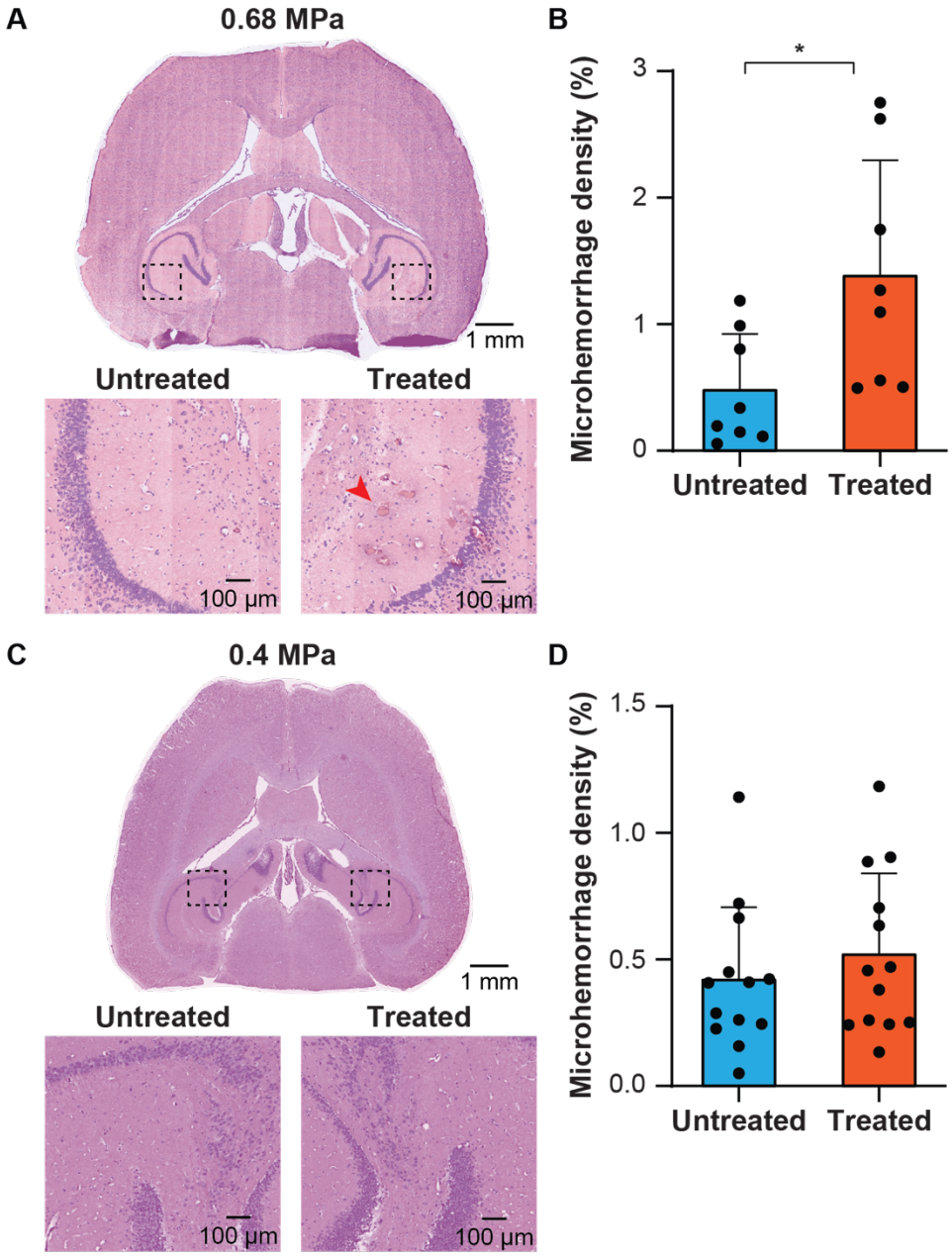

Figure 29. Minimal brain injury avoided by reducing FUS pressure. (A) Representative H&E staining for experiment 1 (0.68 MPa sonication with 2-month-old mice). (B) There was a significant increase ($p = 0.04$) in microhemorrhage density (red arrow) in the treated hemisphere (1.38 ± 0.92%) compared with the contralateral hemisphere (0.48 ± 0.44%). (C) Representative H&E staining for experiment 2 (0.4 MPa sonication with 6-month-old mice). (D) There was no significant difference ($p = 0.20$) in the microhemorrhage density in the treated hemisphere (0.52 ± 0.32%) compared with the contralateral hemisphere (0.42 ± 0.29%).

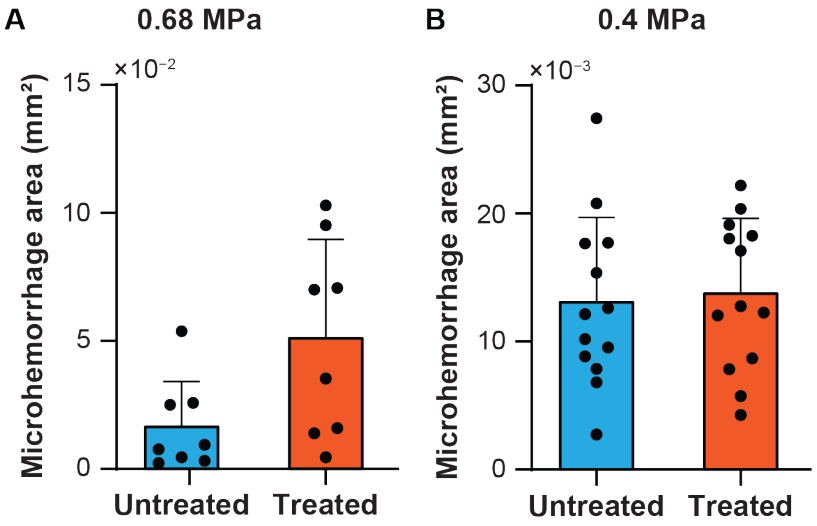

*Figure 30. Safety assessment of sonobiopsy via histological examination. (A) In experiment 1, there was a non-significant (p = 0.07) sub-millimeter increase in average microhemorrhage area in the treated hemisphere (0.051 ± 0.038 mm²) compared with that in the contralateral hemisphere (0.017 ± 0.018 mm²). **(B)** In experiment 2, there was no significant difference (p = 0.39) in the average microhemorrhage area in the treated hemisphere (0.014 ± 0.006 mm²) compared with the contralateral hemisphere (0.013 ± 0.017 mm²).*

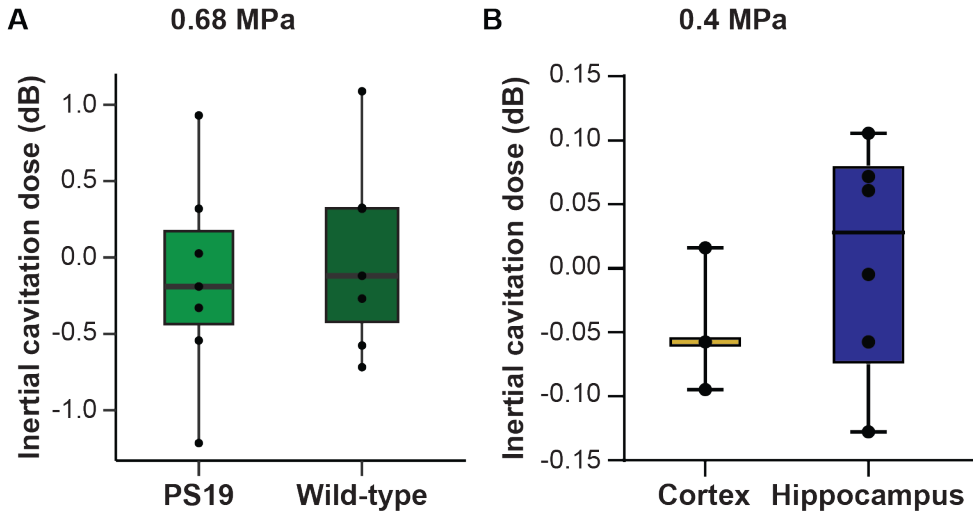

*Figure 31. Safety assessment of sonobiopsy via passive cavitation detection. (A) In experiment 1, the inertial cavitation dose was minimal with no significant difference (p = 0.67) between the FUS-treated groups (PS19: -0.14 ± 0.68 dB; wild-type: 0.007 ± 0.623 dB), suggesting a low risk for tissue damage. **(B)** In experiment 2, there was minimal inertial cavitation dose during sonication of the 6-month-old PS19 mice at the piriform cortex (-0.045 ± 0.056 dB) and the hippocampus (0.008 ± 0.089 dB). Black bars indicate median in A and B.*

5.2.3 Discussion

We observed high baseline levels of pTau-181, pTau-231, and NfL. This is expected as these are established biomarkers for tauopathy and neurodegeneration that are readily detectable in plasma with highly sensitive assays. As a result, the apparent yields of sonobiopsy have likely been dampened by high plasma levels under the baseline condition. To further complicate diagnostic performance, pTau-181, pTau-231, and NfL had large variabilities across subjects, which likely reflects the heterogeneity observed in neuropathology in PS19 mice[205]. Moreover, inter-individual variations in nonspecific release and clearance of biomarkers can result in large differences in baseline levels of brain-derived plasma biomarkers in the steady state. In clinical practice, such variations that are not related to the underlying disease process can decrease the sensitivity and specificity of plasma biomarkers in conventional liquid biopsy. In contrast, sonobiopsy can directly address this limitation by allowing blood sample collection before and after sonication to compare the biomarker levels within each subject. In this way, the changes in plasma biomarker levels from their baseline following sonication can be used to directly estimate FUS-induced release of brain-derived biomarkers from the targeted area in the brain.

The observed microhemorrhage can be avoided by lowering the peak negative pressure, while still achieving sonobiopsy-induced biomarker release. This suggests that sonobiopsy can be successfully performed without gross brain injury by optimizing FUS parameters. Though the higher peak negative pressure increases the efficacy of sonobiopsy and BBB opening, the efficacy likely varies depending on the biomarker molecular properties, including the kinetics of biomarker influx into and clearance from the plasma[206]. In addition, there was no strong correlation between CE volume and normalized pTau-181 (n = 6, Pearson's correlation coefficient $r = 0.79$, $p = 0.06$) or normalized pTau-231 (n = 7, $r = -0.021$, $p = 0.97$) or NfL (n = 9, $r = 0.013$, $p = 0.97$). Altogether, there must be a balance between the safety and

efficacy of sonobiopsy by optimizing the FUS parameters and plasma sampling times for the biomarker of interest and targeted tissue. Future studies should perform a comprehensive safety study that includes histopathology examination and behavioral assays that evaluate motor coordination and cognitive function, such as Y-maze, Barnes maze, and pole test[207–209], which may be affected by FUS sonication of the hippocampus.

Though sonobiopsy was effective when targeting the hippocampus or the olfactory cerebral cortex, there was no significant difference in NfL levels between these specific brain regions. This may be explained by early neurodegenerative changes in both targeted areas in PS19 mice[198,204]. The spatial resolution of sonobiopsy can be leveraged to colocalize the biomarkers released by sonobiopsy with nonspecific imaging biomarkers of neurodegeneration, such as decreased metabolism[210] or tissue microstructural deficits[211,212]. Further, the yield of sonobiopsy can be increased by targeting areas with a higher burden of protein deposits, e.g., tau deposits using tau-specific radiotracers for positron emission tomography[213]. This spatially-resolved diagnosis can improve the multimodal diagnosis by combining molecular biomarkers with imaging biomarkers, thus providing an additional benchmark for the accurate diagnosis of the molecular subtypes and regional patterns of neurodegenerative disorders that predict disease progression and outcome.

This proof-of-concept study had several limitations. First, this study demonstrated that sonobiopsy could result in a quantitative increase in plasma biomarker levels. Future studies are needed to examine the qualitative effects of sonobiopsy on plasma biomarkers with an in-depth analysis of post-translational modifications (e.g., phosphorylation, acetylation), size distribution, and oligomerization. Second, while this study showed that sonobiopsy can be successfully performed with relatively low FUS acoustic pressures (0.4 MPa) and by targeting a

specific brain area, we did not perform a comprehensive optimization study to characterize the effects of FUS parameters and blood collection time. While these effects have been described in different settings and macromolecules (RNA or DNA), it is conceivable that the dynamics and kinetics of sonobiopsy would be different for protein biomarkers. Lastly, this study focused on proteins with relatively small molecular weights (48–68 kDa)[214,215]. Future studies are needed to determine the generalizability of sonobiopsy in releasing larger brain-derived biomarkers and its efficacy to release biomarkers of primarily intracellular proteinopathies (e.g., α-synucleinopathies)[216].

5.2.4 Conclusion

This study demonstrated the feasibility and safety of sonobiopsy to enhance the detection of both biomarkers of the primary pathogenic process (e.g., post-translational modifications of the tau protein) and secondary neurodegeneration. As such, sonobiopsy can provide a window into the molecular derangements in the central nervous system milieu that are otherwise hidden or distorted by the BBB to resolve inter-individual variations in brain proteinopathies. This proof-of-principle study was the first to open the door for noninvasive and spatially targeted diagnosis and monitoring of neurodegenerative disorders with sonobiopsy.

Chapter 6: Conclusions and future perspectives

6.1 Conclusion

In this thesis, focused ultrasound-enabled blood-based liquid biopsy (sonobiopsy) was studied and evaluated for the release of tumor-derived biomarkers in small and large animal models of glioblastoma (GBM) and the release of biomarkers of neurodegeneration in a mouse model of Alzheimer's disease. The optimization of the sonobiopsy parameters was critical to increase biomarker release to the blood and improve the detection sensitivity for two GBM mutations while reducing the risk for tissue damage. An MRI-guided sonobiopsy system was developed to establish the potential for clinical translation by demonstrating the increase in brain-derived biomarkers in the plasma in a large animal model. Sonobiopsy increased the release of tumor-derived biomarkers and improved the sensitivity for detecting two GBM mutations in a clinically relevant pig GBM model. The clinical applications of sonobiopsy can be expanded to other brain diseases after it was shown that sonobiopsy can provide a noninvasive diagnosis of neurodegenerative diseases. Altogether, sonobiopsy enabled a minimally invasive, sensitive, molecular diagnosis of GBM and Alzheimer's disease by significantly increasing the level of disease-specific biomarkers in the plasma. This thesis provided convincing evidence that support the adoption of sonobiopsy for the molecular characterization of brain diseases and laid the foundation for future clinical applications.

6.2 Perspectives

The clinical need for this technique is clear: current methods to characterize the genetic profile of brain diseases have limitations that preclude the adoption of a minimally invasive, sensitive, molecular diagnosis. Focused ultrasound (FUS) is the key to addressing this unmet need by disrupting the primary limitation hindering blood-based liquid biopsies, the blood-brain barrier

(BBB). Though the underlying mechanism of sonobiopsy, FUS-induced BBB disruption, has been developed for more than two decades, the "two-way trafficking" hypothesis that posited biomarkers can be released from the brain tissue into the blood circulation was novel. And though the FUS-induced release of biomarkers has been sparsely studied since 2009, it has not yet been used for diagnosing brain cancer, nor has it been translated to large animals and patients. Our work paved the way for FUS to be a diagnostic tool and acquire the genetic profile of brain diseases.

Informational interviews with neurosurgeons and neuro-oncologists underscore the importance for sonobiopsy as a minimally invasive, sensitive, molecular diagnosis. This has potential applications to screen patients during initial diagnosis, identify actionable targets for precision medicine, assist drug trials as a companion diagnostic to monitor response to therapy, and differentiate tumor progression from pseudoprogression, among others. Importantly, sonobiopsy is a platform technology that can be used in neuro-oncology, neurology, and psychiatry. The feasibility, safety, and efficacy of sonobiopsy for the various neurological disorders must be further explored with the goal of translating the technology to the clinic.

References

1. Chen K-T, Chai W-Y, Lin Y-J, et al. Neuronavigation-guided focused ultrasound for transcranial blood-brain barrier opening and immunostimulation in brain tumors. Sci Adv. 2021; 7: eabd0772.

2. Johnson DR, O'Neill BP. Glioblastoma survival in the United States before and during the temozolomide era. J Neurooncol. 2012; 107: 359–64.

3. Stupp R, Mason WP, van den Bent MJ, et al. Radiotherapy plus Concomitant and Adjuvant Temozolomide for Glioblastoma. N Engl J Med. 2005; 352: 987–96.

4. Birkó Z, Nagy B, Klekner Á, Virga J. Novel Molecular Markers in Glioblastoma—Benefits of Liquid Biopsy. Int J Mol Sci. 2020; 21: 7522.

5. Shukla G, Alexander GS, Bakas S, et al. Advanced magnetic resonance imaging in glioblastoma: a review. Chinese Clin Oncol. 2017; 6: 40–40.

6. Hammoud MA, Sawaya R, Shi W, Thall PF, Leeds NE. Prognostic significance of preoperative MRI scans in glioblastoma multiforme. J Neurooncol. 1996; 27: 65–73.

7. Gillies RJ, Kinahan PE, Hricak H. Radiomics: Images Are More than Pictures, They Are Data. Radiology. 2016; 278: 563–77.

8. Le NQK, Hung TNK, Do DT, et al. Radiomics-based machine learning model for efficiently classifying transcriptome subtypes in glioblastoma patients from MRI. Comput Biol Med. 2021; 132: 104320.

9. Macyszyn L, Akbari H, Pisapia JM, et al. Imaging patterns predict patient survival and molecular subtype in glioblastoma via machine learning techniques. Neuro Oncol. 2016; 18: 417–25.

10. Abdelaziz O, Eshra M, Belal A, Elshafei M. Diagnostic Value of Magnetic Resonance Spectroscopy Compared with Stereotactic Biopsy of Intra-axial Brain Lesions. J Neurol Surg Part A Cent Eur Neurosurg. 2016; 77: 283–90.

11. Gao T, Zou C, Li Y, et al. A Brief History and Future Prospects of CEST MRI in Clinical Non-Brain Tumor Imaging. Int J Mol Sci. 2021; 22: 11559.

12. Rathore S, Akbari H, Rozycki M, et al. Radiomic MRI signature reveals three distinct subtypes of glioblastoma with different clinical and molecular characteristics, offering prognostic value beyond IDH1. Sci Rep. 2018; 8: 5087.

13. Bae S, Choi YS, Ahn SS, et al. Radiomic MRI Phenotyping of Glioblastoma: Improving Survival Prediction. Radiology. 2018; 289: 797–806.

14. McGirt MJ, Woodworth GF, Coon AL, et al. Independent predictors of morbidity after image-guided stereotactic brain biopsy: a risk assessment of 270 cases. J Neurosurg. 2005; 102: 897–901.

15. Ragel BT, Ryken TC, Kalkanis SN, et al. The role of biopsy in the management of patients with presumed diffuse low grade glioma: A systematic review and evidence-based clinical practice guideline. J Neurooncol. 2015; 125: 481–501.

16. Mahlokozera T, Vellimana AK, Li T, et al. Biological and therapeutic implications of multisector sequencing in newly diagnosed glioblastoma. Neuro Oncol. 2018; 20: 472–83.

17. Chaudhuri AA, Chabon JJ, Lovejoy AF, et al. Early detection of molecular residual disease in localized lung cancer by circulating tumor DNA profiling. Cancer Discov. 2017; 7: 1394–403.

18. Nassiri F, Chakravarthy A, Feng S, et al. Detection and discrimination of intracranial tumors using plasma cell-free DNA methylomes. Nat Med. 2020; 26: 1044–7.

19. Müller Bark J, Kulasinghe A, Chua B, Day BW, Punyadeera C. Circulating biomarkers in patients with glioblastoma. Br J Cancer. 2020; 122: 295–305.

20. Saenz-Antoñanzas A, Auzmendi-Iriarte J, Carrasco-Garcia E, et al. Liquid biopsy in glioblastoma: Opportunities, applications and challenges. Cancers (Basel). 2019; 11: 1–20.

21. Muralidharan K, Yekula A, Small JL, et al. TERT promoter mutation analysis for blood-based diagnosis and monitoring of gliomas. Clin Cancer Res. 2021; 27: 169–78.

22. Bagley SJ, Ali Nabavizadeh S, Mays JJ, et al. Clinical utility of plasma cell-free DNA in adult patients with newly diagnosed glioblastoma: A pilot prospective study. Clin Cancer Res. 2020; 26: 397–407.

23. De Rubis G, Rajeev Krishnan S, Bebawy M. Liquid Biopsies in Cancer Diagnosis, Monitoring, and Prognosis. Trends Pharmacol Sci. 2019; 40: 172–86.

24. Qiu J, Xu J, Zhang K, et al. Refining cancer management using integrated liquid biopsy. Theranostics. 2020; 10: 2374–84.

25. Wu J, Hu S, Zhang L, et al. Tumor circulome in the liquid biopsies for cancer diagnosis and prognosis. Theranostics. 2020; 10: 4544–56.

26. Pasini L, Ulivi P. Liquid Biopsy for the Detection of Resistance Mechanisms in NSCLC: Comparison of Different Blood Biomarkers. J Clin Med. 2019; 8: 998.

27. Mizobuchi Y, Nakajima K, Fujihara T, et al. The risk of hemorrhage in stereotactic biopsy for brain tumors. J Med Investig. 2019; 66: 314–8.

28. Bardelli A, Pantel K. Liquid Biopsies, What We Do Not Know (Yet). Cancer Cell. 2017; 31: 172–9.

29. Piccioni DE, Achrol AS, Kiedrowski LA, et al. Analysis of cell-free circulating tumor DNA in 419 patients with glioblastoma and other primary brain tumors. CNS Oncol. 2019; 8: CNS34.

30. Szymanski JJ, Sundby RT, Jones PA, et al. Cell-free DNA ultra-low-pass whole genome sequencing to distinguish malignant peripheral nerve sheath tumor (MPNST) from its benign precursor lesion: A cross-sectional study. Abbosh C, Ed. PLOS Med. 2021; 18: e1003734.

31. Shi J, Zhang R, Li J, Zhang R. Size profile of cell-free DNA: A beacon guiding the practice and innovation of clinical testing. Theranostics. 2020; 10: 4737–48.

32. Tzimagiorgis G, Michailidou EZ, Kritis A, Markopoulos AK, Kouidou S. Recovering circulating extracellular or cell-free RNA from bodily fluids. Cancer Epidemiol. 2011; 35: 580–9.

33. Elazezy M, Joosse SA. Techniques of using circulating tumor DNA as a liquid biopsy component in cancer management. Comput Struct Biotechnol J. 2018; 16: 370–8.

34. Crowley E, Di Nicolantonio F, Loupakis F, Bardelli A. Liquid biopsy: Monitoring cancer-genetics in the blood. Nat Rev Clin Oncol. 2013; 10: 472–84.

35. Mair R, Mouliere F, Smith CG, et al. Measurement of plasma cell-free mitochondrial tumor DNA improves detection of glioblastoma in patient-derived orthotopic xenograft models. Cancer Res. 2019; 79: 220–30.

36. Bettegowda C, Sausen M, Leary RJ, et al. Detection of Circulating Tumor DNA in Early- and Late-Stage Human Malignancies. Sci Transl Med. 2014; 6: 224ra24-224ra24.

37. Pantel K, Alix-Panabières C. Liquid biopsy and minimal residual disease — latest advances and implications for cure. Nat Rev Clin Oncol. 2019; 16: 409–24.

38. Goldman JW, Noor ZS, Remon J, Besse B, Rosenfeld N. Are liquid biopsies a surrogate for tissue EGFR testing? Ann Oncol. 2018; 29: i38–46.

39. Schwaederle M, Husain H, Fanta PT, et al. Detection rate of actionable mutations in diverse cancers using a biopsy-free (blood) circulating tumor cell DNA assay. Oncotarget. 2016; 7: 9707–17.

40. Zill OA, Banks KC, Fairclough SR, et al. The landscape of actionable genomic alterations in cell-free circulating tumor DNA from 21,807 advanced cancer patients. Clin Cancer Res. 2018; 24: 3528–38.

41. Mouliere F, Chandrananda D, Piskorz AM, et al. Enhanced detection of circulating tumor DNA by fragment size analysis. Sci Transl Med. 2018; 10: 1–14.

42. Kwapisz D. The first liquid biopsy test approved. Is it a new era of mutation testing for non-small cell lung cancer? Ann Transl Med. 2017; 5: 46.

43. Alix-Panabières C, Pantel K. Clinical applications of circulating tumor cells and circulating tumor DNA as liquid biopsy. Cancer Discov. 2016; 6: 479–91.

44. Chen WW, Balaj L, Liau LM, et al. Beaming and droplet digital PCR analysis of mutant IDH1 mRNA in glioma patient serum and cerebrospinal fluid extracellular vesicles. Mol

Ther - Nucleic Acids. 2013; 2: e109.

45. Boisselier B, Pérez-Larraya JG, Rossetto M, et al. Detection of IDH1 mutation in the plasma of patients with glioma. Neurology. 2012; 79: 1693–8.

46. Chandran VI, Welinder C, Mansson AS, et al. Ultrasensitive immunoprofiling of plasma extracellular vesicles identifies syndecan-1 as a potential tool for minimally invasive diagnosis of glioma. Clin Cancer Res. 2019; 25: 3115–27.

47. De Mattos-Arruda L, Mayor R, Ng CKY, et al. Cerebrospinal fluid-derived circulating tumour DNA better represents the genomic alterations of brain tumours than plasma. Nat Commun. 2015; 6: 1–6.

48. Pan C, Diplas BH, Chen X, et al. Molecular profiling of tumors of the brainstem by sequencing of CSF-derived circulating tumor DNA. Acta Neuropathol. 2019; 137: 297–306.

49. Figueroa JM, Skog J, Akers J, et al. Detection of wild-Type EGFR amplification and EGFRvIII mutation in CSF-derived extracellular vesicles of glioblastoma patients. Neuro Oncol. 2017; 19: 1494–502.

50. Yan W, Xu T, Zhu H, Yu J. Clinical Applications of Cerebrospinal Fluid Circulating Tumor DNA as a Liquid Biopsy for Central Nervous System Tumors. Onco Targets Ther. 2020; Volume 13: 719–31.

51. Miller AM, Shah RH, Pentsova EI, et al. Tracking tumour evolution in glioma through liquid biopsies of cerebrospinal fluid. Nature. 2019; 565: 654–8.

52. Zonta E, Garlan F, Pécuchet N, et al. Multiplex detection of rare mutations by picoliter droplet based digital PCR: Sensitivity and specificity considerations. PLoS One. 2016; 11: 1–20.

53. Shankar GM, Balaj L, Stott SL, Nahed B, Carter BS. Liquid biopsy for brain tumors. Expert Rev Mol Diagn. 2017; 17: 943.

54. Butler HJ, Brennan PM, Cameron JM, et al. Development of high-throughput ATR-FTIR technology for rapid triage of brain cancer. Nat Commun. 2019; 10: 4501.

55. Connolly ID, Li Y, Gephart MH, Nagpal S. The "Liquid Biopsy": the Role of Circulating DNA and RNA in Central Nervous System Tumors. Curr Neurol Neurosci Rep. 2016; 16: 1–8.

56. Van Tellingen O, Yetkin-Arik B, De Gooijer MC, et al. Overcoming the blood-brain tumor barrier for effective glioblastoma treatment. Drug Resist Updat. 2015; 19: 1–12.

57. Wei KC, Chu PC, Wang HYJ, et al. Focused Ultrasound-Induced Blood-Brain Barrier Opening to Enhance Temozolomide Delivery for Glioblastoma Treatment: A Preclinical Study. PLoS One. 2013; 8: 1–10.

58. Arvanitis CD, Ferraro GB, Jain RK. The blood–brain barrier and blood–tumour barrier in

brain tumours and metastases. Nat Rev Cancer. 2020; 20: 26–41.

59. Hynynen K, McDannold N, Vykhodtseva N, Jolesz FA. Noninvasive MR Imaging–guided Focal Opening of the Blood-Brain Barrier in Rabbits. Radiology. 2001; 220: 640–6.

60. Chen H, Kreider W, Brayman AA, Bailey MR, Matula TJ. Blood Vessel Deformations on Microsecond Time Scales by Ultrasonic Cavitation. Phys Rev Lett. 2011; 106: 034301.

61. Novell A, Kamimura HAS, Cafarelli A, et al. A new safety index based on intrapulse monitoring of ultra-harmonic cavitation during ultrasound-induced blood-brain barrier opening procedures. Sci Rep. 2020; 10: 10088.

62. Liu HL, Hua MY, Chen PY, et al. Blood-brain barrier disruption with focused ultrasound enhances delivery of chemotherapeutic drugs for glioblastoma treatment. Radiology. 2010; 255: 415–25.

63. Wei H-J, Upadhyayula PS, Pouliopoulos AN, et al. Focused Ultrasound-Mediated Blood-Brain Barrier Opening Increases Delivery and Efficacy of Etoposide for Glioblastoma Treatment. Int J Radiat Oncol. 2021; 110: 539–50.

64. Englander ZK, Wei H-J, Pouliopoulos AN, et al. Focused ultrasound mediated blood–brain barrier opening is safe and feasible in a murine pontine glioma model. Sci Rep. 2021; 11: 6521.

65. Meng Y, Suppiah S, Mithani K, et al. Current and emerging brain applications of MR-guided focused ultrasound. J Ther Ultrasound. 2017; 5: 1–9.

66. Lee EJ, Fomenko A, Lozano AM. Magnetic resonance-guided focused ultrasound : Current status and future perspectives in thermal ablation and blood-brain barrier opening. J Korean Neurosurg Soc. 2019; 62: 10–26.

67. Alli S, Figueiredo CA, Golbourn B, et al. Brainstem blood brain barrier disruption using focused ultrasound: A demonstration of feasibility and enhanced doxorubicin delivery. J Control Release. 2018; 281: 29–41.

68. Ye D, Sultan D, Zhang X, et al. Focused ultrasound-enabled delivery of radiolabeled nanoclusters to the pons. J Control Release. 2018; 283: 143–50.

69. Meng Y, Suppiah S, Surendrakumar S, Bigioni L, Lipsman N. Low-intensity MR-guided focused ultrasound mediated disruption of the blood-brain barrier for intracranial metastatic diseases. Front Oncol. 2018; 8: 1–8.

70. Leinenga G, Götz J. Scanning ultrasound removes amyloid-β and restores memory in an Alzheimer's disease mouse model. Sci Transl Med. 2015; 7.

71. Karakatsani ME, Wang S, Samiotaki G, et al. Amelioration of the nigrostriatal pathway facilitated by ultrasound-mediated neurotrophic delivery in early Parkinson's disease. J Control Release. 2019; 303: 289–301.

72. Yoon K, Lee W, Chen E, et al. Localized Blood–Brain Barrier Opening in Ovine Model

Using Image-Guided Transcranial Focused Ultrasound. Ultrasound Med Biol. 2019; 45: 2391–404.

73. Liu HL, Chen PY, Yang HW, et al. In vivo MR quantification of superparamagnetic iron oxide nanoparticle leakage during low-frequency-ultrasound-induced blood-brain barrier opening in swine. J Magn Reson Imaging. 2011; 34: 1313–24.

74. Huang Y, Alkins R, Schwartz ML, Hynynen K. Opening the Blood-Brain Barrier with MR Imaging–guided Focused Ultrasound: Preclinical Testing on a Trans–Human Skull Porcine Model. Radiology. 2017; 282: 123–30.

75. Xie F, Boska MD, Lof J, et al. Effects of Transcranial Ultrasound and Intravenous Microbubbles on Blood Brain Barrier Permeability in a Large Animal Model. Ultrasound Med Biol. 2008; 34: 2028–34.

76. Downs ME, Buch A, Karakatsani ME, Konofagou EE, Ferrera VP. Blood-Brain Barrier Opening in Behaving Non-Human Primates via Focused Ultrasound with Systemically Administered Microbubbles. Sci Rep. 2015; 5: 1–13.

77. Marquet F, Teichert T, Wu SY, et al. Real-time, transcranial monitoring of safe blood-brain barrier opening in non-human primates. PLoS One. 2014; 9: 1–11.

78. Arvanitis CD, Livingstone MS, Vykhodtseva N, McDannold N. Controlled ultrasound-induced blood-brain barrier disruption using passive acoustic emissions monitoring. PLoS One. 2012; 7: e45783.

79. Mainprize T, Lipsman N, Huang Y, et al. Blood-Brain Barrier Opening in Primary Brain Tumors with Non-invasive MR-Guided Focused Ultrasound: A Clinical Safety and Feasibility Study. Sci Rep. 2019; 9: 321.

80. Carpentier A, Canney M, Vignot A, et al. Clinical trial of blood-brain barrier disruption by pulsed ultrasound. Sci Transl Med. 2016; 8: 343re2.

81. Asquier N, Bouchoux G, Canney M, et al. Blood-brain barrier disruption in humans using an implantable ultrasound device: Quantification with MR images and correlation with local acoustic pressure. J Neurosurg. 2020; 132: 875–83.

82. Idbaih A, Canney M, Belin L, et al. Safety and feasibility of repeated and transient blood-brain barrier disruption by pulsed ultrasound in patients with recurrent glioblastoma. Clin Cancer Res. 2019; 25: 3793–801.

83. Park SH, Kim MJ, Jung HH, et al. Safety and feasibility of multiple blood-brain barrier disruptions for the treatment of glioblastoma in patients undergoing standard adjuvant chemotherapy. J Neurosurg. 2020; 1: 1–9.

84. Meng Y, Pople CB, Suppiah S, et al. MR-guided focused ultrasound liquid biopsy enriches circulating biomarkers in patients with brain tumors. Neuro Oncol. 2021; 23: 1789–97.

85. Chen K-T, Lin Y-J, Chai W-Y, et al. Neuronavigation-guided focused ultrasound

(NaviFUS) for transcranial blood-brain barrier opening in recurrent glioblastoma patients: clinical trial protocol. Ann Transl Med. 2020; 8: 673–673.

86. D'Souza AL, Tseng JR, Pauly KB, et al. A strategy for blood biomarker amplification and localization using ultrasound. Proc Natl Acad Sci U S A. 2009; 106: 17152–7.

87. Chevillet JR, Khokhlova TD, Giraldez MD, et al. Release of cell-free microRNA tumor biomarkers into the blood circulation with pulsed focused ultrasound: A noninvasive, anatomically localized, molecular liquid biopsy. Radiology. 2017; 283: 158–67.

88. Paproski RJ, Jovel J, Wong GKS, Lewis JD, Zemp RJ. Enhanced detection of cancer biomarkers in blood-borne extracellular vesicles using nanodroplets and focused ultrasound. Cancer Res. 2017; 77: 3–13.

89. D'Souza AL, Chevillet JR, Ghanouni P, et al. Tumor characterization by ultrasound-release of multiple protein and microRNA biomarkers, preclinical and clinical evidence. PLoS One. 2018; 13: 1–17.

90. Hussein F, Antonescu C, Karshafian R. Ultrasound and microbubble induced release from intracellular compartments. BMC Biotechnol. 2017; 17: 1–12.

91. Forbrich A, Paproski R, Hitt M, Zemp R. Comparing efficiency of micro-RNA and mRNA biomarker liberation with microbubble-enhanced ultrasound exposure. Ultrasound Med Biol. 2014; 40: 2207–16.

92. Peng D, Xu T, Mason TJ, Wu W. A study of ovarian cancer biomarker amplification using ultrasound for early stage detection. Ultrasonics. 2014; 54: 451–4.

93. Maciulevičius M, Tamošiūnas M, Jakštys B, et al. Investigation of microbubble cavitation-induced calcein release from cells in vitro. Ultrasound Med Biol. 2016; 42: 2990–3000.

94. Zhu L, Cheng G, Ye D, et al. Focused Ultrasound-enabled Brain Tumor Liquid Biopsy. Sci Rep. 2018; 8: 6553.

95. Russano M, Napolitano A, Ribelli G, et al. Liquid biopsy and tumor heterogeneity in metastatic solid tumors: the potentiality of blood samples. J Exp Clin Cancer Res. 2020; 39: 95.

96. Ilié M, Hofman P. Pros: Can tissue biopsy be replaced by liquid biopsy? Transl Lung Cancer Res. 2016; 5: 420–3.

97. Nasrallah MP, Binder ZA, Oldridge DA, et al. Molecular Neuropathology in Practice: Clinical Profiling and Integrative Analysis of Molecular Alterations in Glioblastoma. Acad Pathol. 2019; 6: 237428951984835.

98. Schwarzenbach H, Hoon DSB, Pantel K. Cell-free nucleic acids as biomarkers in cancer patients. Nat Rev Cancer. 2011; 11: 426–37.

99. Kustanovich A, Schwartz R, Peretz T, Grinshpun A. Life and death of circulating cell-free

DNA. Cancer Biol Ther. 2019; 20: 1057–67.

100. Shin J, Kong C, Cho JS, et al. Focused ultrasound–mediated noninvasive blood-brain barrier modulation: preclinical examination of efficacy and safety in various sonication parameters. Neurosurg Focus. 2018; 44: E15.

101. Song K-H, Harvey BK, Borden MA. State-of-the-art of microbubble-assisted blood-brain barrier disruption. Theranostics. 2018; 8: 4393–408.

102. Tsai H-C, Tsai C-H, Chen W-S, et al. Safety evaluation of frequent application of microbubble-enhanced focused ultrasound blood-brain-barrier opening. Sci Rep. 2018; 8: 17720.

103. Diaz LA, Jr, Bardelli A. Liquid biopsies: Genotyping circulating tumor DNA. J Clin Oncol. 2014; 32: 579.

104. Wu Y, Meng Q, Yang Z, et al. Circulating HER_2 mRNA in the peripheral blood as a potential diagnostic and prognostic biomarker in females with breast cancer. Oncol Lett. 2018;

105. Chiu RW, Lui W, Cheung M, et al. Time Profile of Appearance and Disappearance of Circulating Placenta-Derived mRNA in Maternal Plasma. Clin Chem. 2006; 52: 313–6.

106. Okazaki S. Measurement of mRNA of trophoblast-specific genes in cellular and plasma components of maternal blood. J Med Genet. 2006; 43: e47–e47.

107. Choi JJ, Pernot M, Small SA, Konofagou EE. Noninvasive, transcranial and localized opening of the blood-brain barrier using focused ultrasound in mice. Ultrasound Med Biol. 2007; 33: 95–104.

108. Bankhead P, Loughrey MB, Fernández JA, et al. QuPath: Open source software for digital pathology image analysis. Sci Rep. 2017; 7: 16878.

109. Shen J, Kong W, Wu Y, et al. Plasma mRNA as liquid biopsy predicts chemo-sensitivity in advanced gastric cancer patients. J Cancer. 2017; 8: 434–42.

110. Chang JW-C, Shih C-L, Wang C-L, et al. Transcriptomic Analysis in Liquid Biopsy Identifies Circulating PCTAIRE-1 mRNA as a Biomarker in NSCLC. Cancer Genomics - Proteomics. 2020; 17: 91–100.

111. Campos CDM, Jackson JM, Witek MA, Soper SA. Molecular Profiling of Liquid Biopsy Samples for Precision Medicine. Cancer J. 2018; 24: 93–103.

112. Wu Y, Meng Q, Yang Z, et al. Circulating HER_2 mRNA in the peripheral blood as a potential diagnostic and prognostic biomarker in females with breast cancer. Oncol Lett. 2018;

113. Samiotaki G, Konofagou EE. Dependence of the reversibility of focused- ultrasound-induced blood-brain barrier opening on pressure and pulse length in vivo. IEEE Trans Ultrason Ferroelectr Freq Control. 2013; 60: 2257–65.

114. Samiotaki G, Vlachos F, Tung YS, Konofagou EE. A quantitative pressure and microbubble-size dependence study of focused ultrasound-induced blood-brain barrier opening reversibility in vivo using MRI. Magn Reson Med. 2012; 67: 769–77.

115. Burgess A, Shah K, Hough O, Hynynen K. Focused ultrasound-mediated drug delivery through the blood–brain barrier. Expert Rev Neurother. 2015; 15: 477–91.

116. Martínez-González A, Calvo GF, Pérez Romasanta LA, Pérez-García VM. Hypoxic Cell Waves Around Necrotic Cores in Glioblastoma: A Biomathematical Model and Its Therapeutic Implications. Bull Math Biol. 2012; 74: 2875–96.

117. Forster J, Harriss-Phillips W, Douglass M, Bezak E. A review of the development of tumor vasculature and its effects on the tumor microenvironment. Hypoxia. 2017; Volume 5: 21–32.

118. Fontanilles M, Marguet F, Beaussire L, et al. Cell-free DNA and circulating TERT promoter mutation for disease monitoring in newly-diagnosed glioblastoma. Acta Neuropathol Commun. 2020; 8: 179.

119. Nabavizadeh SA, Ware JB, Guiry S, et al. Imaging and histopathologic correlates of plasma cell-free DNA concentration and circulating tumor DNA in adult patients with newly diagnosed glioblastoma. Neuro-Oncology Adv. 2020; 2: 1–9.

120. Magnin R, Rabusseau F, Salabartan F, et al. Magnetic resonance-guided motorized transcranial ultrasound system for blood-brain barrier permeabilization along arbitrary trajectories in rodents. J Ther Ultrasound. 2015; 3: 1–11.

121. McDannold N, Arvanitis CD, Vykhodtseva N, Livingstone MS. Temporary disruption of the blood-brain barrier by use of ultrasound and microbubbles: Safety and efficacy evaluation in rhesus macaques. Cancer Res. 2012; 72: 3652–63.

122. Aryal M, Vykhodtseva N, Zhang YZ, Park J, McDannold N. Multiple treatments with liposomal doxorubicin and ultrasound-induced disruption of blood-tumor and blood-brain barriers improve outcomes in a rat glioma model. J Control Release. 2013; 169: 103–11.

123. Liu HL, Tsai HC, Lu YJ, Wei KC. Neuronavigation-guided focused ultrasound-induced blood-brain barrier opening: A preliminary study in swine. AIP Conf Proc. 2012; 1503: 29–34.

124. O'Reilly MA, Jones RM, Barrett E, et al. Investigation of the safety of focused ultrasound-induced blood-brain barrier opening in a natural canine model of aging. Theranostics. 2017; 7: 3573–84.

125. Jones RM, Deng L, Leung K, et al. Three-dimensional transcranial microbubble imaging for guiding volumetric ultrasound-mediated blood-brain barrier opening. Theranostics. 2018; 8: 2909.

126. McDannold N, Zhang Y, Supko JG, et al. Acoustic feedback enables safe and reliable carboplatin delivery across the blood-brain barrier with a clinical focused ultrasound

system and improves survival in a rat glioma model. Theranostics. 2019; 9: 6284–99.

127. Lipsman N, Meng Y, Bethune AJ, et al. Blood–brain barrier opening in Alzheimer's disease using MR-guided focused ultrasound. Nat Commun. 2018; 9: 1–8.

128. Abrahao A, Meng Y, Llinas M, et al. First-in-human trial of blood–brain barrier opening in amyotrophic lateral sclerosis using MR-guided focused ultrasound. Nat Commun. 2019; 10: 1–9.

129. Gasca-Salas C, Fernández-Rodríguez B, Pineda-Pardo JA, et al. Blood-brain barrier opening with focused ultrasound in Parkinson's disease dementia. Nat Commun. 2021; 12: 1–7.

130. Rezai AR, Ranjan M, D'Haese P-F, et al. Noninvasive hippocampal blood-brain barrier opening in Alzheimer's disease with focused ultrasound. Proc Natl Acad Sci U S A. 2020; 1–3.

131. Johanns TM, Fu Y, Kobayashi DK, et al. High incidence of TERT mutation in brain tumor cell lines. Brain Tumor Pathol. 2016; 33: 222–7.

132. Inda M -d.-M, Bonavia R, Mukasa A, et al. Tumor heterogeneity is an active process maintained by a mutant EGFR-induced cytokine circuit in glioblastoma. Genes Dev. 2010; 24: 1731–45.

133. Sato H, Soh J, Aoe K, et al. Droplet digital PCR as a novel system for the detection of microRNA-34b/c methylation in circulating DNA in malignant pleural mesothelioma. Int J Oncol. 2019; 54: 2139–48.

134. Suzawa K, Yamamoto H, Ohashi K, et al. Optimal method for quantitative detection of plasma EGFR T790M mutation using droplet digital PCR system. Oncol Rep. 2017; 37: 3100–6.

135. Harper R, Reeves A. Reporting of precision of estimates for diagnostic accuracy: a review. BMJ. 1999; 318: 1322.1-1323.

136. Newcombe RG. Two-sided confidence intervals for the single proportion: comparison of seven methods. Stat Med. 1998; 17: 857–72.

137. Akshulakov SK, Kerimbayev TT, Biryuchkov MY, et al. Current Trends for Improving Safety of Stereotactic Brain Biopsies: Advanced Optical Methods for Vessel Avoidance and Tumor Detection. Front Oncol. 2019; 9: 947.

138. Trojanowski P, Jarosz B, Szczepanek D. The diagnostic quality of needle brain biopsy specimens obtained with different sampling methods – Experimental study. Sci Rep. 2019; 9: 8077.

139. Tseng C-L, Stewart J, Whitfield G, et al. Glioma consensus contouring recommendations from a MR-Linac International Consortium Research Group and evaluation of a CT-MRI and MRI-only workflow. J Neurooncol. 2020; 149: 305–14.

140. Chen L, Zhang Y, Yang J, Hagan JP, Li M. Vertebrate animal models of glioma: Understanding the mechanisms and developing new therapies. Biochim Biophys Acta - Rev Cancer. 2013; 1836: 158–65.

141. Robertson FL, Marqués-Torrejón M-A, Morrison GM, Pollard SM. Experimental models and tools to tackle glioblastoma. Dis Model Mech. 2019; 12: dmm040386.

142. Galanzha EI, Menyaev YA, Yadem AC, et al. In vivo liquid biopsy using Cytophone platform for photoacoustic detection of circulating tumor cells in patients with melanoma. Sci Transl Med. 2019; 11: eaat5857.

143. Keller L, Belloum Y, Wikman H, Pantel K. Clinical relevance of blood-based ctDNA analysis: mutation detection and beyond. Br J Cancer. 2021; 124: 345–58.

144. Rolfo C, Mack PC, Scagliotti G V., et al. Liquid Biopsy for Advanced Non-Small Cell Lung Cancer (NSCLC): A Statement Paper from the IASLC. J Thorac Oncol. 2018; 13: 1248–68.

145. Hall C, Lueshen E, Mošat' A, Linninger AA. Interspecies scaling in pharmacokinetics: A novel whole-body physiologically based modeling framework to discover drug biodistribution mechanisms in vivo. J Pharm Sci. 2012; 101: 1221–41.

146. Li H, Ruan J, Xie Z, Wang H, Liu W. Investigation of the critical geometric characteristics of living human skulls utilising medical image analysis techniques. Int J Veh Saf. 2007; 2: 345–67.

147. Sauleau P, Lapouble E, Val-Laillet D, Malbert C-H. The pig model in brain imaging and neurosurgery. Animal. 2009; 3: 1138–51.

148. Ohta M, Ohta K, Ma J, et al. Clinical and analytical evaluation of an enzyme immunoassay for myelin basic protein in cerebrospinal fluid. Clin Chem. 2000; 46: 1326–30.

149. Brommeland T, Rosengren L, Fridlund S, Hennig R, Isaksen V. Serum levels of glial fibrillary acidic protein correlate to tumour volume of high-grade gliomas. Acta Neurol Scand. 2007; 116: 380–4.

150. Sareen H, Garrett C, Lynch D, et al. The Role of Liquid Biopsies in Detecting Molecular Tumor Biomarkers in Brain Cancer Patients. Cancers (Basel). 2020; 12: 1831.

151. Jung CS, Foerch C, Schanzer A, et al. Serum GFAP is a diagnostic marker for glioblastoma multiforme. Brain. 2007; 130: 3336–41.

152. Sommerlath VN, Buergy D, Etminan N, et al. Molecular features of glioblastomas in long-term survivors compared to short-term survivors—a matched-pair analysis. Radiat Oncol. 2022; 17: 15.

153. Zavialova M, Shevchenko V, Nikolaev E, Zgoda V. Is myelin basic protein a potential biomarker of brain cancer? Eur J Mass Spectrom. 2017; 23: 192–6.

154. Gregory J V., Kadiyala P, Doherty R, et al. Systemic brain tumor delivery of synthetic protein nanoparticles for glioblastoma therapy. Nat Commun. 2020; 11: 5687.

155. Golfinos JG, Norman SA, Coons SW, et al. Expression of the genes encoding myelin basic protein and proteolipid protein in human malignant gliomas. Clin Cancer Res. 1997; 3: 799–804.

156. Arvanitis CD, Livingstone MS, Vykhodtseva N, McDannold N. Controlled Ultrasound-Induced Blood-Brain Barrier Disruption Using Passive Acoustic Emissions Monitoring. PLoS One. 2012; 7: e45783.

157. Chen H, Konofagou EE. The size of blood-brain barrier opening induced by focused ultrasound is dictated by the acoustic pressure. J Cereb Blood Flow Metab. 2014; 34: 1197–204.

158. Barnes SR, Ng TSC, Santa-Maria N, et al. ROCKETSHIP: a flexible and modular software tool for the planning, processing and analysis of dynamic MRI studies. BMC Med Imaging. 2015; 15: 19.

159. Tofts PS, Kermode AG. Measurement of the blood-brain barrier permeability and leakage space using dynamic MR imaging. 1. Fundamental concepts. Magn Reson Med. 1991; 17: 357–67.

160. Tofts PS. Modeling tracer kinetics in dynamic Gd-DTPA MR imaging. J Magn Reson Imaging. 1997; 7: 91–101.

161. Tofts PS, Brix G, Buckley DL, et al. Estimating kinetic parameters from dynamic contrast-enhanced t1-weighted MRI of a diffusable tracer: Standardized quantities and symbols. J Magn Reson Imaging. 1999; 10: 223–32.

162. Bradley WG. MR appearance of hemorrhage in the brain. Radiology. 1993; 189: 15–26.

163. FRY WJ. Intense ultrasound; a new tool for neurological research. J Ment Sci. 1954; 100: 85–96.

164. Lynn JG, Putnam TJ. Histology of Cerebral Lesions Produced by Focused Ultrasound. Am J Pathol. 1944; 20: 637–49.

165. Omuro AMP, Leite CC, Mokhtari K, Delattre J-Y. Pitfalls in the diagnosis of brain tumours. Vol. 5. 2006.

166. Gómez-Oliva R, Domínguez-García S, Carrascal L, et al. Evolution of Experimental Models in the Study of Glioblastoma: Toward Finding Efficient Treatments. Front Oncol. 2021; 10: 3245.

167. Khoshnevis M, Carozzo C, Bonnefont-Rebeix C, et al. Development of induced glioblastoma by implantation of a human xenograft in Yucatan minipig as a large animal model. J Neurosci Methods. 2017; 282: 61–8.

168. Selek L, Seigneuret E, Nugue G, et al. Imaging and histological characterization of a

human brain xenograft in pig: The first induced glioma model in a large animal. J Neurosci Methods. 2014; 221: 159–65.

169. O'Reilly MA, Waspe AC, Ganguly M, Hynynen K. Focused-Ultrasound Disruption of the Blood-Brain Barrier Using Closely-Timed Short Pulses: Influence of Sonication Parameters and Injection Rate. Ultrasound Med Biol. 2011; 37: 587–94.

170. Park SH, Kim MJ, Jung HH, et al. One-Year Outcome of Multiple Blood–Brain Barrier Disruptions With Temozolomide for the Treatment of Glioblastoma. Front Oncol. 2020; 10: 1663.

171. Wu S-K, Tsai C-L, Huang Y, Hynynen K. Focused Ultrasound and Microbubbles-Mediated Drug Delivery to Brain Tumor. Pharmaceutics. 2020; 13: 15.

172. Kelly P. Gliomas: Survival, origin and early detection. Surg Neurol Int. 2010; 1: 96.

173. Seo YJ, Cho WH, Kang DW, Cha SH. Extraneural Metastasis of Glioblastoma Multiforme Presenting as an Unusual Neck Mass. J Korean Neurosurg Soc. 2012; 51: 147.

174. Zhang H, Yuan F, Qi Y, Liu B, Chen Q. Circulating Tumor Cells for Glioma. Front Oncol. 2021; 11: 576.

175. Gao F, Cui Y, Jiang H, et al. Circulating tumor cell is a common property of brain glioma and promotes the monitoring system. Oncotarget. 2016; 7: 71330–40.

176. Juratli MA, Sarimollaoglu M, Siegel ER, et al. Real-time monitoring of circulating tumor cell release during tumor manipulation using in vivo photoacoustic and fluorescent flow cytometry. Head Neck. 2014; 36: 1207–15.

177. Campos-Carrillo A, Weitzel JN, Sahoo P, et al. Circulating tumor DNA as an early cancer detection tool. Pharmacol Ther. 2020; 207: 107458.

178. Liu MC, Oxnard GR, Klein EA, Swanton C, Seiden M. Response to W.C. Taylor, and C. Fiala and E.P. Diamandis. Ann Oncol. 2020; 31: 1268–70.

179. Cohen JD, Li L, Wang Y, et al. Detection and localization of surgically resectable cancers with a multi-analyte blood test. Science (80-). 2018; 359: 926–30.

180. Fahoum I, Forer R, Volodarsky D, et al. Characterization of Factors Affecting the Detection Limit of EGFR p.T790M in Circulating Tumor DNA. Technol Cancer Res Treat. 2018; 17: 153303381879365.

181. Marczynski GT, Laus AC, dos Reis MB, Reis RM, Vazquez V de L. Circulating tumor DNA (ctDNA) detection is associated with shorter progression-free survival in advanced melanoma patients. Sci Rep. 2020; 10: 18682.

182. Gorgannezhad L, Umer M, Islam MN, Nguyen N-T, Shiddiky MJA. Circulating tumor DNA and liquid biopsy: opportunities, challenges, and recent advances in detection technologies. Lab Chip. 2018; 18: 1174–96.

183. Fiala C, Kulasingam V, Diamandis EP. Circulating Tumor DNA for Early Cancer Detection. J Appl Lab Med. 2018; 3: 300–13.

184. Newman AM, Bratman S V, To J, et al. An ultrasensitive method for quantitating circulating tumor DNA with broad patient coverage. Nat Med. 2014; 20: 548–54.

185. Hori SS, Gambhir SS. Mathematical Model Identifies Blood Biomarker-Based Early Cancer Detection Strategies and Limitations. Sci Transl Med. 2011; 3: 109ra116-109ra116.

186. Sloan AE, Soler D, Young AB, Cooper KD, McCormic T. 219 Liquid Biopsy Can Distinguish Recurrent Glioblastomas From Pseudoprogression and Radiation Necrosis After Concurrent Radiochemotherapy. Neurosurgery. 2016; 63: 185–6.

187. Golde TE, Borchelt DR, Giasson BI, Lewis J. Thinking laterally about neurodegenerative proteinopathies. J Clin Invest. 2013; 123: 1847–55.

188. Wesseling H, Mair W, Kumar M, et al. Tau PTM Profiles Identify Patient Heterogeneity and Stages of Alzheimer's Disease. Cell. 2020; 183: 1699-1713.e13.

189. Dujardin S, Commins C, Lathuiliere A, et al. Author Correction: Tau molecular diversity contributes to clinical heterogeneity in Alzheimer's disease. Nat Med. 2021; 27: 356–356.

190. Morris M, Knudsen GM, Maeda S, et al. Tau post-translational modifications in wild-type and human amyloid precursor protein transgenic mice. Nat Neurosci. 2015; 18: 1183–9.

191. Schott JM, Reiniger L, Thom M, et al. Brain biopsy in dementia: clinical indications and diagnostic approach. Acta Neuropathol. 2010; 120: 327–41.

192. Thijssen EH, La Joie R, Wolf A, et al. Diagnostic value of plasma phosphorylated tau181 in Alzheimer's disease and frontotemporal lobar degeneration. Nat Med. 2020; 26: 387–97.

193. Janelidze S, Mattsson N, Palmqvist S, et al. Plasma P-tau181 in Alzheimer's disease: relationship to other biomarkers, differential diagnosis, neuropathology and longitudinal progression to Alzheimer's dementia. Nat Med. 2020; 26: 379–86.

194. Gafson AR, Barthélemy NR, Bomont P, et al. Neurofilaments: neurobiological foundations for biomarker applications. Brain. 2020; 143: 1975–98.

195. Khalil M, Teunissen CE, Otto M, et al. Neurofilaments as biomarkers in neurological disorders. Nat Rev Neurol. 2018; 14: 577–89.

196. Hampel H, O'Bryant SE, Molinuevo JL, et al. Blood-based biomarkers for Alzheimer disease: mapping the road to the clinic. Nat Rev Neurol. 2018; 14: 639–52.

197. Penner G, Lecocq S, Chopin A, et al. Blood-based diagnostics of Alzheimer's disease. Expert Rev Mol Diagn. 2019; 19: 613–21.

198. Yoshiyama Y, Higuchi M, Zhang B, et al. Synapse Loss and Microglial Activation

Precede Tangles in a P301S Tauopathy Mouse Model. Neuron. 2007; 53: 337–51.

199. López-González I, Aso E, Carmona M, et al. Neuroinflammatory Gene Regulation, Mitochondrial Function, Oxidative Stress, and Brain Lipid Modifications With Disease Progression in Tau P301S Transgenic Mice as a Model of Frontotemporal Lobar Degeneration-Tau. J Neuropathol Exp Neurol. 2015; 74: 975–99.

200. Sun Y, Guo Y, Feng X, et al. The behavioural and neuropathologic sexual dimorphism and absence of MIP-3α in tau P301S mouse model of Alzheimer's disease. J Neuroinflammation. 2020; 17: 72.

201. Jones RM, Deng L, Leung K, et al. Three-dimensional transcranial microbubble imaging for guiding volumetric ultrasound-mediated blood-brain barrier opening. Theranostics. 2018; 8: 2909–26.

202. McDannold N, Zhang Y, Supko JG, et al. Acoustic feedback enables safe and reliable carboplatin delivery across the blood-brain barrier with a clinical focused ultrasound system and improves survival in a rat glioma model. Theranostics. 2019; 9: 6284–99.

203. Wickham H. ggplot2 [Internet]. New York, NY: Springer New York; 2009. (Use R!).

204. Gratuze M, Leyns CEG, Sauerbeck AD, et al. Impact of TREM2R47H variant on tau pathology–induced gliosis and neurodegeneration. J Clin Invest. 2020; 130: 4954–68.

205. Woerman AL, Patel S, Kazmi SA, et al. Kinetics of Human Mutant Tau Prion Formation in the Brains of 2 Transgenic Mouse Lines. JAMA Neurol. 2017; 74: 1464.

206. Zhang DY, Gould A, Happ HC, et al. Ultrasound-mediated blood–brain barrier opening increases cell-free DNA in a time-dependent manner. Neuro-Oncology Adv. 2021; 3.

207. Tucker LB, Fu AH, McCabe JT. Hippocampal-Dependent Cognitive Dysfunction following Repeated Diffuse Rotational Brain Injury in Male and Female Mice. J Neurotrauma. 2021; 38: 1585–606.

208. Fesharaki-Zadeh A, Miyauchi JT, St. Laurent-Arriot K, Tsirka SE, Bergold PJ. Increased Behavioral Deficits and Inflammation in a Mouse Model of Co-Morbid Traumatic Brain Injury and Post-Traumatic Stress Disorder. ASN Neuro. 2020; 12: 175909142097956.

209. Leconte C, Benedetto C, Lentini F, et al. Histological and Behavioral Evaluation after Traumatic Brain Injury in Mice: A Ten Months Follow-Up Study. J Neurotrauma. 2020; 37: 1342–57.

210. Kato T, Inui Y, Nakamura A, Ito K. Brain fluorodeoxyglucose (FDG) PET in dementia. Ageing Res Rev. 2016; 30: 73–84.

211. Nazeri A, Chakravarty MM, Rotenberg DJ, et al. Functional Consequences of Neurite Orientation Dispersion and Density in Humans across the Adult Lifespan. J Neurosci. 2015; 35: 1753–62.

212. Vogt NM, Hunt JF, Adluru N, et al. Cortical Microstructural Alterations in Mild

Cognitive Impairment and Alzheimer's Disease Dementia. Cereb Cortex. 2020; 30: 2948–60.

213. Leuzy A, Chiotis K, Lemoine L, et al. Tau PET imaging in neurodegenerative tauopathies—still a challenge. Mol Psychiatry. 2019; 24: 1112–34.

214. Yamada K, Cirrito JR, Stewart FR, et al. In Vivo Microdialysis Reveals Age-Dependent Decrease of Brain Interstitial Fluid Tau Levels in P301S Human Tau Transgenic Mice. J Neurosci. 2011; 31: 13110–7.

215. Holth JK, Fritschi SK, Wang C, et al. The sleep-wake cycle regulates brain interstitial fluid tau in mice and CSF tau in humans. Science (80-). 2019; 363: 880–4.

216. Lashuel HA, Overk CR, Oueslati A, Masliah E. The many faces of α-synuclein: from structure and toxicity to therapeutic target. Nat Rev Neurosci. 2013; 14: 38–48.